

AD-A139 565

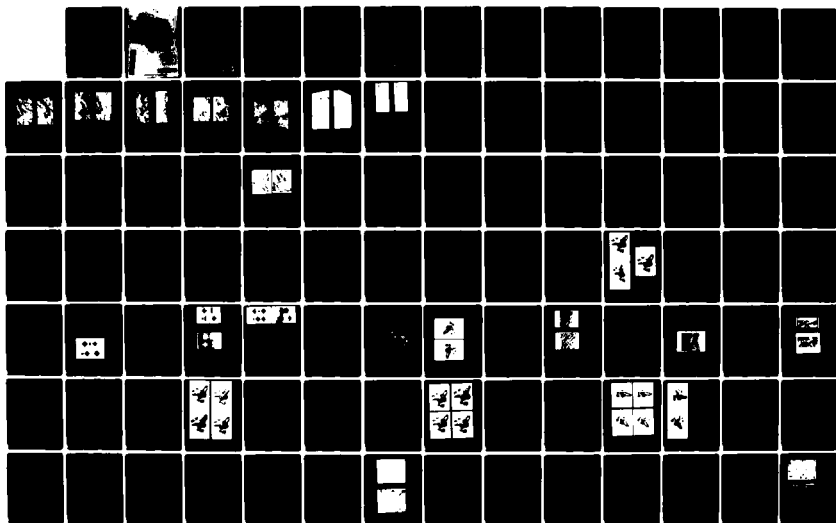
EVALUATION OF RADARGRAMMETRIC STEREO(U) INSTITUT FÜR  
DIGITALE BILDVERARBEITUNG UND GRAPHIK GRAZ (AUSTRIA)  
G DOMIK ET AL. 11 OCT 83 F49620-82-C-0053

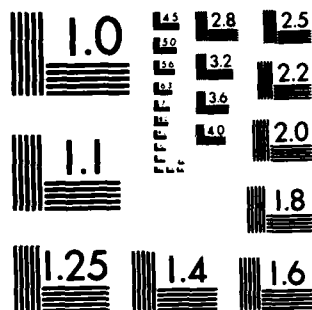
1/2

UNCLASSIFIED

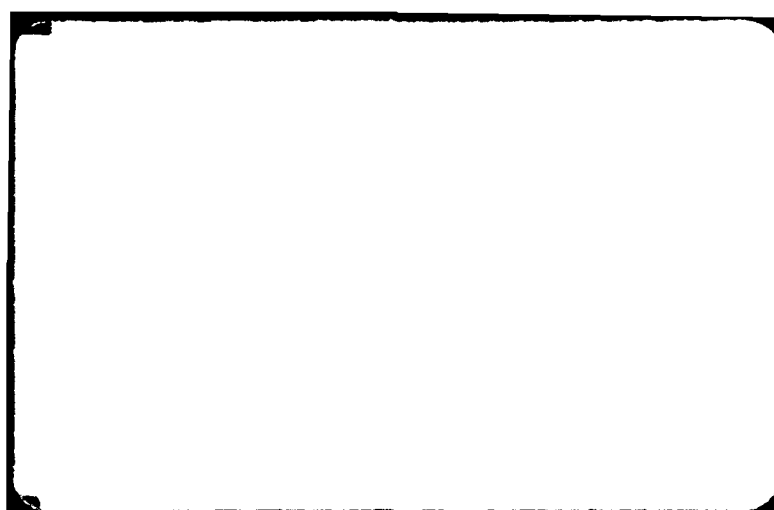
F/G 17/9

NL





MICROCOPY RESOLUTION TEST CHART  
NATIONAL BUREAU OF STANDARDS-1963-A



Contract Number F49620-82-C-0053.

EVALUATION OF RADARGRAMMETRIC STEREO

Gitta Domik, Franz Leberl, Johannes Raggam

Technical University  
and Graz Research Center  
A-8010 Graz, Austria

11 October 1983

Final Scientific Report  
1 July 1982 - 30 June 1983

Approved for public release distribution unlimited.

Prepared for  
USAF, AFSC  
Air Force Office of Scientific Research  
and  
European Office of Aerospace  
Research and Development  
London, England

DTIC  
ELECTE  
MAR 27 1984  
A

REPORT DOCUMENTATION PAGE		READ INSTRUCTIONS BEFORE COMPLETING FORM
1. REPORT NUMBER	2. GOVT ACCESSION NO. <b>AD-A139 565</b>	3. RECIPIENT'S CATALOG NUMBER
4. TITLE (and Subtitle)  <b>EVALUATION OF RADARGRAMMETRIC STEREO</b>		5. TYPE OF REPORT & PERIOD COVERED <b>FINAL REPORT, 1 July 82 - 30 June 83</b>
		6. PERFORMING ORG. REPORT NUMBER
7. AUTHOR(s)  <b>G. DOMIK, F. LEBERL, J. RAGGAM</b>		8. CONTRACT OR GRANT NUMBER(s)  <b>F49620-82-C-0053</b>
9. PERFORMING ORGANIZATION NAME AND ADDRESS		10. PROGRAM ELEMENT, PROJECT, TASK AREA & WORK UNIT NUMBERS
11. CONTROLLING OFFICE NAME AND ADDRESS <b>USAF, AFSC Air Force Office of Scientific Research Building 410, Bolling AFB, DC 20332</b>		12. REPORT DATE <b>11 October 1983</b>
		13. NUMBER OF PAGES <b>127</b>
14. MONITORING AGENCY NAME & ADDRESS (if different from Controlling Office)		15. SECURITY CLASS. (of this report)
		15a. DECLASSIFICATION/DOWNGRADING SCHEDULE
16. DISTRIBUTION STATEMENT (of this Report)		
<div style="border: 1px solid black; padding: 5px; display: inline-block;"> <b>DISTRIBUTION STATEMENT A</b>  <b>Approved for public release</b>  <b>Distribution Unlimited</b> </div>		
17. DISTRIBUTION STATEMENT (of the abstract entered in Block 20, if different from Report)		
18. SUPPLEMENTARY NOTES		
19. KEY WORDS (Continue on reverse side if necessary and identify by block number)  <b>Radar imagery, stereoscopy, image simulation, radargrammetry, radar height measurements.</b>		
20. ABSTRACT (Continue on reverse side if necessary and identify by block number)  <b>The ability of an observer to stereoscopically view overlapping radar image pairs is evaluated. This analysis is based on a set of aircraft and satellite radar data, and on data generated by means of computer simulation. Synthesis of radar images is based on digital elevation models, allowing one to study a much wider range of flight parameters and sensor geometries than is currently available for study with real data. The report discusses</b>		

simulation techniques, presents an evaluation of different radar-grammetric stereo geometries and analyses effects of squint angle, look angles and look angle differences on the stereoscopic viewability of overlapping radar image.

X

# Abstract

The ability of an observer to stereoscopically view overlapping radar image pairs is evaluated. This analysis is based on a set of aircraft and satellite radar data, and on data generated by means of computer simulation. Synthesis of radar images is based on digital elevation models, allowing one to study a much wider range of flight parameters and sensor geometries than is currently available for study with real data. The report discusses simulation techniques, presents an evaluation of different radargrammetric stereo geometries and analyses effects of squint angle, look angles and look angle differences on the stereoscopic viewability of overlapping radar images.

Accession For	
NTIS GRA&I	<input checked="" type="checkbox"/>
DTIC TAB	<input type="checkbox"/>
Unannounced	<input type="checkbox"/>
Justification <i>NR TR</i>	
By _____	
Distribution/ _____	
Availability Codes	
Dist	Avail and/or Special
<i>A-1</i>	



# TABLE OF CONTENTS

1.	Introduction.....	4
2.	Radar Stereoscapy.....	6
2.1	Background.....	6
2.2	Stereo Viewing Considerations.....	8
	(a) Acuity.....	8
	(b) Viewability .....	8
2.3	Radar Stereoscopic Computations.....	16
2.4	Stereoscopic Exaggeration.....	19
	(a) Definition of an Exaggeration Factor.....	19
	(b) Radar Stereoscopic Exaggeration.....	21
2.5	Radar Stereoscapy with Non-Paralllel Flight Lines....	24
	(a) Ground Range Presentation.....	32
	(b) Slant Range Presentation.....	33
3.	Image Simulation Approaches.....	34
3.1	Object Space Algorithm.....	34
	(a) General Description.....	34
	(b) Example.....	35
	(c) Arbitrary Flight Path and Squint Angle.....	35
3.2	Image Space Algorithm.....	39
	(a) General Description.....	39
	(b) Deriving Sensor Position <u>s</u> and range r from Image Coordinates.....	39
	(c) Local vs. Sensor Coordinates.....	40
	(d) Range Sphere and Doppler Cone.....	42
	(e) Intersecting Projection Circle with DEM.....	44
	(f) Arbitrary Flight Path.....	44
	(g) Geometric Rectification of Squint Angle Images.....	44
3.3	Radiometric Model.....	48
	(a) Shadow.....	48
	(b) Assigning Grey Values.....	49
3.4	Discussion and Implementation.....	50
4.	Verification of Simulation Program .....	51
4.1	Using Geometric Shapes.....	51
4.2	SIR-A Data.....	56
	(a) Greek Islands.....	56
	(b) North-California.....	59
4.3	SAR-580.....	61



5.	Discussion of Stereo Viewability .....	65
5.1	Same Side Flight Tracks -- Different Elevation Angles.....	66
5.2	Distortions of Same Side Stereo with Applied Squint Angle.....	71
5.3	Crossing Flight Tracks -- Same Elevation Angles.....	74
6.	On the Accuracy of Radar Stereo Mapping.....	77
6.1	Theoretical Error Analysis of Radar Stereo Models....	77
	(a) Errors in Sensor Position Coordinates.....	78
	(b) Errors in Sensor Attitude Vectors.....	81
	(c) Errors in Slant Ranges.....	83
6.2	Accuracies with Parallax Measurements.....	84
6.3	Rigorous Radar Stereo Mapping.....	88
6.3.1	Mathematical Formulation.....	88
6.3.2	Results Obtained with Rigorous Stereo Radargrammetry.....	91
7.	Conclusions and Future Plans.....	94
Appendix A - Description of Simulation Package		
Appendix B - Figures and Tables		
Literature		

## 1. Introduction

Efforts to map an object or a planetary surface usually include the reconstruction of the three-dimensional shape of the object. There exist various approaches to this task: use of overlapping images to detect and measure geometry differences as a function of the sensor position (stereo-correlation); use of brightness changes in one image (photo-clinometry, "shape-from-shading"); and ranging from a known position to the unknown object surface (profiling, altimetry).

One can denote these reconstructions by "stereo-mapping", since the greek word "stereo" means "spatial", "solid". For complex topographical surfaces only overlapping images have been used. Other approaches serve with other objects: robot-vision may employ "shape-from-shading"; smooth ocean surfaces may be mapped by altimetry.

Detail in multiple images for stereo-mapping must be correlated from one image to the other. This is done by visual matching using human stereoscopic vision, or a machine is used to perform the image correlation task.

With conventional camera photography the stereoscopic viewing process is well understood (La Prade, 1980). The camera is an analogon to normal vision.

However, there are cases where mapping is done with other imaging devices such as radar (Fig. 1.1), e.g. in adverse climates (tropics, arctic) or in remote regions (planet Venus). It is well known that stereoscopic viewing can be used with radar images as well. One also has an understanding of geometric error propagation into measured 3-d coordinates. Only the limitations of radar stereoscopy are not researched to any extent. Such research is vital not only for mapping topographical heights, but also is needed in the visual interpretation of images for thematic mapping.

Therefore, it is the purpose of this report to review existing and to present new understanding of radar stereoscopy. For this purpose, a set of radar image data has been compiled and evaluated with respect to stereoscopic viewing. The range of data, however, was found to be too restricted to allow one to draw firm conclusions. Therefore a system for simulation of radar images was developed and synthesized data were employed in the stereo viewing evaluation.

The problem of radar stereoscopy is introduced in this report by discussion of stereo viewing that follows the extensive body of work on the subject (e.g. La Prade, 1970; Leberl, 1979). We then describe the computer simulation technique used to obtain radar images for evaluation. Both simulated and real images from satellites and aircrafts serve in the analysis of stereo-viewability of this data.

Based on the conclusions of the evaluation one now can predict the achievable height-mapping accuracy. Established theoretical error propagation models must be examined with respect to stereo-measurability or viewability.

The conclusion is reached that numerous flight arrangements can be used to obtain stereoscopic radar images, that stereoscopic viewing often is only feasible with considerable strain on the observer, and that height accuracies can be obtained for mapping at small scale, and for differential rectification.

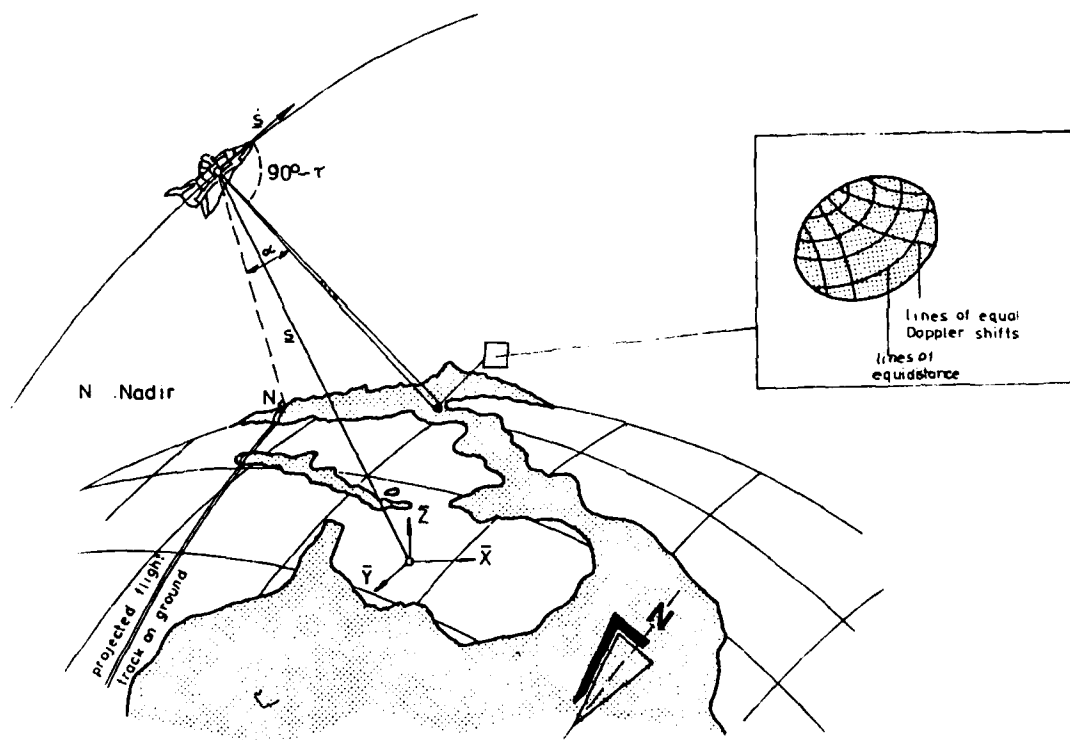


Figure 1.1 : Radar imaging from orbit, where  $\underline{s}$  is the position vector of the sensor.

## 2. RADAR STEREOSCOPY

### 2.1 Background

Stereo viewing of overlapping images is a valuable tool in photointerpretation. It is also indispensable for the identification and measurement of homologous points in two overlapping images and subsequent reconstruction of the three-dimensional topographic relief. This may serve to create a model of terrain topography, e.g. in the form of contours, or to selectively measure slopes and relative height differences.

This terminology is based on the authoritative review of LaPrade et al. (1980). It differs from that used for example in the German photogrammetric literature (Rinner and Burkhardt 1972) where both the direct perception of space and the viewing of overlapping images are denoted by stereo viewing. Techniques of generating three-dimensional object space coordinates from sets of monocular image measurements is the topic of stereology.

For the observer radar stereo viewing is hardly different from viewing conventional photographs, although there exists an entirely different projection geometry and mathematical model. The human observer perceives displacements of image points due to height differences (relief displacement). These form so-called parallax differences irrespective of whether we deal with natural binocular vision or with two images in stereoscopic viewing.

Already a considerable body of literature has accumulated on stereo radar, beginning with LaPrade (1963). Previous work was reviewed and some numerical results were presented by Leberl (1979). Stereo viewability of radar images was discussed by LaPrade (1970), Graham (1975), Leberl (1975, 1978, 1979) and by Kaupp et al. (1982). Computation of three-dimensional object coordinates from overlapping images was analysed by Innes (1964), Rosenfield (1968), Gracie et al. (1970), Konecny (1972), DBA-Systems (1974), Goodyear (1974), Derenyi (1975) and Leberl (1972, 1975, 1978).

The most commonly discussed radar stereo imaging arrangements are shown in Figure 2.1.

They have either both flights to the same side or each of the two flights at opposite sides of the object. Other arrangements have been described but have not materialized: these include cross-wise flights (Graham, 1975) and different flight altitudes or single flight convergent schemes such as with tilted antennas in a real aperture

radar (Leberl, 1972; Carlson, 1973; Bair and Carlson, 1974, 1975). It is not possible to generate stereo SAR from a single straight flight line Fig. (2.1b), a topic discussed in detail in a preceding study (Leberl, 1979).

The current considerations are separate from previous theoretical error analyses. We discuss the concept of exaggeration factors for evaluation of image pairs.

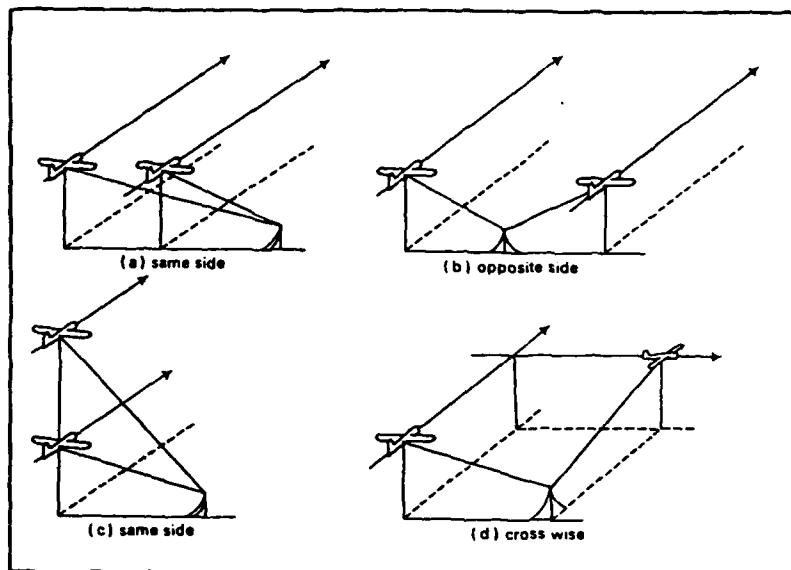


Figure 2.1a: Flight configurations to obtain overlapping images with two flight lines.

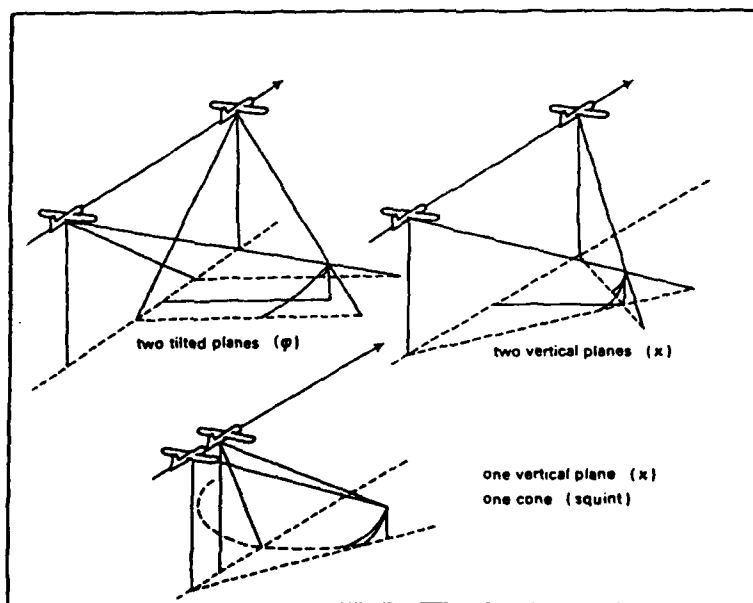


Figure 2.1b: Flight configurations to obtain overlapping images with one flight line and real aperture antenna.

## 2.2 Stereo Viewing Considerations

### (a) Acuity

Measurements in overlapping images should always be made stereoscopically. The minimum observable retinal disparity for binocular vision is reported by LaPrade et al (1980) at 3". Muenster (1942) reports a mean value of 6" under good lighting conditions. The optimum can be achieved with lines in object space that run parallel. On the other hand, there exists also a maximum viewable stereo disparity angle: this amounts to 70" (Rinner and Burkhardt 1972). Monocularly two objects can be distinguished if they create an angular disparity in one eye of perhaps 20". Thus stereoscopy has a distinct advantage: if one were to monocularly measure the same point in two images, a measuring error will be committed that is several times larger than in a stereoscopic mode.

### (b) Viewability

The two partners of a stereo image pair must be very similar in image quality or thematic content (tone, texture, etc.) so that they correlate well, whereas they should be sufficiently different in geometry to present parallaxes for height perception. Since radar is actively illuminating the target, differences in geometry due to different sensor positions imply also illumination differences.

From a geometric point of view good radar stereoscopy therefore seems to conflict with good viewability. In aerial photo interpretation the required parallaxes are obtained without any illumination differences in the two stereopartners: the sun illumination hardly changes from one photograph to the next. Stereo viewability is not a problem with photography. It is the essential problem with radar. Figures 2.2 through 2.8 present some examples of stereo radar models from:

- (i) aircraft with opposite-side illumination (Figure 2.2);
- (ii) aircraft, with same-side illumination (Figures 2.3, 2.4);
- (iii) same-side illumination from an aircraft and satellite SAR (Figures 2.4, 2.5);
- (iv) satellite (SEASAT) with same-side and opposite-side illumination (Figures 2.6, 2.7);
- (v) lunar Apollo 17 radar with same-side illumination (Figure 2.8).

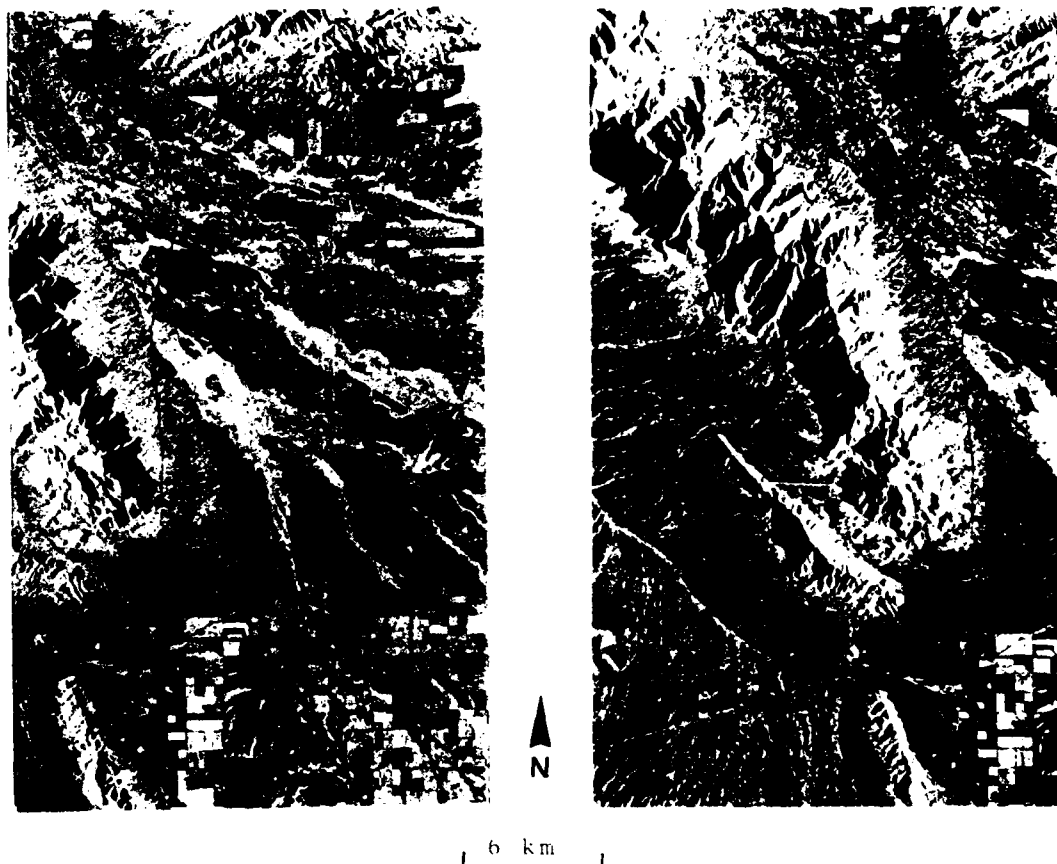


Figure 2.2: Aircraft radar pair, opposite side stereo, of Goodyear Electronic Mapping System (GEMS), over Estrella Mtn.; wavelength 3 cm, synthetic aperture.

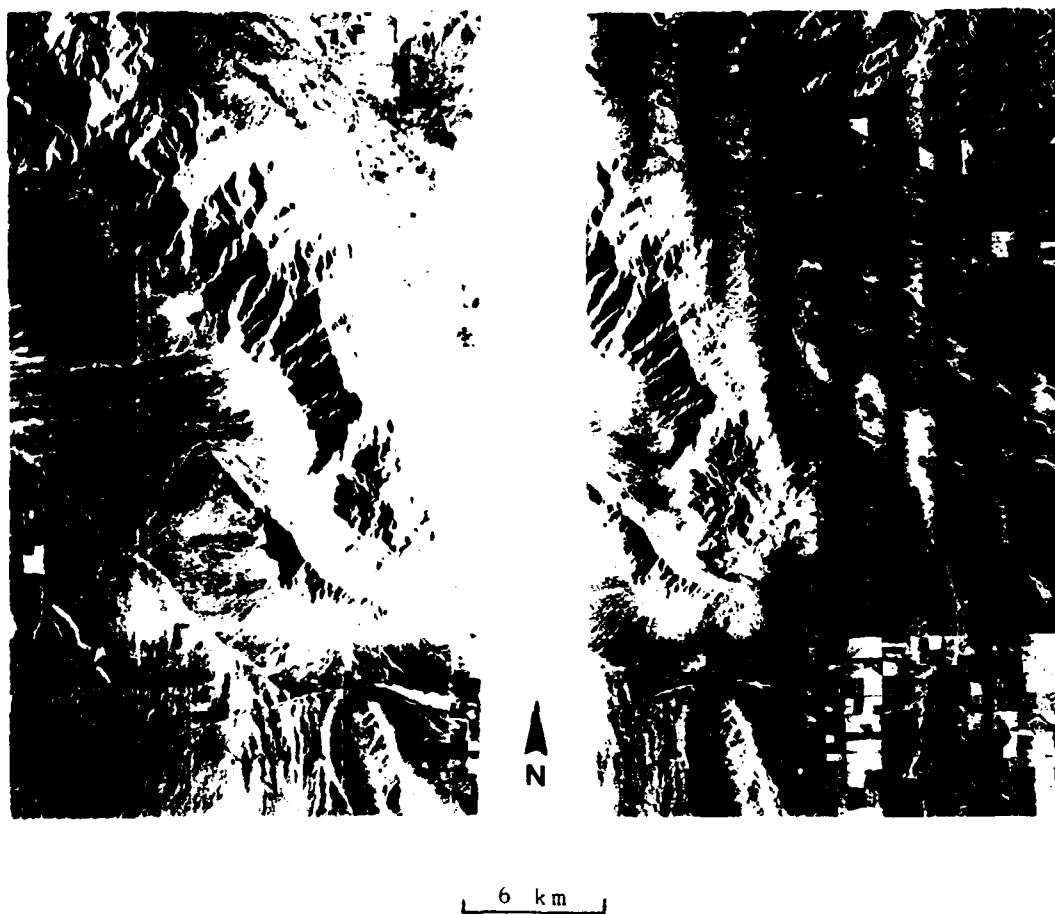


Figure 2.3: Aircraft radar pair as in Figure 2.2, same-side geometry.



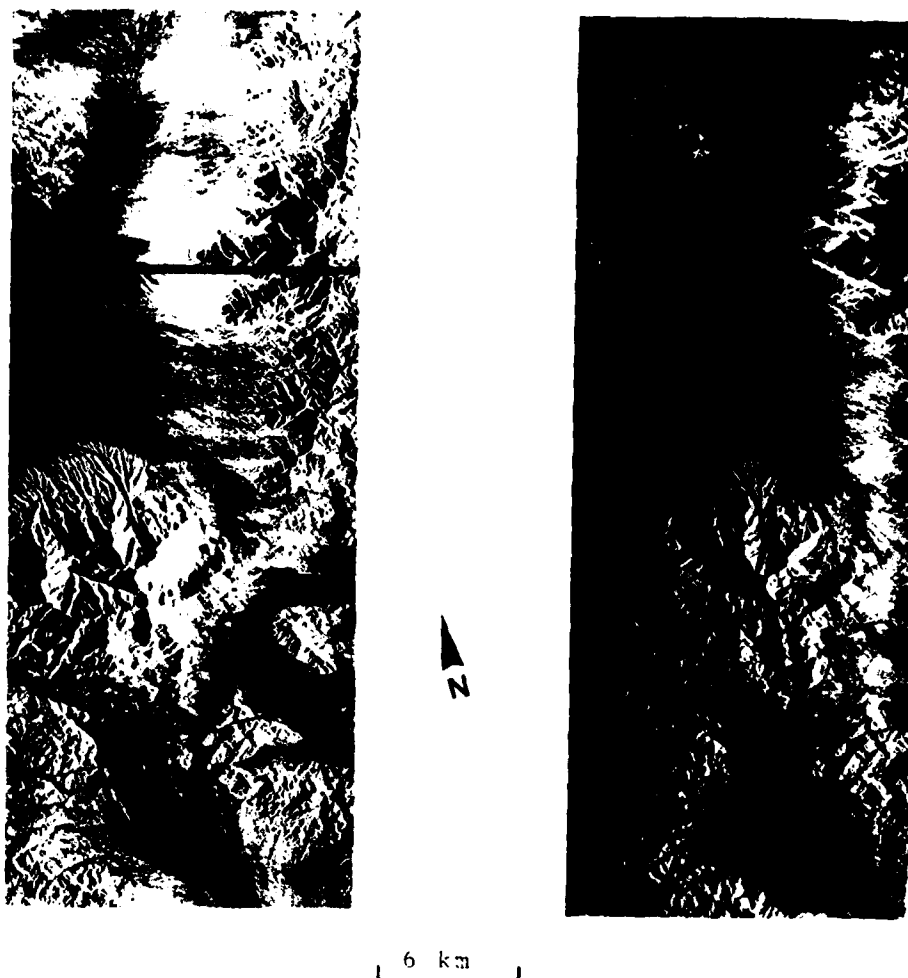


Figure 2.4: Same-side geometry radar stereo, Goodyear Electronic Mapping System (GEMS), over Granite Mtn. Arizona, flight-height 10 km, wavelength 3 cm, synthetic aperture.

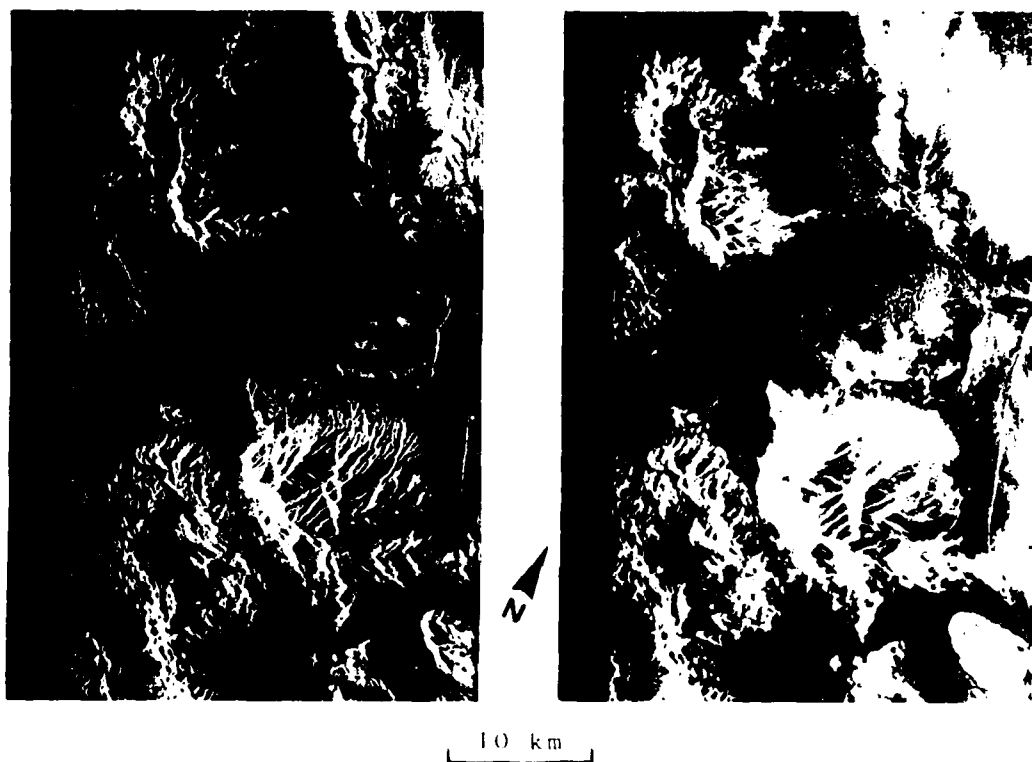


Figure 2.5: Same-side geometry radar stereo, SEASAT-SAR, wavelength 25 cm, flight altitude 810 km, look angles about  $20^\circ$ .

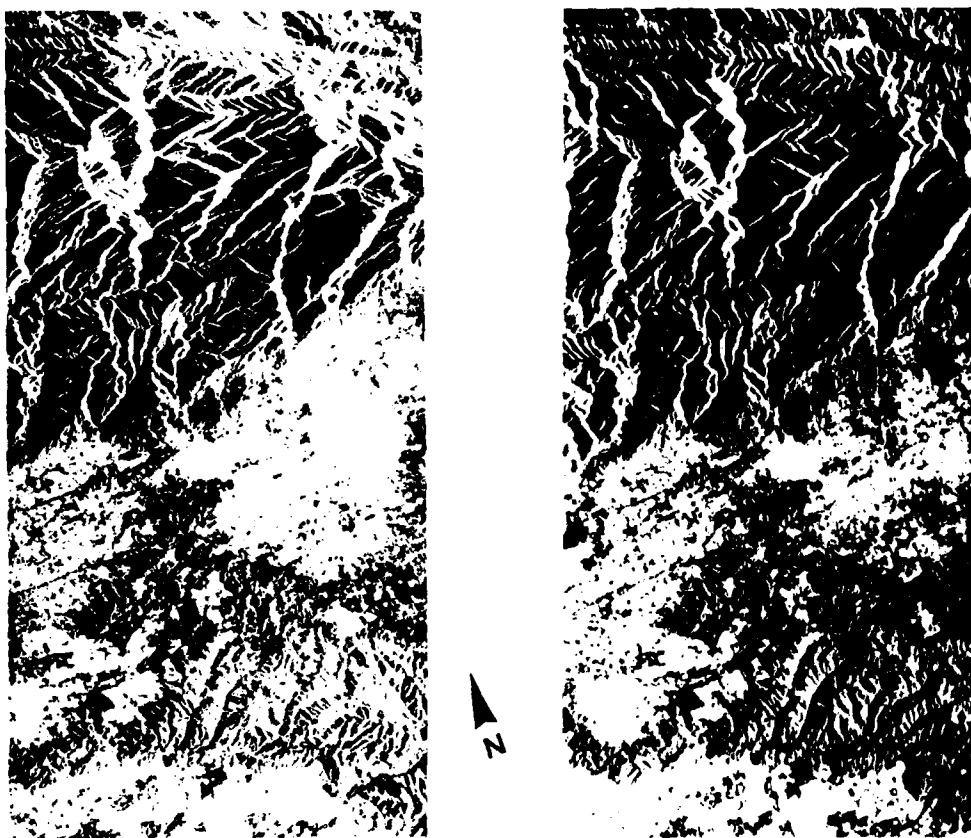


Figure 2.6: SEASAT-SAR stereo radar image pair, flight altitude 810 km, look angles about  $20^{\circ}$ . Same-side geometry, Los Angeles area.

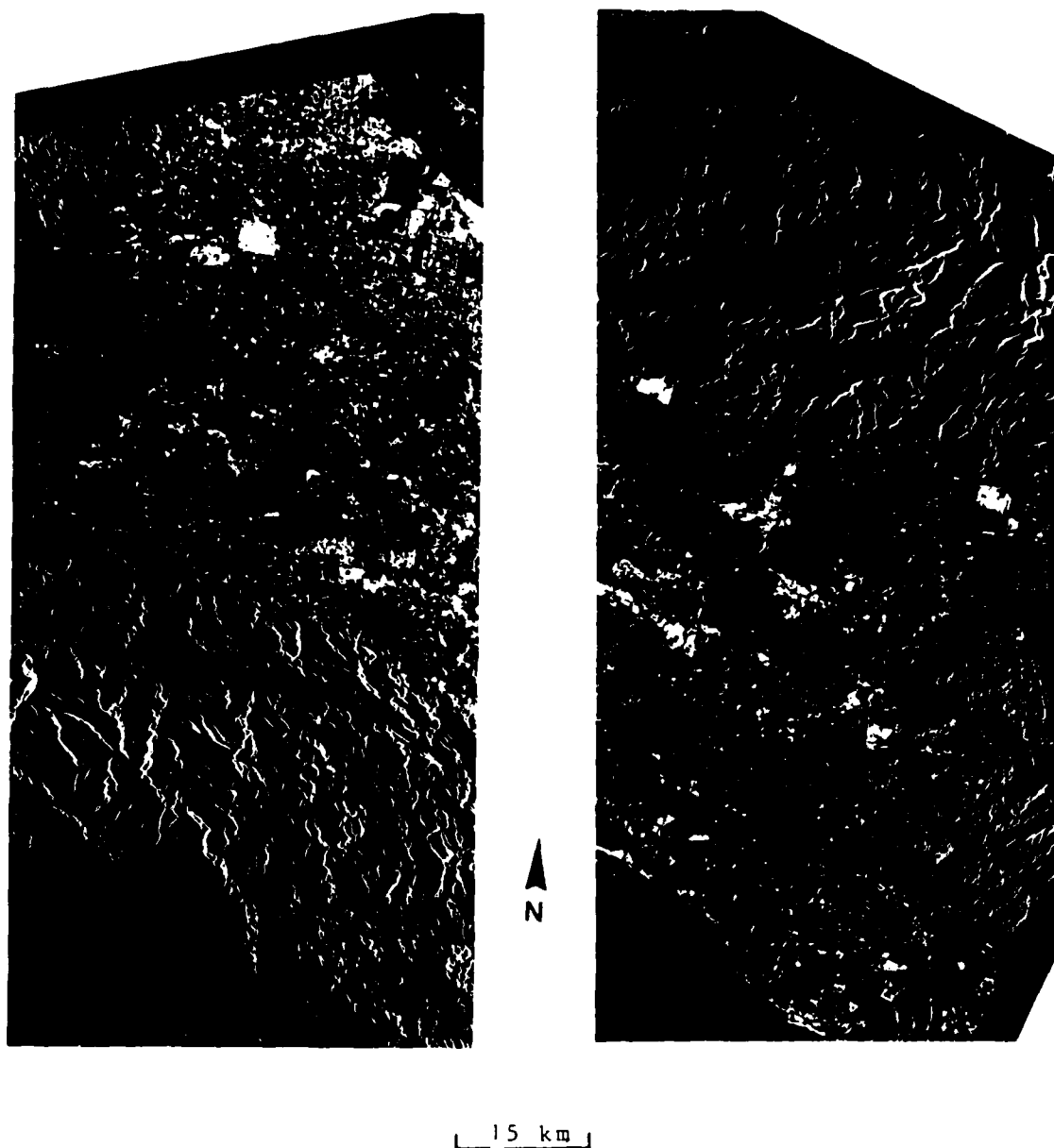
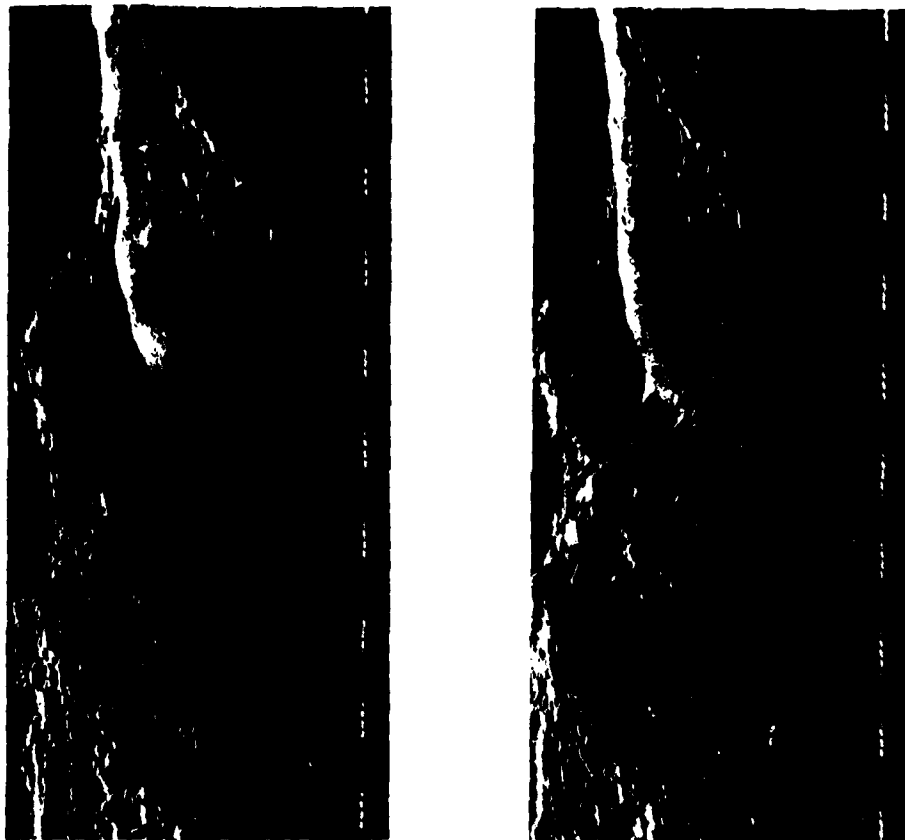


Figure 2.7: SEASAT-SAR stereo radar image pair of Los Angeles, opposite-side geometry, combining a descending orbit with an ascending one.



20 km

Figure 2.8: Apollo 17 Lunar Sounder Experiment (ALSE) image pair over Montes Appenninus on the Moon, flight altitude is 112 km, stereo base 3.5 km, same side geometry, wavelength is 2 m.

A subjective evaluation of stereo viewability by an observer reveals that influencing factors on stereo are:

- stereo-arrangement;
- look angles off-nadir;
- stereo intersection angles;
- ruggedness of the imaged area.

Viewability is thus ensured at shallow look angles for same-side arrangements. Opposite-side stereo may be feasible with flat or gently rolling terrain. The limits of the actual performance cannot be defined precisely using imagery available today. One has to investigate this with the help of an even larger set of images, in particular with a larger variety of cases; image simulation offers a means to evaluate the subjective capability of an observer viewing radar stereo data.

LaPrade (1975) reports on one experiment with operators studying same-side stereo of flat areas with man-made objects. Optimum results were reported to require look angles of 37 to 67 degrees off-nadir and intersection angles of about 12 to 15 degrees. These intersection angles may seem poor, but it will be shown later that radar has the potential to still produce vertical exaggeration approaching that of standard photo-interpretation.

### 2.3 Radar Stereoscopic Computations

General formulations for radar stereo computations have been proposed by Gracie et al. (1970) and others. The literature was reviewed by Leberl (1979). Simplified formulations for parallel flight lines are more commonly employed. For these recti-linear flights at constant altitude are assumed with the flight direction parallel to the object x-coordinate axis (Figure 2.9).

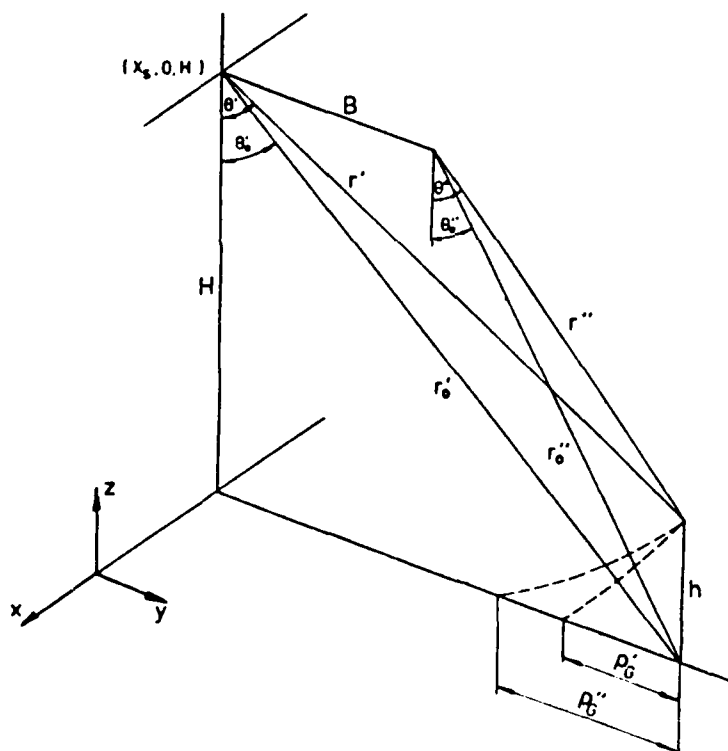


Figure 2.9: Definition of entities for radar stereo computations.

We read from the figure that the object  $x_p, y_p, z_p$  - coordinates of a point P are:

$$\begin{aligned} x_p &= x_s & (2.1) \\ y_p &= (r'^2 - r''^2 + B^2)/(2B) \\ z_p &= H - ((r'^2 - y_p^2)^{1/2} + (r''^2 - (B - y_p)^2)^{1/2})/2 \end{aligned}$$

where B is the stereo base, H is the flying height.

A slightly different approach to compute the height h above a reference datum is still with projection circles:

$$\begin{aligned} y &= \tan \theta' (H-h) \\ y &= \pm \tan \theta'' \cdot (H-h) + B & (2.2) \\ h &= H - B / (\tan \theta' \pm \tan \theta'') \end{aligned}$$

To relate the object height h above a reference datum to parallax difference dp measured on an image pair for given look and intersection angles, we have from Figure 9 for ground range images:

$$\begin{aligned} pg' &= H \cot \theta_o' - H \cot \theta' \\ pg'' &= H \cot \theta_o'' - H \cot \theta'' \end{aligned}$$

and

$$\begin{aligned} \cot \theta_o' &= \cot \theta' (H-h)/H \\ \cot \theta_o'' &= \cot \theta'' (H-h)/H \end{aligned}$$

combining:

$$\begin{aligned} dpg &= pg'' - pg' \\ dpg/h &= \cot \theta' - \cot \theta'' & (2.3) \end{aligned}$$

Note that a given parallax dpg generates a different height h depending on  $\theta_o'$  and  $\theta_o''$ . This means that apparent heights will change across a stereo model, in contrast to photographic stereo where a given parallax always corresponds to the same height independent of where in the

stereo model it has been measured.

For slant range images parallax can be defined as follows:

$$\begin{aligned} \text{dps} &= r'' - r' \\ &= (H-h) (\sec \theta'' - \sec \theta') \end{aligned} \quad (2.4)$$

Here, unlike ground range pairs, we find that zero heights still generate non-zero parallaxes. This means that the datum surface in a slant range pair will appear curved, which we may calculate by setting  $h=0$ ,  $\theta' = \theta_0'$  and  $\theta'' = \theta_0''$ :

$$\text{dpdatum} = H(\sec \theta_0'' - \sec \theta_0')$$

Topographic relief will appear to lie on top of this curved surface, according to

$$\begin{aligned} \text{dps} - \text{dpdatum} &= (H-h) (\sec \theta'' - \sec \theta') \\ &\quad - H(\sec \theta_0'' - \sec \theta_0') \end{aligned} \quad (2.5)$$

We also know from the geometry that

$$\begin{aligned} \tan \theta' &= y/(H-h), & \tan \theta'' &= (y-B)/(H-h), \\ \tan \theta_0' &= y/H, & \tan \theta_0'' &= (y-B)/H. \end{aligned}$$

These combine to yield

$$\begin{aligned} \sec \theta' &= (1 + \tan^2 \theta' \cdot H^2 / (H-h)^2)^{1/2} \\ \sec \theta'' &= (1 + \tan^2 \theta'' \cdot H^2 / (H-h)^2)^{1/2} \end{aligned}$$

Substituting in equ. (2.5):

$$\begin{aligned} (\text{dps} - \text{dpdatum})/h &= \\ &= ((H-h)^2 + H^2 \tan^2 \theta'')^{1/2} - ((H-h)^2 + H^2 \tan^2 \theta_0')^{1/2} - \\ &\quad - H(\sec \theta_0'' - \sec \theta_0')/h \end{aligned} \quad (2.6)$$



For  $H \gg h$  this simplifies to

$$\begin{aligned} (dps - dpdatum)/h &= ((\sec^2 \theta_0'' - 2h/H)^{1/2} - \\ &(\sec^2 \theta_0' - 2h/H)^{1/2} - \\ &\sec \theta_0'' + \sec \theta_0') H/h \end{aligned} \quad (2.7)$$

Equations (2.3) and (2.7) allow one to compute parallax differences for each stereo configuration and object height difference, and will be used for the evaluation of exaggeration factors in the following section.

## 2.4 Stereoscopic Exaggeration

### (a) Definition of an Exaggeration Factor

Stereo imaging geometry is usually being judged by two numbers: The first,  $1/t$ , indicates a ratio between a parallactic distance obtained by natural binocular vision and the parallactic distance observed in the stereoscopic image pair;  $t$  is called the "total plastic". It is assumed that natural vision and stereo image generation are from the same distance to the object. Typically,  $t$  can be as large as several hundred thousand. Since the figure compares natural binocular vision with stereoscopic images it is not of interest in the current context.

The second number is of greater significance: it describes the "flatness" of the observed stereoscopic impression in the form of an "exaggeration factor",  $q$ . Since we observe stereo imagery with a central perspective geometry, we need first to understand this factor for that arrangement, then extend the concept to apply to radar image geometry as well. Stereoscopic exaggeration, or affine stretch, of the observed object is a common concept that is discussed in photogrammetric manuals (LaPrade et al. 1980; Rinner and Burkhardt, 1972). For ease of reference we present this concept.

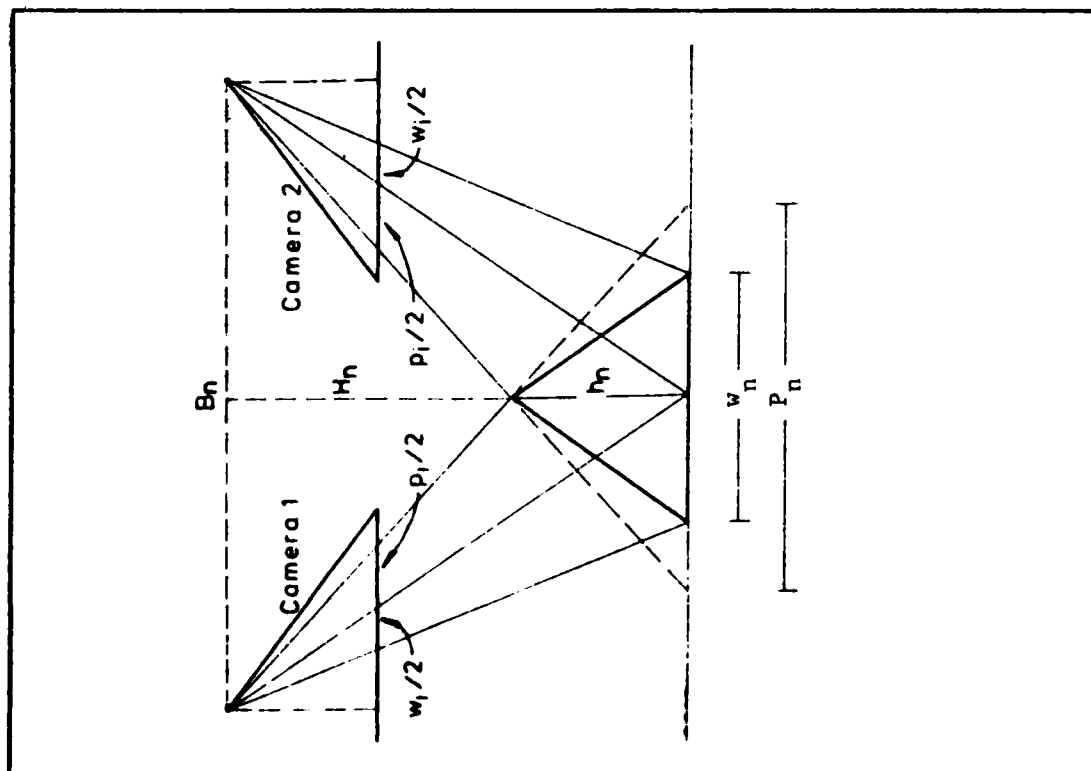


**Figure 2.10a:** Definitions for the vertical exaggeration factor after La Parade et al. (1930).  
Object space.

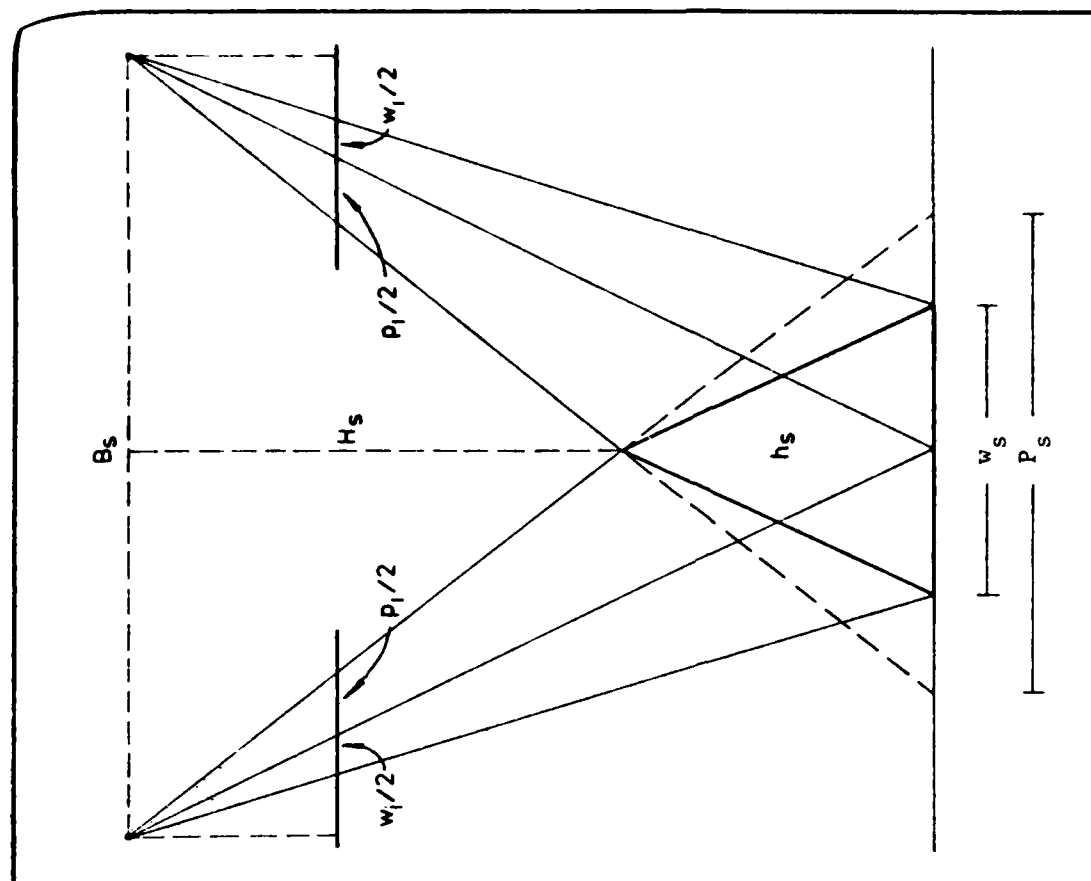


**Figure 2.10b: Definitions for the vertical exaggeration factor after La Parade et al. (1980). Stereoscopic reconstruction.**

Figure 2.10 shows the central perspective image collection geometry for a pair of cameras and an observer looking at a stereoscopic image pair through the lenses of a stereoscope. The object is a pyramid of the height,  $h_n$ , and base  $w_n$ . For the exaggeration factor one defines the ratio  $h_n/w_n$  of the pyramid in object space. This appears from the stereo observation as  $h_s/w_s$ . This allows one to define  $q$ , the exaggeration factor, as a measure of the flatness of the observed stereo model:

$$q = (h_s/w_s) / (h_n/w_n) \quad (2.8)$$

It can be shown that the exaggeration factor is independent of the dimensions of the object and merely depends on the so-called "base-to-height-ratios",  $H_n/B_n$ , in object space, and  $H_s/B_s$  for stereoviewing:

$$q = (H_s/B_s) / (B_n/H_n) \quad (2.9)$$

The transformation of equ. (2.8) into equ. (2.9) is discussed by LaPrade et al. (1980).

In natural binocular vision the eyes form a convergence angle, of about 14 degrees or less. This converts to a value for  $H_s/B_s$  of about 4. One can verify by experiment that optimum stereoscopic viewing is achieved with:

$$H_s/B_s \approx 5$$

$$\text{so that: } q \approx 5 (B_n/H_n) \quad (2.10)$$

This stereo exaggeration factor will now be applied to radar images.

#### (b) Radar Stereoscopic Exaggeration

The exaggeration factor,  $q$ , as defined for camera photography relates a subjectively observed pyramid in the stereoscopic model to the same pyramid in object space. Since we can relate the radar stereoparallax  $dp$  to the equivalent photographic stereo case it is possible to compare the quality of radar and camera stereoscopy. We merely need to find the photographic base-to-height ratio,  $B_n/H_n$ , of a fictitious camera arrangement that would produce the same parallax  $dp$  obtained from radar for a given object height  $h$ . The exaggeration factor,  $q$ , is formed from equ. (2.9):

In case of a camera we have  $B_n/H_n$  from:

$$B_n/H_n = dpn/hn \quad (2.11)$$

Therefore

$$q = 5 \cdot dpn/hn$$

The ratio  $dp/h$  needs to be found for radar. Using Equ. (2.3) we find for ground range images:

$$qg \approx 5 \cdot (\cot \theta'' + \cot \theta') \quad (2.12)$$

For slant range images we may use equ. (2.7) for the excess parallax of topography above the datum plane:

$$qs \approx ((\sec^2 \theta_o'' - 2h/H)^{1/2} - (\sec^2 \theta_o' - 2h/H)^{1/2} - \sec \theta_o'' + \sec \theta_o') \cdot 5 \cdot H/h \quad (2.13)$$

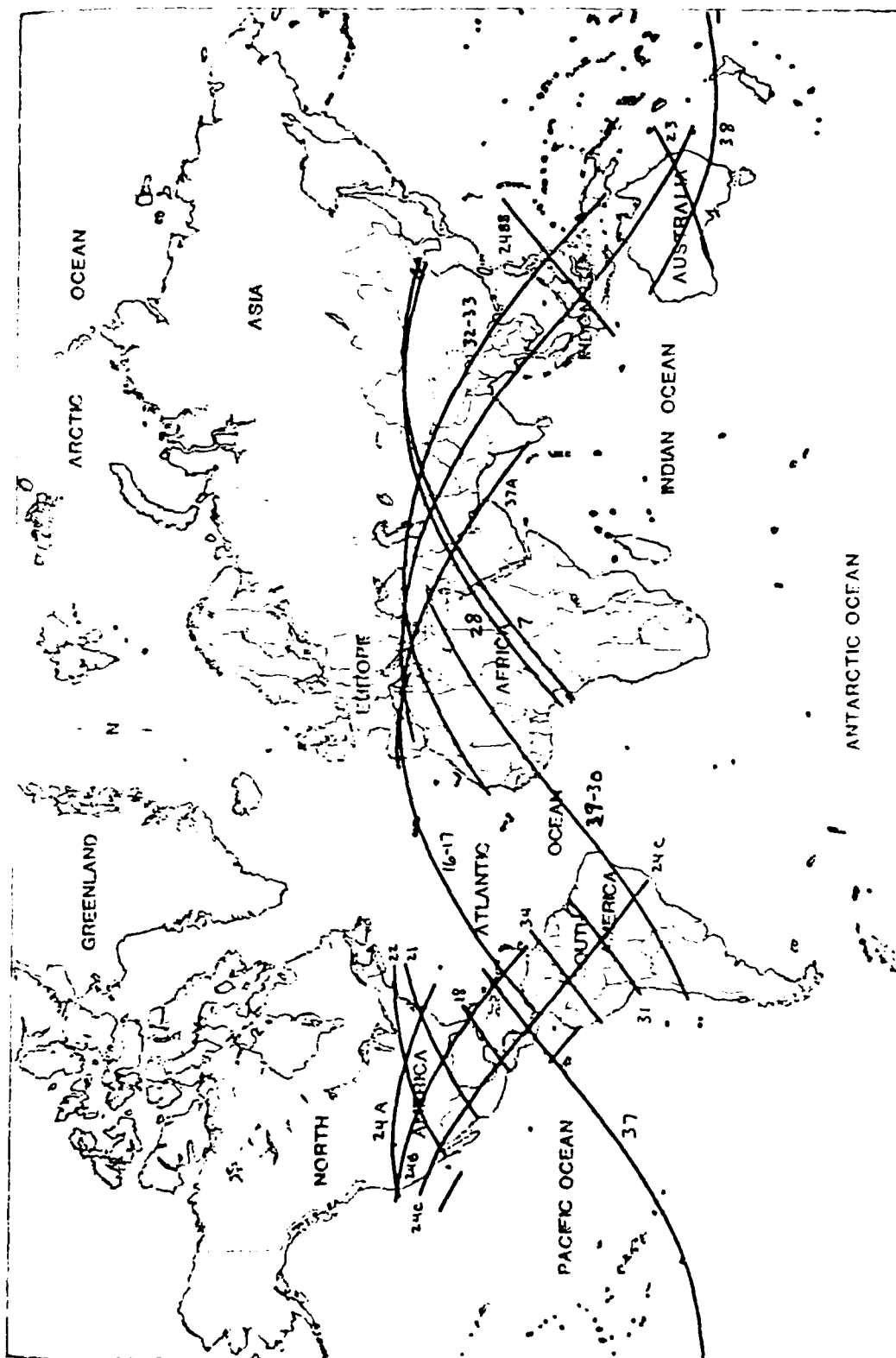


Figure 2.11: Orbit configurations for the Space Shuttle Imaging Radar A (SIR-A) data takes.

We see in table 2.1 that radar stereo parallaxes and exaggeration factors compare well with values obtained from cameras: as look angles become steeper, one has a more accentuated stereo-effect in spite of small stereo intersection angles. This assumes extreme values for a case such as Apollo 17 - ALSE, where very small intersection angles create parallaxes that are multiples of the object height. In camera photogrammetry, the largest parallaxes are of the order of an observed height difference, as  $q$ -values range between 3 and 5.

Factor  $q$  results from a deterministic model of radar stereo parallaxes and addresses the question of an affine stretch of the stereo model. Large exaggeration factors result from large parallaxes but do not ensure high accuracy: the discussion excludes error propagation into measurements of base width,  $w_n$ , and of parallaxes,  $dp$ . Theoretical error considerations were presented by Leberl (1979), these and practical results will be discussed in chapter 6.

## 2.5 Radar Stereoscopy with Non-Parallel Flight Lines

Spaceborne platforms will generally not result in parallel flight lines for overlapping images. Instead there is convergence of the flight lines. A case in example is the Space Shuttle Imaging Radar A (SIR A), as seen in Figure 2.11.

As a result one obtains overlapping images with a particular stereo geometry (Figure 2.12). Stereoscopic viewing is possible; however, the geometry of the stereo case differs from the one discussed in chapter 2.3.

An example of such a stereo image pair is presented in Figure 2.13. This will be discussed in later chapters to a greater extent. The following is an analysis of parallax geometry.

The two convergent stereo partners are observed stereoscopically by placing them in the same way as they were generated, i.e. the flight lines need to intersect under an angle,  $\gamma$ .

As seen in Figure 2.14 one has to differentiate between ground and slant range presentations. Each image contains relief displacement,  $p'$ ,  $p''$ . This combines to form observable stereo parallaxe differences.

Type of Radar	Stereo Base km	Look Angle $\theta'$ ( $^\circ$ )	Intersection Angle $\Delta\theta'$ ( $^\circ$ )	Flying Height H (km)	Parallax Diff. due to h=1km Ground ranges	Exaggeration Factors	
						Ground Ranges qg	Slant Ranges qs
SEASAT	25 75	20 22	1.6 4.8	800 800	0.263 0.761	1.3 3.8	0.05 0.14
Aircraft SAR	0.7 13.5	68 65	0.5 23	12 12	0.011 0.720	0.06 3.6	0.04 1.60
Goodyear Aircraft RAR	10 48	81 80	10 160	4 4	0.215 0.414	1.1 2.1	0.95 2.01
Motorola Apollo 17 ALSE Moon	0.7 3.9 10.0 10.0	10 10 13 13	0.3 1.9 4.7 4.8	116 116 116 116	0.383 3.422 2.584 5.220	1.9 17.1 12.9 26.1	0.00 0.03 0.07 0.08

Table 2.1: Exaggeration factors for radar stereo models related to ground and slant range representations.

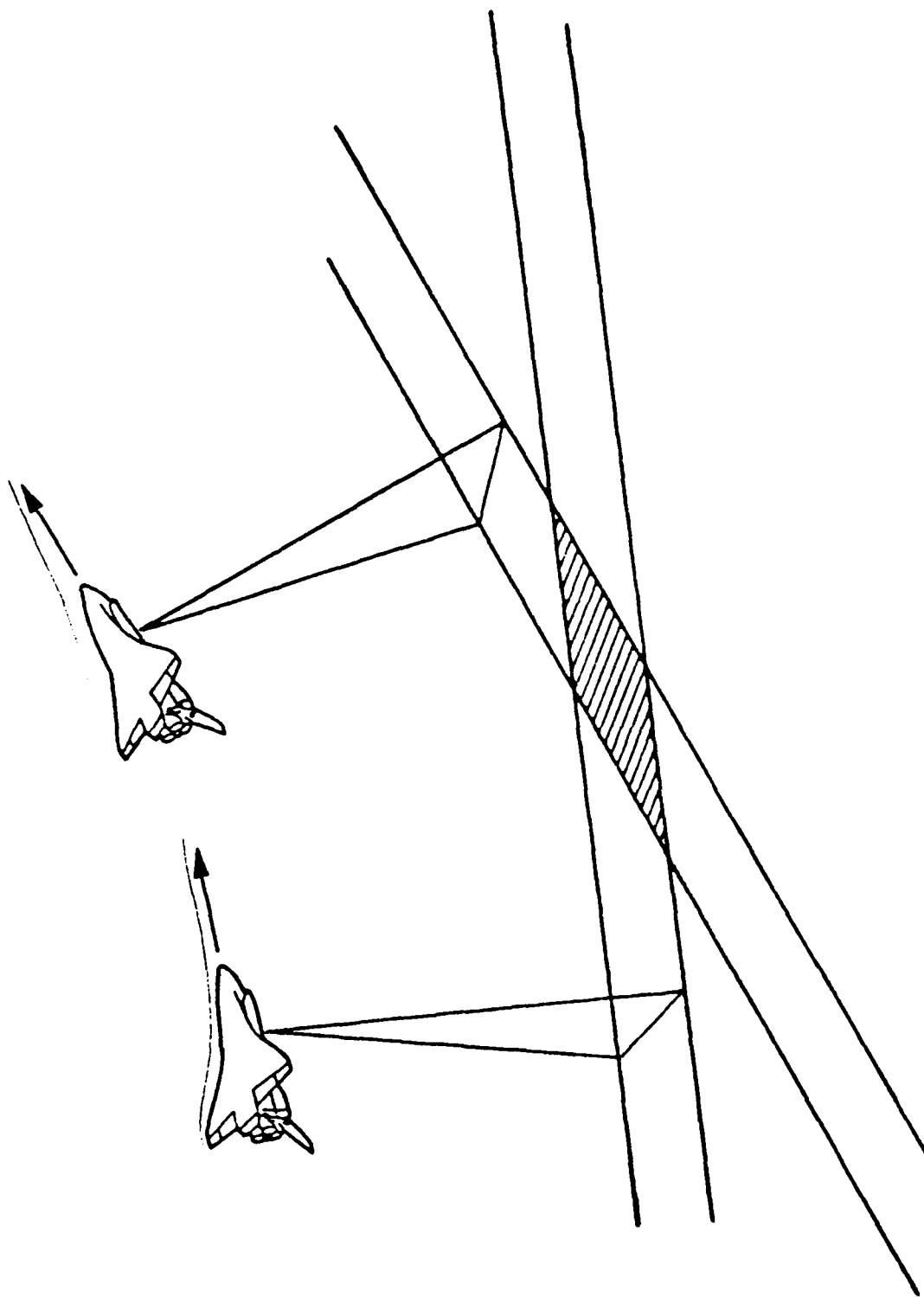


Figure 2.12: Sketch of the imaging geometry for SIR-A convergent stereo.



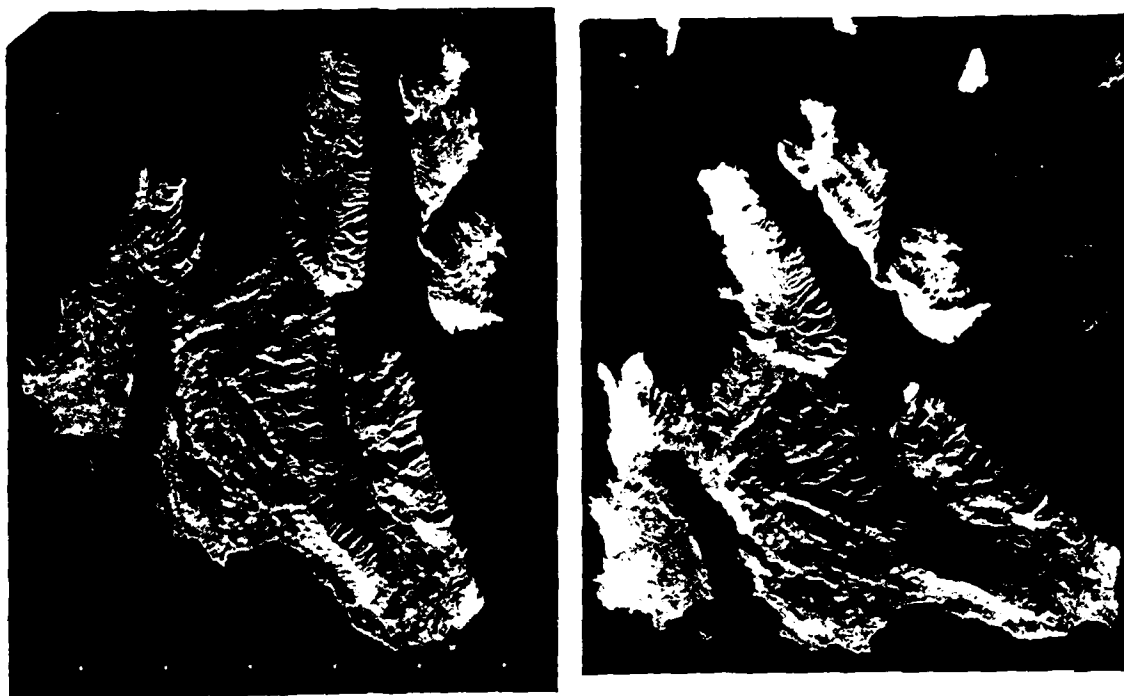


Figure 2.13: Example of stereoscopic radar image pair  
from the SIR-A mission, taken over the Greek  
islands Cephalonia and Ithaka.

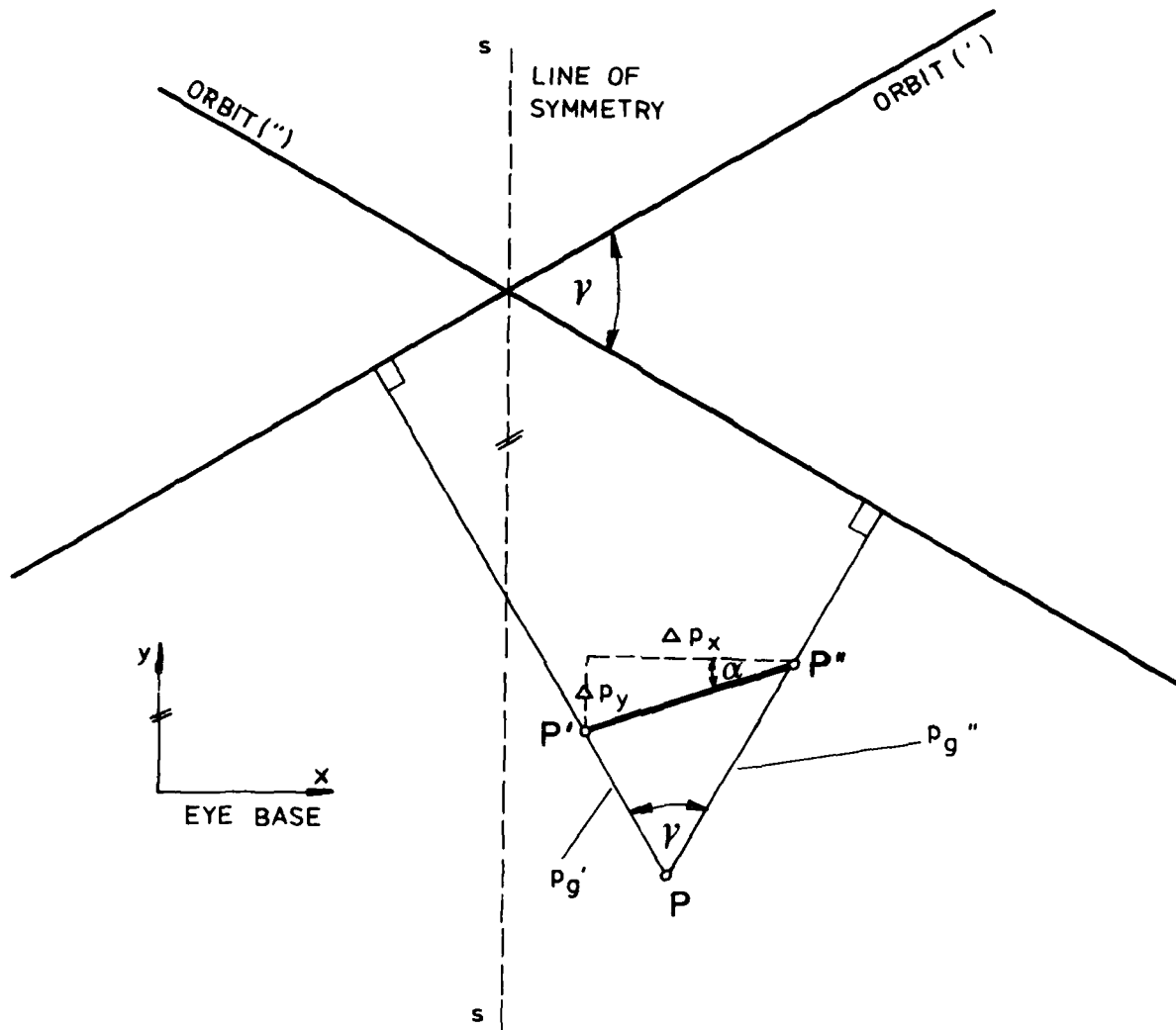


Figure 2.14a: Explanation of radar stereo parallax.  
Ground range presentation.

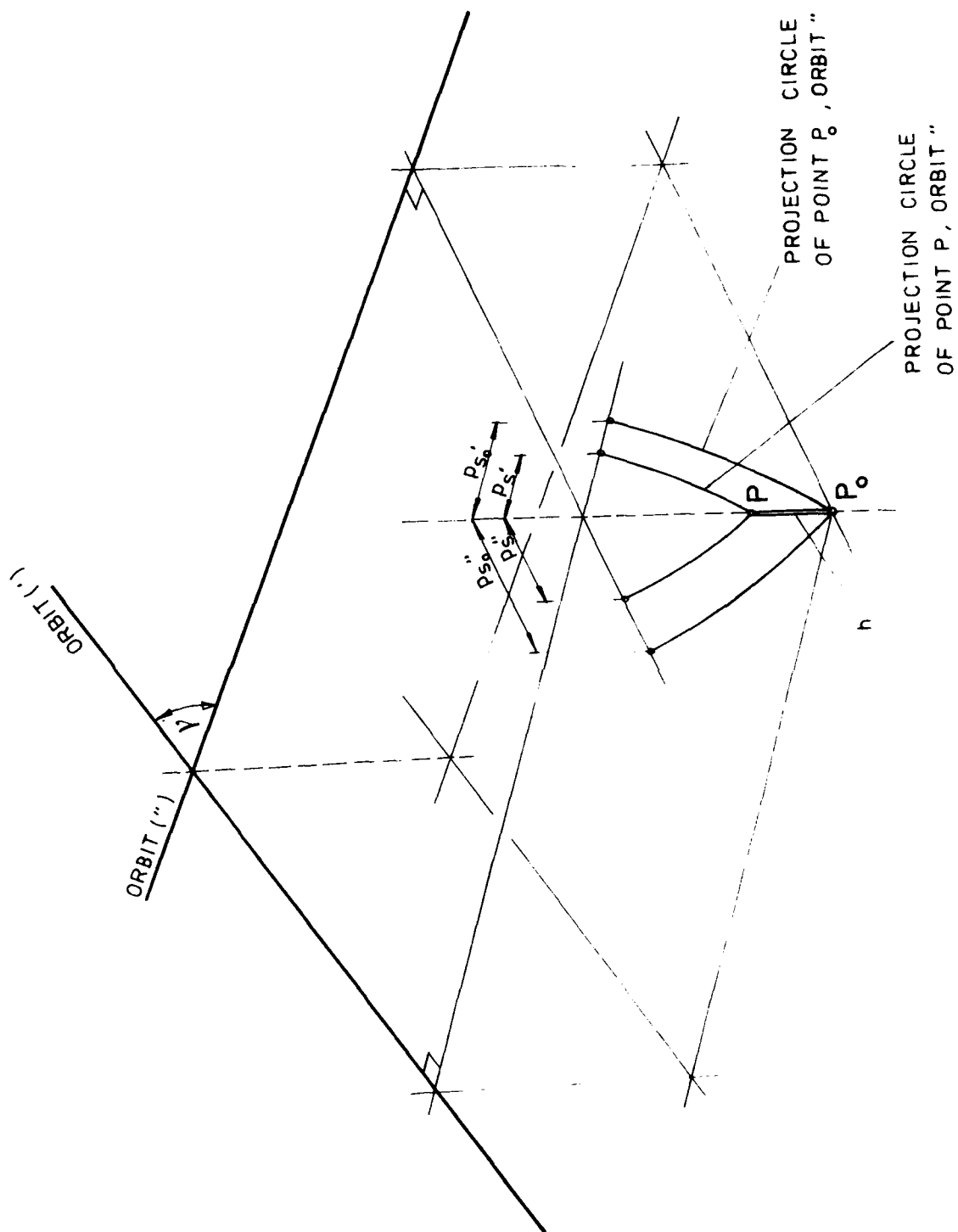


Figure 2.14b: Explanation of radar stereo parallax.  
Slant range presentation.

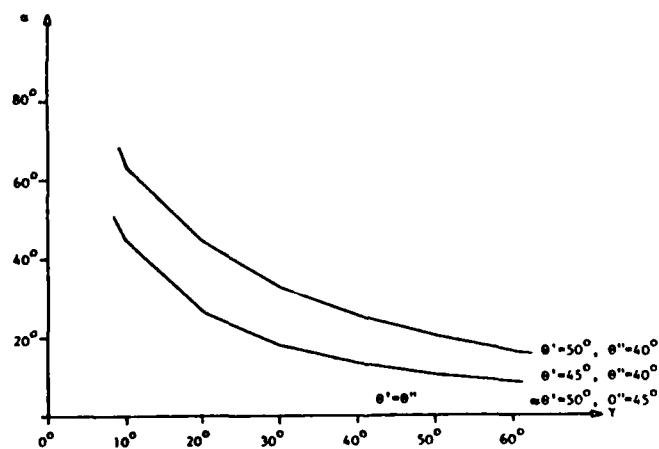
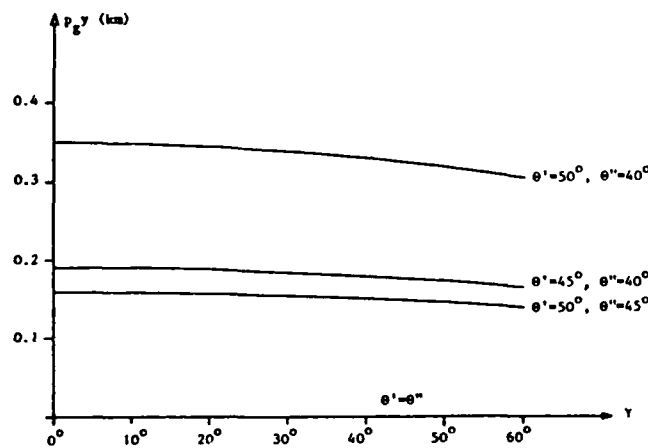
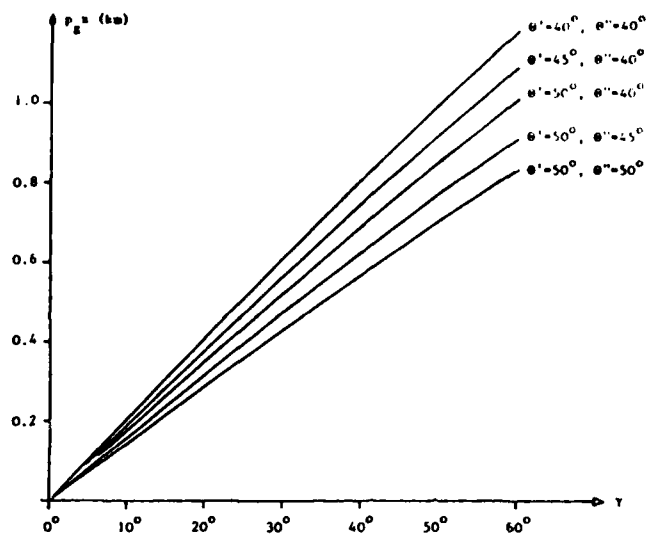


Figure 2.15: Amount of x and y-parallaxes per 1 km height difference for various angles of convergence,  $\gamma$ .

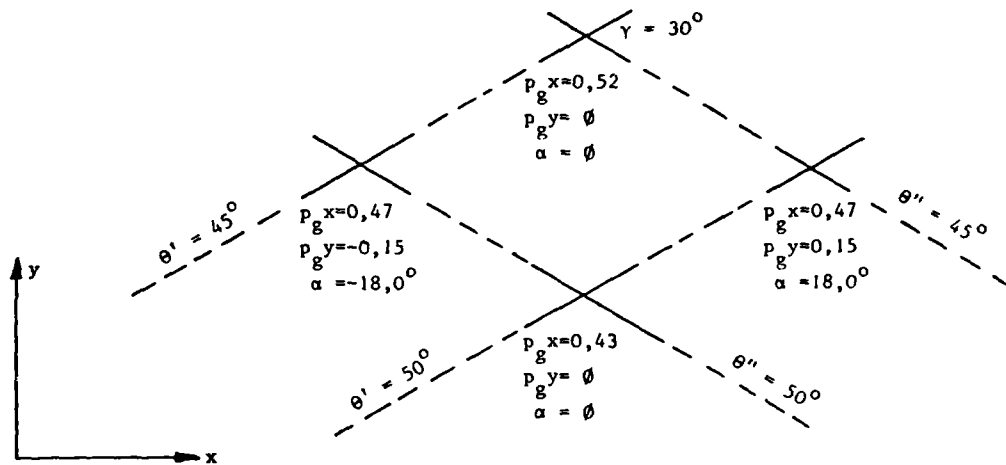


Figure 2.16: Values for parallaxes and rotation of eye base due to 1 km terrain height in the SIR-A Cephalonia stereo model.

(a) Ground range presentation

Figure 2.14 presents the relief displacements in the two images,  $pg'$ ,  $pg''$  and defines a total parallax difference,  $\Delta pgt$ . One needs to attach a coordinate system to the stereo model by defining an x-axis parallel to the eye basis and y at a right angle. The eye basis is normal to the line of symmetry, ss. Parallax differences  $\Delta pgt$  have components in x and y. We find:

$$pg' = ((r'^2 - (H-h)^2)^{1/2} - (r'^2 - H^2)^{1/2}) \approx h.H / (r'^2 - H^2)^{1/2}$$

$$pg'' = ((r''^2 - (H-h)^2)^{1/2} - (r''^2 - H^2)^{1/2}) \approx h.H / (r''^2 - H^2)^{1/2}$$

$$\Delta pgt = (pg'^2 + pg''^2 - 2pg' pg'' \cos \gamma)^{1/2} \quad 2.14$$

$$\Delta pgx = (pg'' + pg') \sin \gamma / 2 \quad 2.15$$

$$\Delta pgy = (pg'' - pg') \cos \gamma / 2 \quad 2.16$$

For ground points not on line ss one finds a y-parallax,  $pgy$ . This could be eliminated by rotating the eye basis for an angle  $\alpha$ :

$$\alpha = \arctan \Delta pgy / \Delta pgx \quad 2.17$$

Equations 2.14 through 2.17 must be qualitatively evaluated. Fig. 2.15 presents curves showing the amount of x and y parallax per 1 km height difference for various values of the convergence angle  $\gamma$  and look angles  $\Omega'$ ,  $\Omega''$ .

In the case of the Cephalonia stereo model, we find extreme values of  $\Delta pgy$  or  $\alpha$  as follows:

$$\Delta pgy \text{ max} = 150 \text{ m}$$

$$\alpha_{\text{max}} = 18^\circ$$

These values can be neglected for stereoscopic viewing. From the above equations of  $\Delta pgx$  we obtain the terrain height, h:

$$h \approx \Delta pgx \cdot \tan \Omega / (2 \cdot \sin \gamma / 2) \quad 2.18$$

(b) Slant range presentation

As with parallel flight lines we find also in convergent cases parallax differences for a flat area. One therefore needs to separate the observed parallaxes into one due to the actual relief,  $\Delta p_s$ , and into the systematic component,  $\Delta p_o$ .

Figures 2.14 show that:

$$p_o' = r_o' - (r_o'^2 - H^2)^{1/2} = H / \cos \Omega_o' - H \tan \Omega_o'$$

$$p_o'' = r_o'' - (r_o''^2 - H^2)^{1/2} = H / \cos \Omega_o'' - H \tan \Omega_o''$$

$$\Delta p_o = (p_o'^2 + p_o''^2 - 2p_o' p_o'' \cos \gamma)^{1/2}$$

$$p_s' = r' - (r'^2 - (H-h)^2)^{1/2} = (H-h) / \cos \Omega' - (H-h) \tan \Omega' \quad 2.19$$

$$p_s'' = r'' - (r''^2 - (H-h)^2)^{1/2} = (H-h) / \cos \Omega'' - (H-h) \tan \Omega'' \quad 2.20$$

$$\Delta p_s = (p_s'^2 + p_s''^2 - 2p_s' p_s'' \cos \gamma)^{1/2}$$

$$\Delta p_{sh} = \Delta p_o - \Delta p_s$$

We find a situation that is analogous to that with ground range presentation. In the vicinity of the line of symmetry, ss, we can simplify:

$$h \approx \Delta p_{sh} \cdot \cos \Omega / \{ 2 (1 - \cos \gamma)^{1/2} (1 - \sin \Omega) \} \quad 2.21$$

where  $\Delta p_{sh}$  results from EQ. 2.20 and represents the parallax difference above the deformed reference surface.

In light of satellite radar data to be taken in polar regions (Antarctica) or on other planets (Venus Radar Mapper), these considerations promise to be of some relevance.

Experimental analysis of stereo viewability of this imaging configuration will therefore be included in subsequent chapters.

### 3. Image Simulation Approaches

Various algorithms can be used for radar image simulation. These need to be compared to develop a technique for use of simulated radar images in place of real ones for a stereo parameter study. Emphasis therefore is on the correct image geometry, and on the use of those parameters that are critical to stereo viewing. Radar image simulation has been previously studied by several authors. Holtzman et al. (1978) concentrate on simulating backscatter effects but neglect geometric effects due to topographic relief; Kaupp et al. (1982) concentrate on geometry for stereo studies, but neglect the details of squint and flight arrangements different to the classical same side or opposite side stereo. The current system should allow one to study stereo viewing and varying all parameters that have an effect including squint imaging and different flight arrangements.

The task of image simulation may be split up into two separate tasks. Unruh and Mikhail (1981) describe this as follows:

"The imaging model is actually two separate models. One, a geometric model, relates physical points in object space to physical points on the image. The other, a spectrometric model, relates object attributes at an object point to image brightness at the corresponding image point."

These two models -- the geometric model vs. the radiometric model, in our terminology -- present transformations between object and image spaces.

In the process of generating a synthetic image one has to relate to each object point a corresponding image point (geometric model); two types of algorithms can be employed, the so-called "Object-" and "Image Space Algorithms". Approaches are discussed in the following.

#### 3.1 Object Space Algorithm

##### (a) General Description

Simulation is based on the Cartesian coordinates of the points in a DEM (Digital Elevation Model) and on sensor positions expressed in the same system. After applying the imaging equations to each object point one obtains



irregularly spaced image points. We designate the along-track coordinate as "row" and the range as "column". Sensor position therefore defines the row coordinate, and the calculated range between sensor and object point defines the column coordinate. Since the respective image points are irregular, one must interpolate to create a regularly spaced output. An object space algorithm uses the exact values of the object DEM points. Output values are converted to regularly spaced image points (Fig. 3.1).

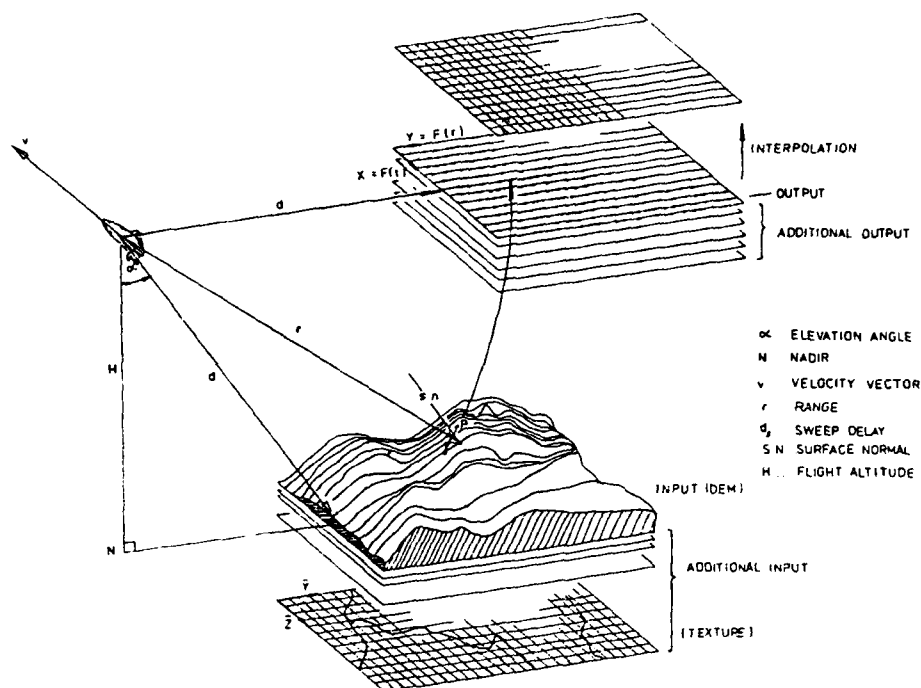


Figure 3.1 : Set-up for an object space algorithm: imaging is in a plane perpendicular to the flight path (denoted by the velocity vector  $v$ ). The output values are converted to regularly spaced image points.

#### (b) Example

The following is a simplified version of an object space algorithm. The input consists of a DEM with equally spaced grid points. The flight path is a straight line perpendicular to the profiles of the DEM at a constant altitude. The radar beam is directed at an angle perpendicular to the flight path (squint angle  $\epsilon = 0$ ). All distances and positions are defined in the same three-dimensional Cartesian coordinate system.

We find range  $r$  between a sensor position and object point  $P=(p_x, p_y, p_z)$  according to Figure 3.2:

$$r = \text{SQRT}((H - p_z)^2 + d^2) \quad \text{EQ. (3.1)}$$

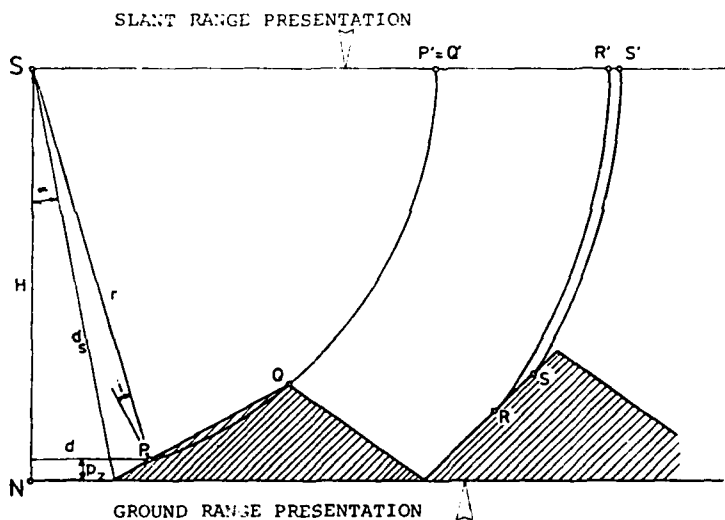
The DEM point to be imaged first determines the sweep delay  $s_d$ , the range  $r$  between sensor position and any other DEM point along the profile determines the image column coordinate  $j$  by

$$j = \text{INT} \left( (r - s_d) / f_j \right) \quad \text{EO. (3.2)}$$

where  $f_j$  is the image scale factor in range direction.

The image row  $i$  is determined by the sensor position and thus by the DEM profile itself.

This simple approach presents the user with such typical image geometry effects as layover, foreshortening and radar shadows.



$\alpha$	elevation angle	H	Flight altitude
$i$	incidence angle	r	slant range
N	Nadir	$d_s$	sweep delay
$\overline{RS} - \overline{R'S'}$	foreshortening	d	Distance between Nadir and P
$P' = Q'$	lay-over	$p_z$	Height of P above ground

Figure 3.2 : Imaging in a plane perpendicular to the flight path

(c) Arbitrary Flight Path and Squint Angle

However, a need may exist to simulate an image when a flight track or actual satellite orbit are known. One would have discrete times and the corresponding sensor positions. The flight path could be expressed by an ellipse, by splines, polynomials or by polygons when simply connecting the given positions. This serves to relate any time  $t_k$  during the imaging phase to a sensor position  $\underline{s}_k$ ; where we express any sensor position  $\underline{s}$  in a local coordinate system  $(x, y, z)$

$$\underline{s} = \underline{s}(t) = (s_x(t), s_y(t), s_z(t)).$$

Imaging is in a so-called zero-Doppler plane that is perpendicular to the corresponding velocity vector, the first derivative of  $\underline{s}$ :

$$\underline{\dot{s}} = \underline{\dot{s}}(t) = (\dot{s}_x(t), \dot{s}_y(t), \dot{s}_z(t))$$

Both  $\underline{s}$  and  $\underline{\dot{s}}$  are a function of time  $t$ .

A surface of constant doppler shift is in general a cone. This is denoted by a squint angle  $\epsilon \neq 0$ . With  $\epsilon = 0$  the cone degenerates to a plane.

With ground point  $P = (p_x, p_y, p_z)$ , a sensor position  $\underline{s}$  with the squint angle  $\epsilon$ , and velocity  $\underline{\dot{s}}$ , we find from Figure 3.3 that a relation exists between  $\underline{p}$ ,  $\underline{s}$ ,  $\underline{\dot{s}}$  and  $\epsilon$ :

$$\frac{\underline{\dot{s}}}{|\underline{\dot{s}}|} \cdot \frac{(\underline{p} - \underline{s})}{|\underline{p} - \underline{s}|} = \cos(90^\circ - \epsilon) = \sin \epsilon \quad \text{EO. (3.3)}$$

Assuming  $\underline{s}$  and  $\underline{\dot{s}}$  to derive from polynomials in  $t$ , this equation can be solved for every point  $P$  of the ground to be imaged. The solutions are the set of  $\{t_k, k=1, \dots, m\}$ . It is a mathematical problem, that the closer the flight path is approximated by the polynomial, the more it oscillates. This leads to a quantitatively big set of solutions, from which a subset of possible solutions have to be extracted. This is no trivial task. This subset  $\{t_l, l=1, \dots, n \mid n < m\}$  determines sensor positions  $\underline{s}_l$ .

From a specific position  $\underline{s}$  at time  $t$  the slant range  $r$  is

$$r = |\underline{p} - \underline{s}| \quad \text{EO. (3.4)}$$

This is displayed in a slant range presentation. In a ground range presentation one finds the column coordinate  $a$

as

$$q = \text{SQRT}(r^2 - H^2)$$

EQ. (3.5)

where  $H$  is meant to be the altitude of the sensor at imaging time  $t$ . It is thus the current value at the time of flight.

Time ( $t$ ) defines the image row (azimuth coordinate), whereas ( $r$ ) respectively ( $q$ ) define the image column or range coordinate. (See EQ. 3.2)

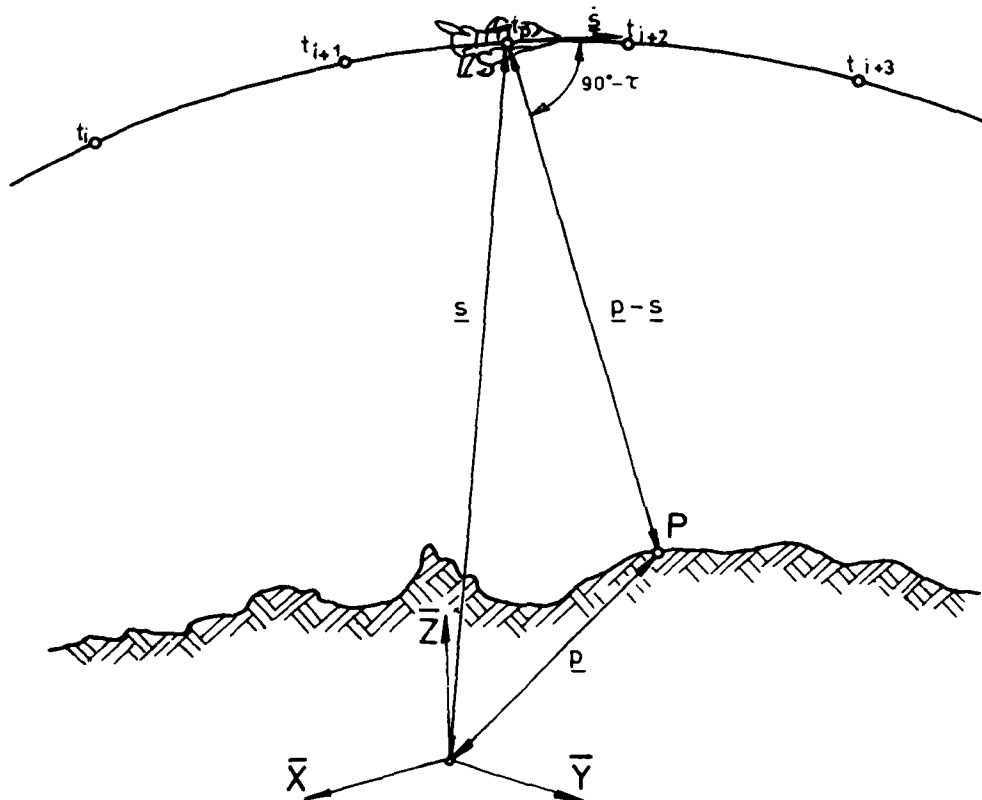


Figure 3.3 : The beam from the sensor to a ground point forms an angle of  $(90^\circ - \tau)$  with the velocity vector.

### 3.2 Image Space Algorithm

#### (a) General Description

The image space approach starts from equidistant image coordinates  $(i,j)$  of the output image. Radar imaging time  $t$  and range  $r$  can be derived from these coordinates and define a projection circle. The corresponding object point(s) in the DEM must be found by intersecting the circle with the DEM. The intersecting points are usually not exact DEM grid points; the intersection of arc and ground is thus found by interpolation. This kind of approach is useful when object space points must be associated with previously specified image locations directly (See Greeve and Coonev, 1974).

#### (b) Deriving sensor position $\underline{s}$ and range $r$ from image coordinates

The coordinates  $(i,j)$  in the output image serve as input values for the simulation program, where  $(i)$  is a function of time  $(t)$  and  $(j)$  is a function of slant range  $(r)$  or ground range  $(g)$ . We find:

$$t = (i-1)*f_i + t_0 \quad \text{EQ. (3.6a)}$$

$$r = (j-1)*f_j + s_d \quad \text{EQ. (3.6b)}$$

$$g = (j-1)*f_j + s_d$$
$$r = \text{SQRT}(H^2 + g^2) \quad \text{EQ. (3.6c)}$$

where

$t$ ....imaging time of coordinate  $(i,j)$   
 $t_0$ ...start time of imaging  
 $f_i$ ...scale factor in azimuth-direction  
 $f_j$ ...scale factor in range-direction

The platform position  $S$  (described by vector  $\underline{s}$ ) and the corresponding velocity vector  $\underline{\dot{s}}$  can be calculated as functions of  $t$ .

(c) Local vs. sensor coordinate system

The relationship between sensor and ground points  $P$  is shown in Fig. 3.4. One has to work with several coordinate systems. Point  $P$  is defined as  $P=(p_x, p_y, p_z)$  in a Cartesian coordinate system  $(x, y, z)$ ; the origin is placed on a suitable point on the earth's surface,  $z$  is the local vertical direction at the origin.

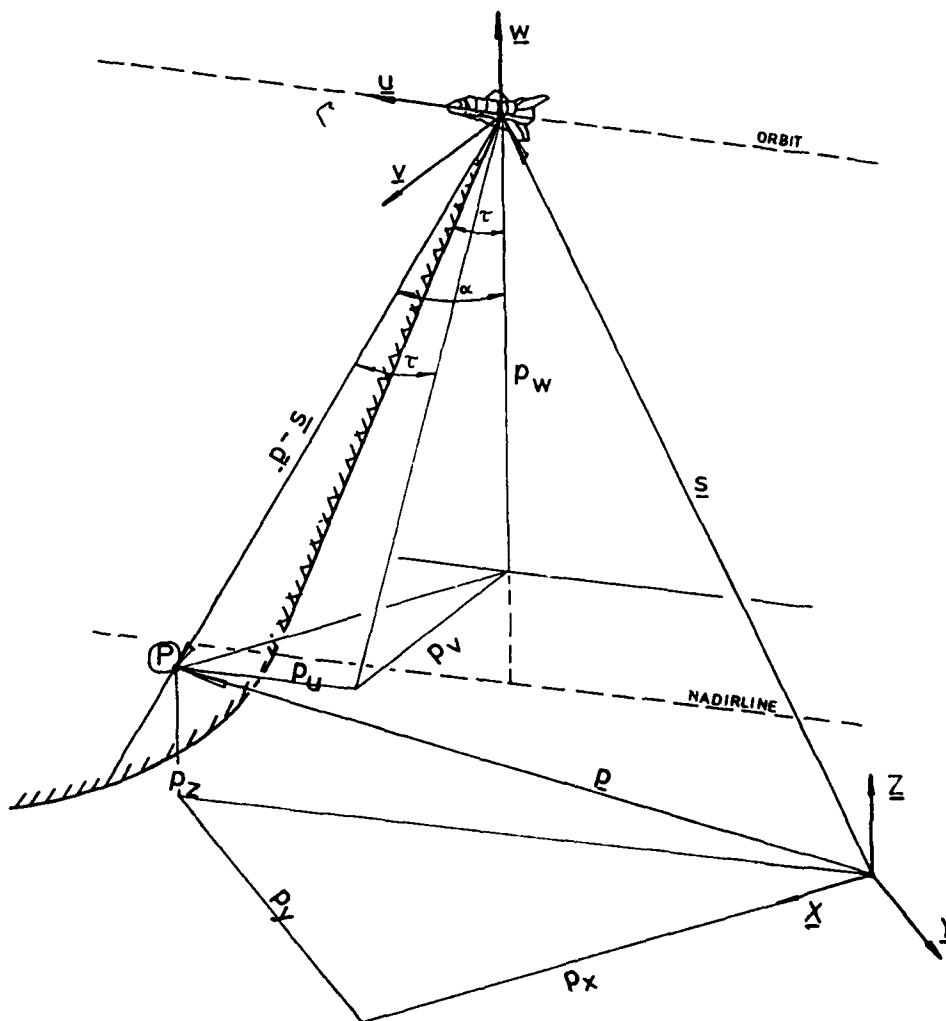


Figure 3.4 : Ground point  $P$  in two coordinate systems

In addition one has an antenna (sensor) coordinate system  $(u,v,w)$  with the origin at the platform position and  $u$  along the platform velocity vector.  $P$  has the coordinates  $\underline{p} = (p_u, p_v, p_w)$ , the relationship between platform position and point  $P$  to be imaged in the local coordinate system is defined by EQ. (3.3).

The antenna coordinate system is defined by three unit vectors  $\underline{u}, \underline{v}, \underline{w}$ :

$$\begin{aligned}\underline{u} &= \underline{s}/|\underline{s}| \\ \underline{v} &= (\underline{s} \times \underline{s})/|\underline{s} \times \underline{s}| \\ \underline{w} &= (\underline{u} \times \underline{v})/|\underline{u} \times \underline{v}|\end{aligned}\quad \text{EQ. (3.7)}$$

EQ. 3.3 degenerates to

$$\underline{u} \cdot \underline{p} = r \cdot \sin \epsilon \quad \text{EQ. (3.3)}$$

in this coordinate system.

Introducing the elevation angle  $\theta$  the following relationships exist between the coordinates  $p_u, p_v, p_w$ , elevation angle  $\theta$  and the squint angle  $\epsilon$ :

$$\begin{aligned}p_u &= r \cdot \sin \epsilon \\ p_v &= r \cdot \text{SQRT}(\sin^2 \theta - \sin^2 \epsilon) \\ p_w &= -r \cdot \cos \theta\end{aligned}\quad \text{EQ. (3.9)}$$

EQ.(3.3), EQ.(3.9) and EQ.(3.8) are alternative formulations of the relationship between the existing parameters.

As both of the coordinate systems are cartesian, the conversion between the local and the antenna system consists of a shift and rotation with shift vector  $\underline{q}$  and a rotation matrix  $R$ .

$$(p_u, p_v, p_w) = R \cdot ((p_x, p_y, p_z) - \underline{q}) \quad \text{EQ. (3.10a)}$$

or in the other direction:

$$(p_x, p_y, p_z) = R^T \cdot (p_u, p_v, p_w) + \underline{q} \quad \text{EQ. (3.10b)}$$

( $\underline{q}$  is of course found to be  $\underline{s}$  and  $R$  to be  $(u^T, v^T, w^T)$ , all expressed in the local Cartesian system).

$R^T$  is the transposed matrix of  $R$ .

(d) Range Sphere and Doppler Cone; Intersection Circle

Any image point creates thus the following geometry:

Time  $t$  (derived by the image row coordinate  $i$ ) defines the sensor location  $S$  and its velocity vector  $\underline{s}$ .  $(\underline{s}, \underline{s}; t)$  determine a cone (Doppler cone), whose peak is in  $S$ , and all generating lines form an angle of  $(90 - \epsilon)$  with  $\underline{s}$ .

The range column  $j$  defines the slant range  $r$  and creates a sphere with the radius  $r$  around its center  $S$ . Intersection of the sphere and cone define a circle as illustrated in Figures 3.5 and 3.6. We define the sphere  $(s, r)$ :

$$u^2 + v^2 + w^2 = r^2 \quad \text{EQ. (3.11)}$$

The cone  $(s; \underline{u}; \epsilon)$  is

$$(v^2 + w^2) / r^2 \cos^2 \epsilon - u^2 / r^2 \sin^2 \epsilon = 0 \quad \text{EQ. (3.12)}$$

The intersection of cone and sphere defines a circle:

$$v^2 + w^2 = r^2 \cos^2 \epsilon \quad \text{EQ. (3.13)}$$

in the plane

$$u = r \sin \epsilon.$$

Each image point then represents a circle that needs to be intersected with the ground. In the simulation task, this is an intersection between circle and DEM.



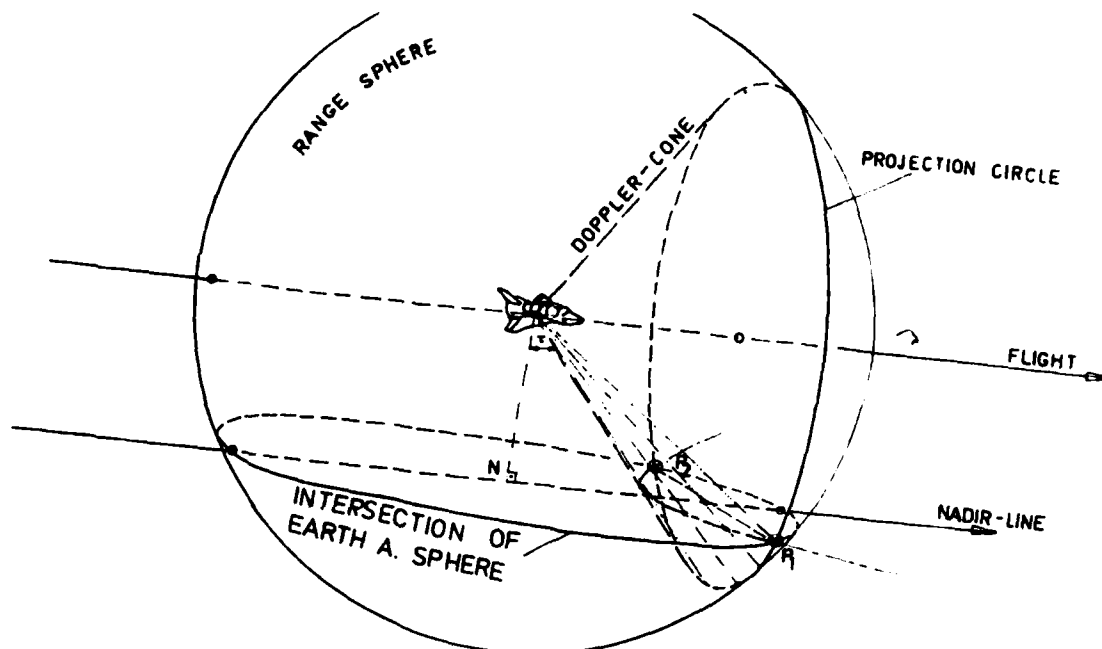


Figure 3.5: Doppler cone and range sphere.  
Perspective view.

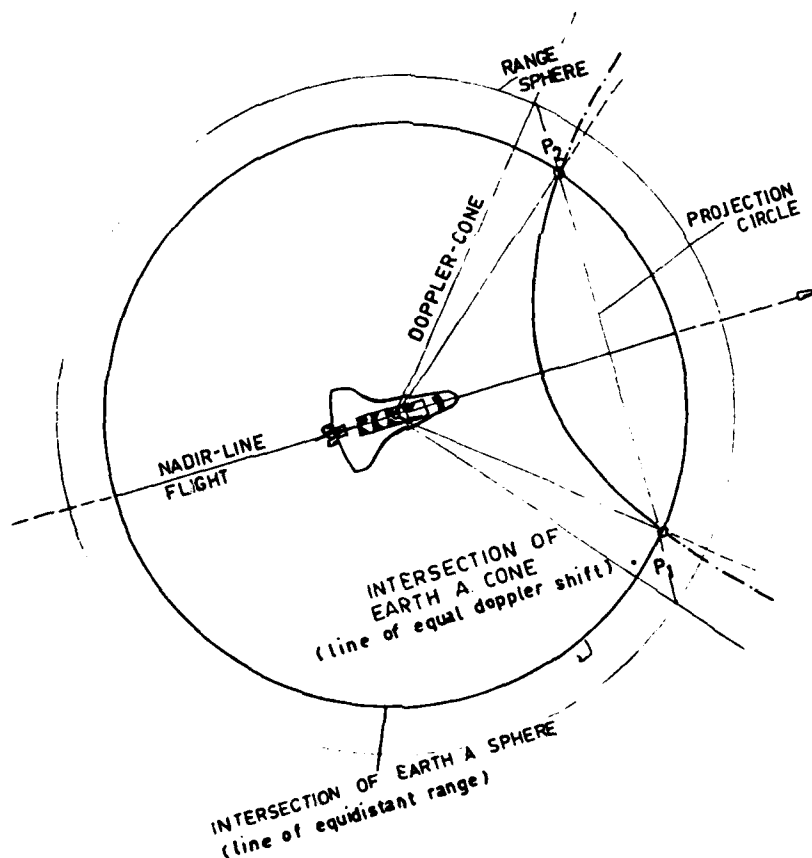


Figure 3.6: Doppler cone and range sphere.  
Vertical view.

#### (e) Intersecting the Projection Circle with the DEM

The intersection between circle and DEM is found in two steps. Let a ray from S form an angle  $\theta$  with the nadirline. Its intersection with the projection circle produces position  $p(\theta) = (p_u, p_v, p_w)\theta$  using EQ. (3.7). In a next step  $p$  is converted to  $\underline{p} = (p_x, p_y, p_z)\theta$  using EQ. (3.9b). Height  $p_z$  can be compared with real height  $z$  at planimetric position  $(p_x, p_y)$  where  $z$  is approximated linearly by the four DEM corner points. By changing  $\theta$  monotonously increasing or decreasing, the intersection points will be below or above the actual terrain; the change-over from below to above or vice versa indicates an intersection within an interval  $[\theta_i, \theta_{i+1}]$ . Then this new interval is subdivided and the computations are continued to define the intersection point more precisely. Finally the DEM segment  $[\theta_i, \theta_{i+1}]$  is approximated by a plane and intersected with the circle.

Each circle has to intersect the DEM at least once, but more than one solution is possible and meaningful. The occurrence of more than one solution is due to the "lay-over": more than one DEM point is to be imaged. In other words: more than one ground point has a given range  $r$  from a platform position.

#### (f) Arbitrary Flight Path and Squint Angle

The approach used for image simulation with the image space algorithm defines a flight path in one of several forms: lookup tables, polynomials, splines etc. It is merely the problem of relating the image time to the corresponding sensor position. This allows one to enter flight perturbations (pitch, yaw) and to study their effect on the image.

Imaging with  $\xi = 0$  as well as  $\xi \neq 0$  is possible. However, for the latter case there is a need to additionally rectify the image.

#### (g) Geometric Rectification of Squint Angle Images

All points imaged from one sensor position are found in one image line. In the case of  $\xi = 0$  the corresponding object points were lined up in a plane perpendicular to the flight path and distortions appear in the range direction resulting from the height variation on the ground. In the

other case, however, the imaged points appear in the object space as elements of a cone (the Doppler cone) and thus the image pixel locations have to be rearranged as to where they would appear in the case of imaging with  $\xi = 0$ . The rectification is explained in Fig. 3.8 for a forward looking squint: All intersection points of DEM and cone appear in one image line, as they are imaged from the same sensor position  $S$ .

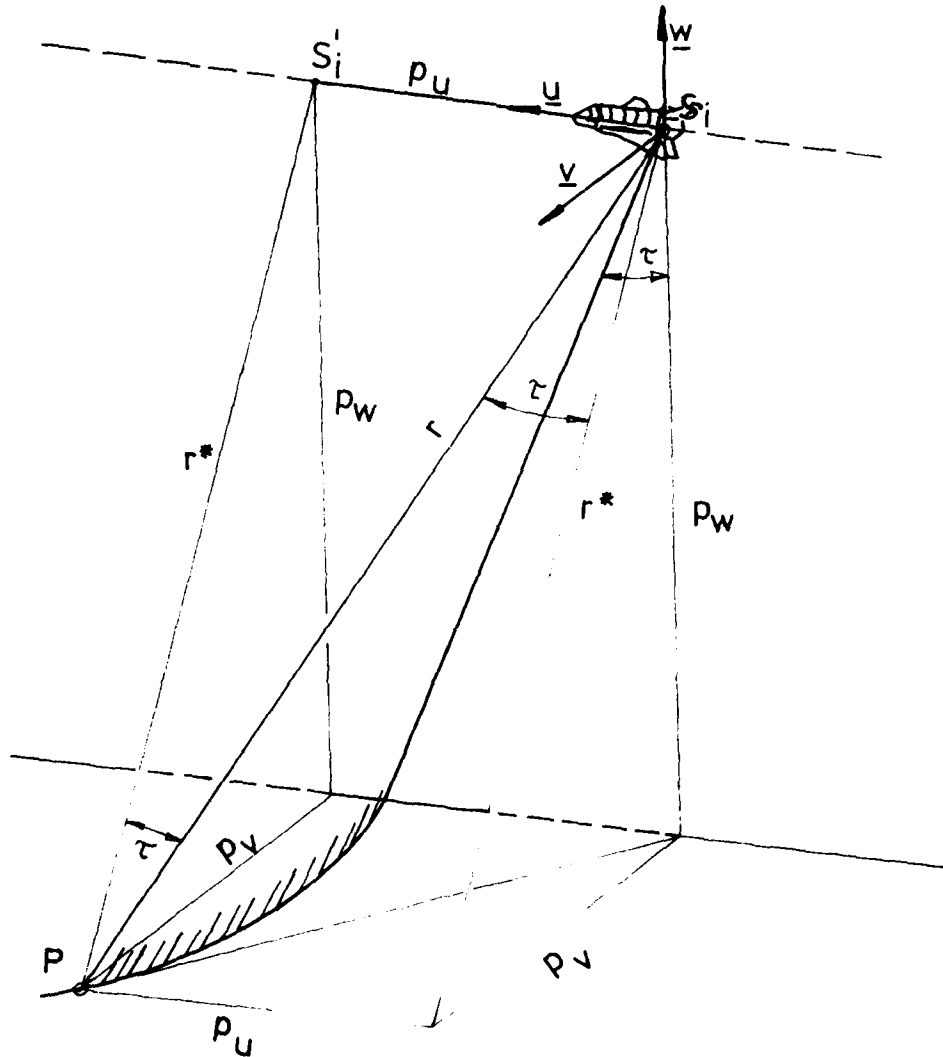


Figure 3.7: Rectifying "squint angle" images geometrically: new sensor position  $S_i'$  and new range ( $r^*$ )

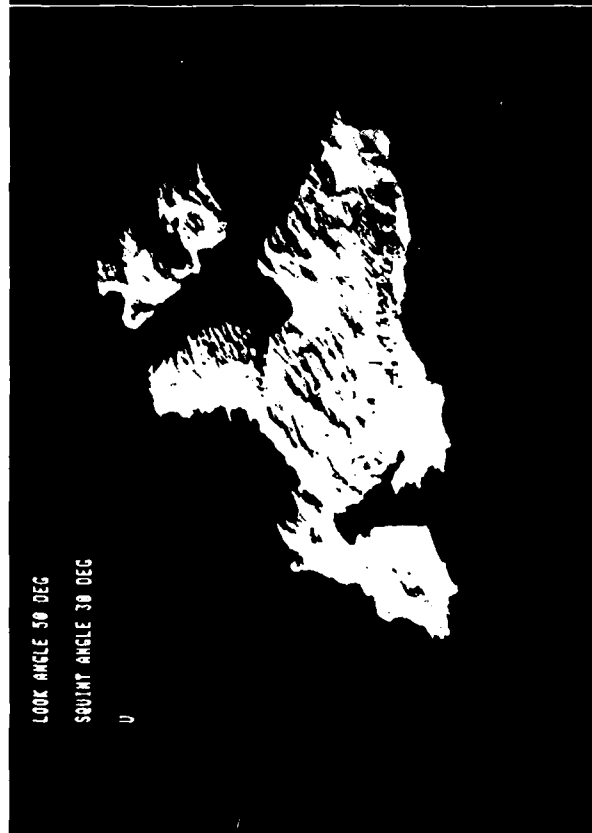
All intersection points of DEM and cone appear in one image line, as they are imaged from the same sensor position  $S_i$  ( $S_i$  = peak of cone at imaging time  $t_i$ , where  $t_i$  is the time of imaging row  $i$ ). The location where the image of one DEM point  $P$  lies within this line is dependent on the distance  $r$  between  $S_i$  and  $P$ . Without squint angle point  $P$  would have been imaged from another position,  $r \cdot \sin \xi$  different. Considering the scale factors in azimuth and range direction, image point  $P'$  should be moved forward to this new image line. For a slant range presentation the new range  $r^* = r \cdot \cos \xi$  determines the image column of the rectified image.

Fig. 3.8 show a simulation result of using a squint angle  $\xi = 30^\circ$ . Other parameters for this simulation are

Flight altitude = 264 km  
Elevation angle to near range =  $70^\circ$ .

Text for Figures 3.8 (a), (b) and 3.9 on next page:

Fig. 3.8 (a) is the raw simulation result, Fig. 3.8 (b) shows the image after rearranging the image pixel locations to the geometry of  $\xi = 0$ . The radiometric distortions caused by the squint cannot be rectified. For comparison, Fig 3.9 is a presentation of a simulation without squint angle, but with exactly the same other imaging parameters.



a

47

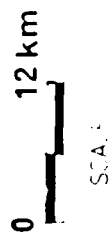


b

3.8



3.9



### 3.3 Radiometric Model

Once the relationship between image and object coordinates is established one can proceed to assign density numbers to each location. These values will vary between black (shadow) and white (target reflecting specularly towards the sensor).

#### (a) Shadow

The determination of areas in radar shadow is a hidden surface problem. Hidden surface elimination is well documented (e.g. Sutherland et al, 1974). The problem remains to find a fast algorithm for each special application.

Hidden surface computations always imply some kind of sorting. In the case of an object space algorithm moving along the DEM profiles from near to far range, the array is already presorted and shadow areas can be easily found by the following method.

For each point P the incidence angle  $\theta^i$  (defined as the angle between the surface normal at P and the line between sensor and P) is calculated. If  $\theta^i$  passes  $90^\circ$  in P, then a straight line from the sensor through point P is used to compute intersection point Q. The area from P to Q is in the shadow. At Q the imaging computations continue.

Other algorithms prove to be more difficult to use since no information is available at imaging time if a DEM point is hidden by other parts of the DEM or not.

Therefore the shadow is computed in a post-processing step. Imaging results in information on corresponding image pixels and DEM cells such as elevation angles and distances from nadir line. These must be sorted with respect to the corresponding time rows and range columns. Sorting in time rows is needed since DEM cells are only hidden by other DEM cells that are seen from the same sensor position.

Sorting along the range column is in two steps. First, points are sorted with increasing ground distance from nadir. Second, a check is performed on the elevation angles for strictly increasing values. For non-increasing values of the elevation angle the corresponding image pixels represent radar shadow.

The imaging technique always results in an almost presorted data field. With "Quicksort", (Hoare, 1962) one of the classical very fast sorting algorithms, the computing time would be  $O(n * \log_2 n)$  for a best case, where  $O$  means "in the order of", and  $n$  is the number of elements to sort. It is not applied because of its property to increase computing time for presorted arrays (Maurer, 1974). "Heapsort" (Williams, 1964) was applied instead; this method has a worst case of  $O(n * \log_2 n)$  once the field is changed into a heap, and proves to be negligible in CPU time for this application.

#### (b) Assigning Grey Values

The grey value to be assigned to an image coordinate  $(i,j)$  is a function of the incidence angles  $\theta^i$  appearing at the corresponding ground points. The angle enters into a backscatter function  $\phi(\theta^i)$ .

The incidence angle is defined as the angle between two vectors, namely the normal onto the DEM and the incidence ray, ( $p-s$ ) (ray from sensor position  $S$  to ground point  $P$ ). In the current context of stereo studies it was considered sufficient to use one backscatter function for an entire image. One could, however, define different such functions depending on planimetric positions  $x,y$  in the DEM. This would allow one to differentiate between e.g. forest, sand, water, ice, etc. However this would imply the existence of thematic information in addition to the mere topographical data in the DEM.

So far standard backscatter functions of Hagfors (1969) or Muhleman (Kobrick, 1982, personal communication) and a cosine function have been used according to EO's. 3.14:

$$\phi_{HAG} = \log_{10} \sqrt[3]{\frac{1}{(\cos^4 \theta^i + C \sin^2 \theta)^3}} \quad \text{Eq. (3.14a)}$$

$$\phi_{MUL} = \log_{10} \left[ \frac{\cos \theta^i * A^3}{(\sin \theta^i + A \cos \theta^i)^3} \right] \quad \text{EO. (3.14b)}$$

$$\phi_{COS} = \cos \theta^i \quad \text{EO. (3.14c)}$$

where

C ... is Hagfors' constant  
A ... is Muhleman's alpha

The resulting  $\phi$ -values must be converted to digital density numbers DN.

### 3.4 Discussion and Choice of Implementation

The algorithm design was the result of experiments with a simplified simulation using the object space approach. Shadowing can be included. This type of simulation is a useful and fast tool if no geometric perturbations must be studied.

A more generally applicable approach is with the use of an image space method. It allows for flexible consideration of perturbed flight paths, resulting in shadows, layovers etc. It actually models the imaging process.

Benefits from this flexibility accrue, for example in the SIR-A case:

SIR-A was not designed to deliver stereo image pairs. Images taken over the same area are with the same look angle (app.  $50^\circ$  at mid swath) but with crossing flight tracks. This proved to be valid stereo imagery (see chapter 2). This type of imaging can be studied with a simulation method that offers the flexibility of arbitrary flight directions.

The actually implemented technique was also required to allow for investigations regarding squint angle arrangements.

One therefore has now available a method of simulation that can use:

- available flight recordings,
- arbitrary resolution and size of DEM,
- arbitrary resolution and size of simulated image,
- squint angle imaging,
- range processing (ground resp. slant range geometry),
- choice of elevation angle (or sweep-delay),
- choice of look direction of SLR,
- uniform backscatter curves according to EO. 3.14 (b).

In addition there exist a simple method that is faster and applicable where special parameters need not be studied.

The product of the software implementation is named SIMRISA (SIMulation of Radar images using an Image Space Algorithm) and described in appendix A. Emphasis was put on modularity of the system. The program can be easily changed, e.g. additional thematic input data sets could allow for use of different backscatter curves or use of different look-up tables within one DEM area.



## 4. Verification of the Simulation Program

### 4.1. Using Geometric Shapes

Synthetic DEM's serve to demonstrate the features of the simulation system. Figures 4.1 (a), (b) show one of these synthetic models. The two profile lines appear again in Fig. 4.2, where the slant range geometry for these special cases is explained.

The illumination (or problem of hidden surfaces) is presented in Fig. 4.3. Here as well as in the following radar images of this model the ground level is not illuminated (or imaged) but set to a constant value to enhance the shadows and geometric features of the image.

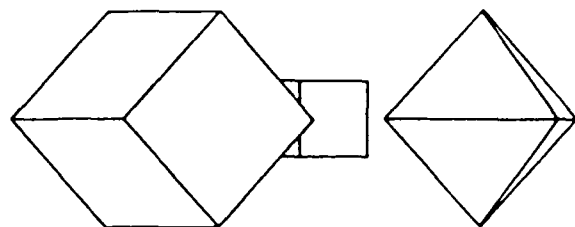
The flight path is chosen to show distinct lay-overs and shadows.

Fig. 4.4 presents a synthetic slant range presentation of the data.

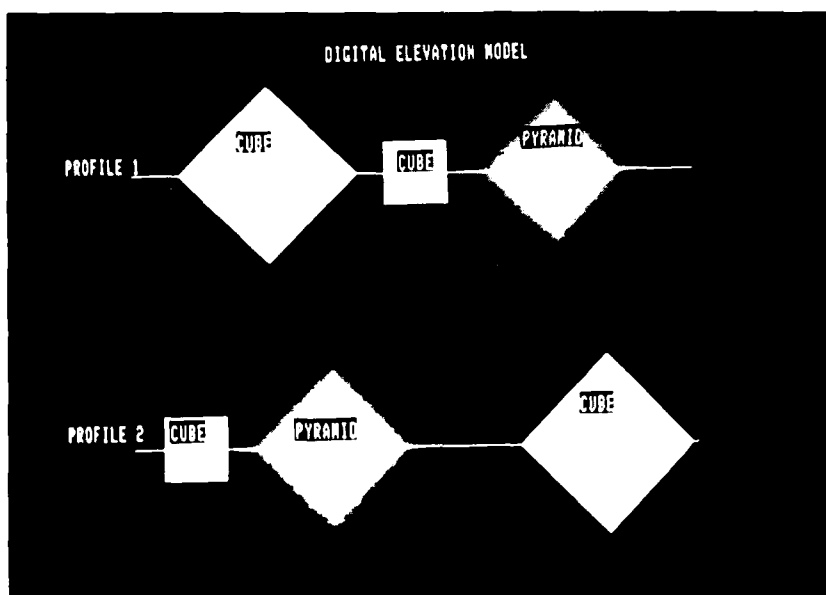
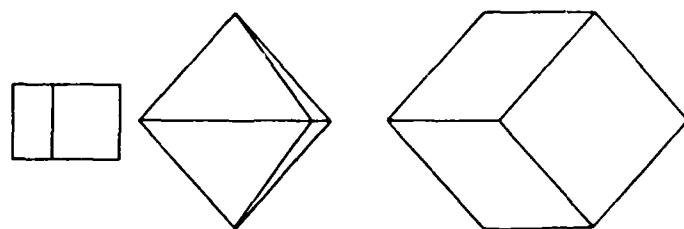
An assumption of diffuse scattering is made. With varying incidence angles on a flat ground from near range to far range the grey values change, too, from high values to low ones. The geometric shapes change in both their image geometry as well as their brightness. Very high return values indicate layovers (more than one return value arrives at the receiver at the same time). Grey value 0 indicates radar shadow. Not only the geometry but also brightness of an object changes as it is imaged at different look angles. This is a main cause of difficulties in stereo radar.

Fig. 4.5 (a) and (b) present an opposite side stereo pair. Here the parameters were chosen like they might be with the ERS-1, at a flight altitude of 777 km and an incidence angle of  $23^{\circ}$  at the center of the (80 km wide) swath. However, stereo viewability is not possible for this specific terrain and sensor configuration. (The configuration is presented in Fig. 4.6)

The data set can serve for educational purposes since it allows one to follow through a series of parameters with the same known shapes.



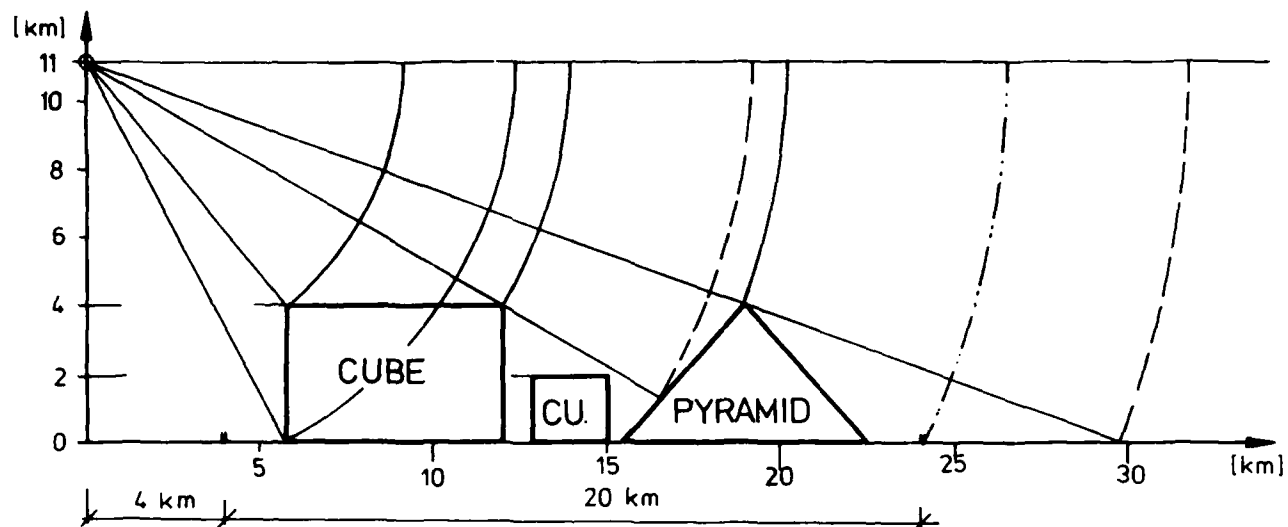
(a)



(b)

Figure 4.1: Synthetic Height Model.

PROFILE 1:  
M 1: 200 000



PROFILE 2:

M 1: 200 000

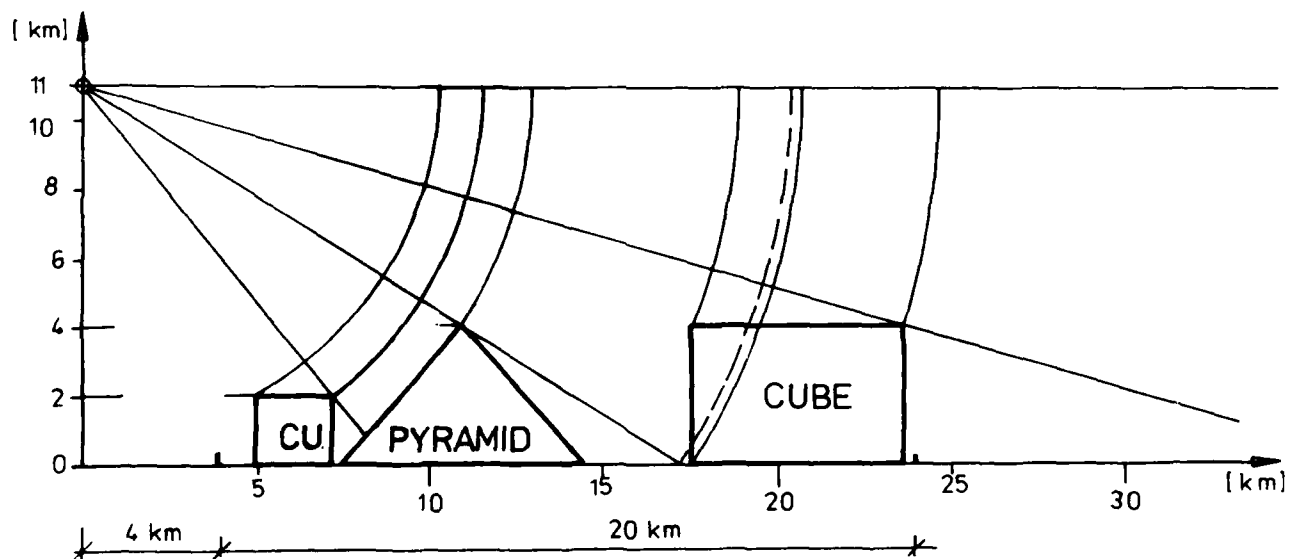


Figure 4.2: Imaging geometry for slant range presentation corresponding to the profiles in Figure 4.1 (b).

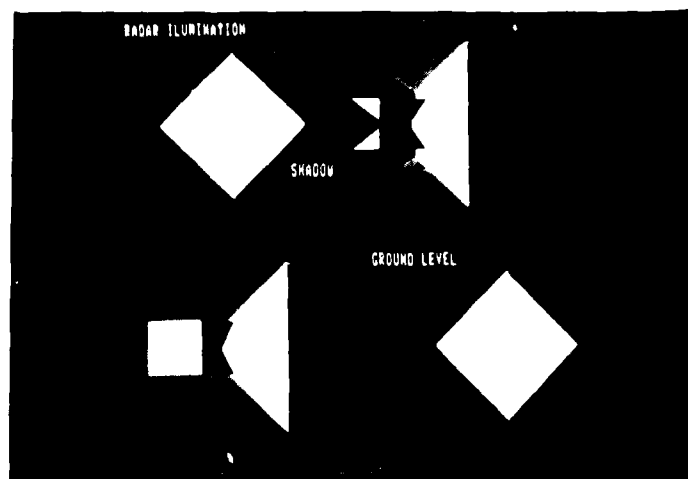


Figure 4.3: Radar illuminated height model  
(shadow and illuminated areas  
can be clearly separated).

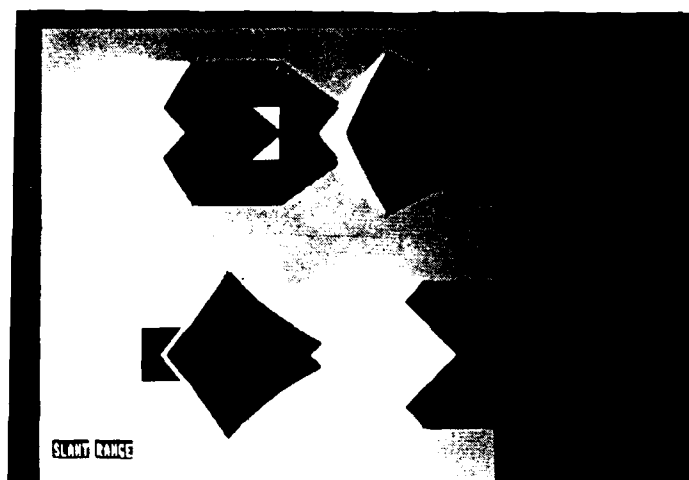


Figure 4.4: Radar slant range presentation.

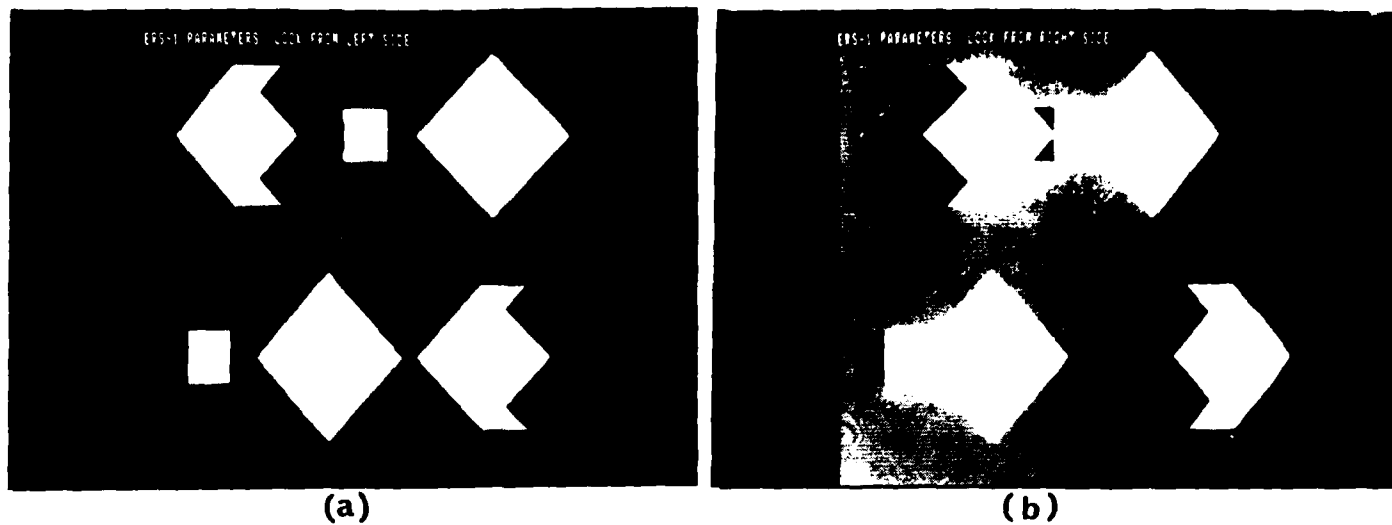


Figure 4.5: (a), (b) Opposite side stereo pair.

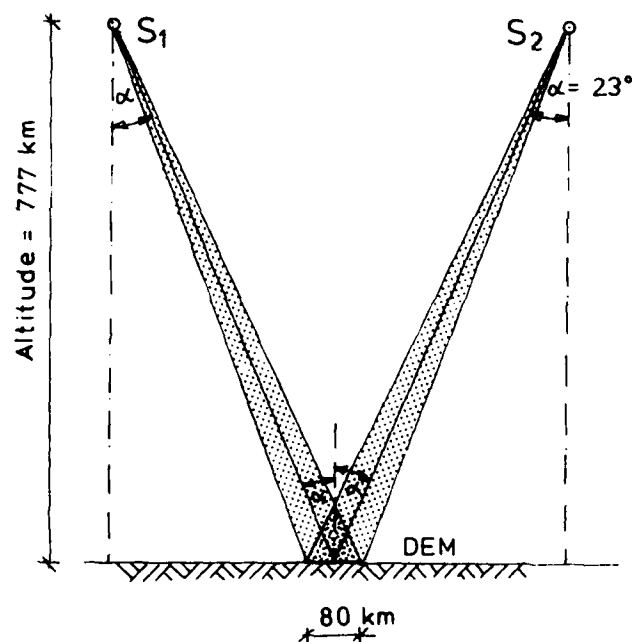


Figure 4.6: Sensor configuration for 4.5.

## 4.2 Using SIR-A Data

The Shuttle Imaging Radar A experiment was carried out in November 81. The swath width was approximately 50 km, with an incidence angle of  $50^\circ$  at mid-center. The wavelength was 23 cm (L-band).

### (a) Greek Islands

A well-suited data set for radar stereo studies was generated during the SIR-A mission over two of the Ionian islands, Cephalonia and Ithaka. The islands are situated between  $38^\circ 00'$  N and  $38^\circ 30'$  N latitude and between  $20^\circ 19'$  E and  $20^\circ 49'$  E longitude.

For stereo studies a DEM had to be generated. This was done using a topographic map at scale 1:200 000 in an UTM projection with contour-lines at a 200 m interval. The contour-lines were digitized into a grid with a mesh size of 1" in latitude and longitude.

Cephalonia is the largest (743 sqkm) island of the Ionian group and also the most mountainous one. The highest elevation - mountain Aenos covered with firs and stone-pines - is 1628 m. Population is mainly on the shores, like the capital Argostolion (7100 inh.), Lixuri (3400 inh.) or Sami (1000 inh.). The vegetation is rich and nearly tropical. The economy is based mainly on vineyards and olivetrees.

Ithaka - native island of Odysseus - is rocky and not very fertile. It is divided into two mountainous areas connected by a land-bridge only 600 m wide. The highest elevation is mountain Nitros (806 m) in the northern part. Ithaki is the main city (2300 inh.)

During the SIR-A flight Cephalonia and Ithaca were imaged two times: on Data Take 32-33 and Data Take 37A. The two orbits crossed at an angle of approximately  $34^\circ$  and created two images sufficient to produce observable stereo parallax. The stereo pair was shown in Fig. 2.13. The swath width is 50 km, look angle  $47^\circ$ . SIR-A was optically processed.

The radar images show all main cities in Cephalonia by their bright return values: Argostolion, Lixuri, Sami and Karavomilo from the map in Fig. 4.7 can be identified on the images. The mountainous region in the central part of Cephalonia (forested region) is a quite homogeneous, diffuse scatterer and shows the brightness depending on the incidence angle. The runway of the airport south-west of Argostolion is a specular scatterer and returns no echo to

the sensor at an incidence angle of approximately  $45^\circ$ .

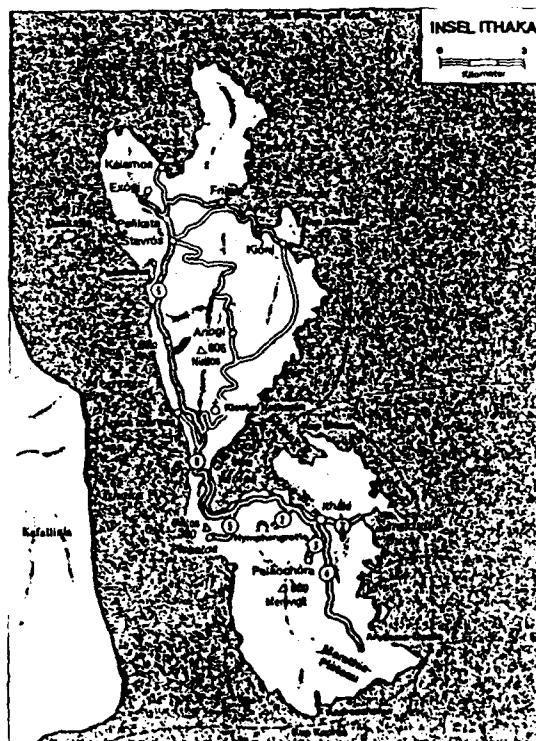
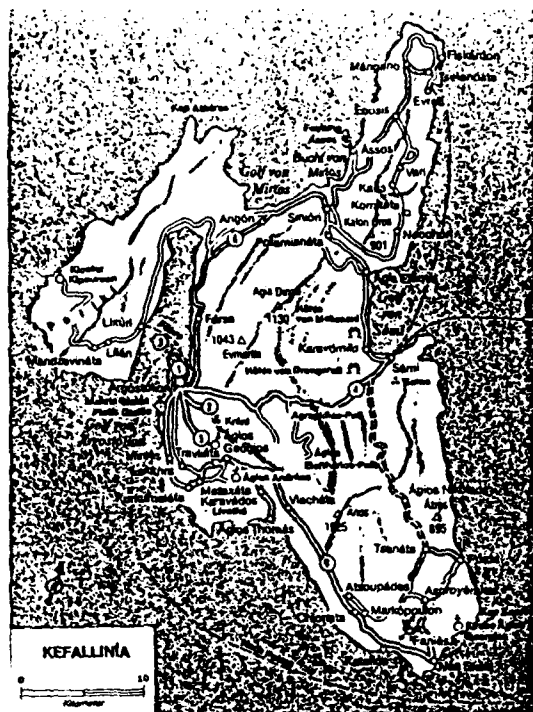


Figure 4.7: Map of Cephalonia (a) and Ithaka (b).

The simulations of Fig. 4.8 are based on a homogeneous backscatter curve for the whole test area. The diffuse scattering of the forested central part can be modeled by the Hagfors law. Comparison of the real and simulated image in the flat western peninsula shows the limitation of the simulation if no thematic information is used. Also the DEM has accuracy limitations so that smaller features are lost in the simulation.

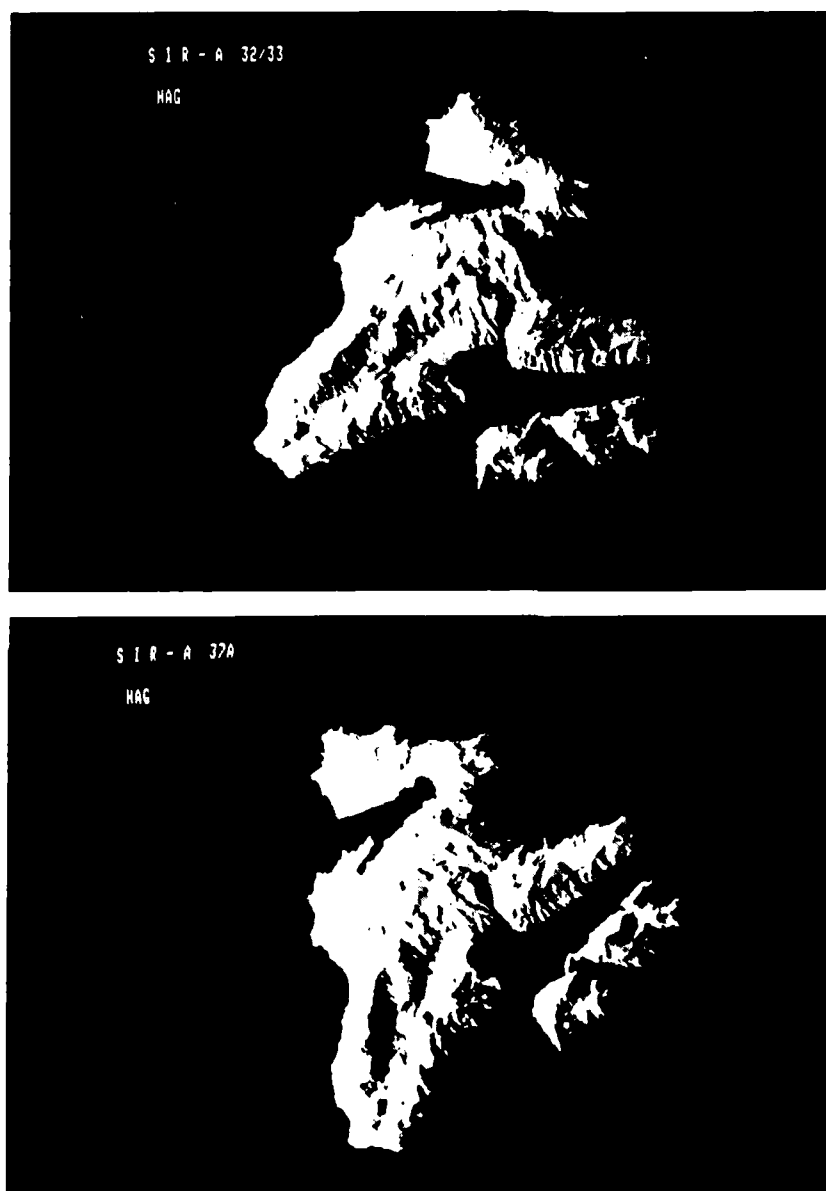


Figure 4.8 : Simulations of Greek Islands, using SIR-A Parameters. (Cimino/Elachi, 1982)



(b) Northern California

Another test site was found in North California (latitude:  $40^{\circ}$  -  $41^{\circ}$  N, longitude:  $123^{\circ}$  -  $121^{\circ}$  E). The elevation model was obtained from the U.S. Geological Survey. It is in the U.T.M. projection and is obtained from contour-lines on a 1:250000 topographic map.

To achieve a resolution comparable to the existing radar image the DEM was reduced - each 4 height points of a grid cell were averaged into one value, resulting in a DEM cell diameter of 126 m. Using a display screen showing 512x512 pixels this test site represents a square area with approximately 64.5 km on each side.

The corresponding real radar image was obtained by SIR-A, orbit 21, data take 24B. The resolution of the image was roughly 40 m; originally SIR-A images were analog; the test data were digitized with a pixel diameter of about 25 m. To cover a comparatively larger area in a 512x512 pixel array, each 25 image points were averaged into one to obtain about the same pixel resolution as for the simulated image.

The topo data file was preprocessed for the earth curvature and rotated to be parallel to the direction of the Space Shuttle. This way the simplified version was used for simulation. Ultimately a slant range presentation was obtained.

Real and simulated images of the test area appear in Fig.'s 4.9 (a) and (b); a backscatter function after Hagfors (see 3.2) served in the simulation. The results appear to be sufficiently realistic to serve in stereo viewability experiments.

---

Work for the simulation of the North California test site was done while one of the cooperators, G. Domik, was a visiting research affiliate at the Jet Propulsion Laboratory, Pasadena, California. Dr. M. Kobrick was the supervisor during the visit. His support is gratefully acknowledged.

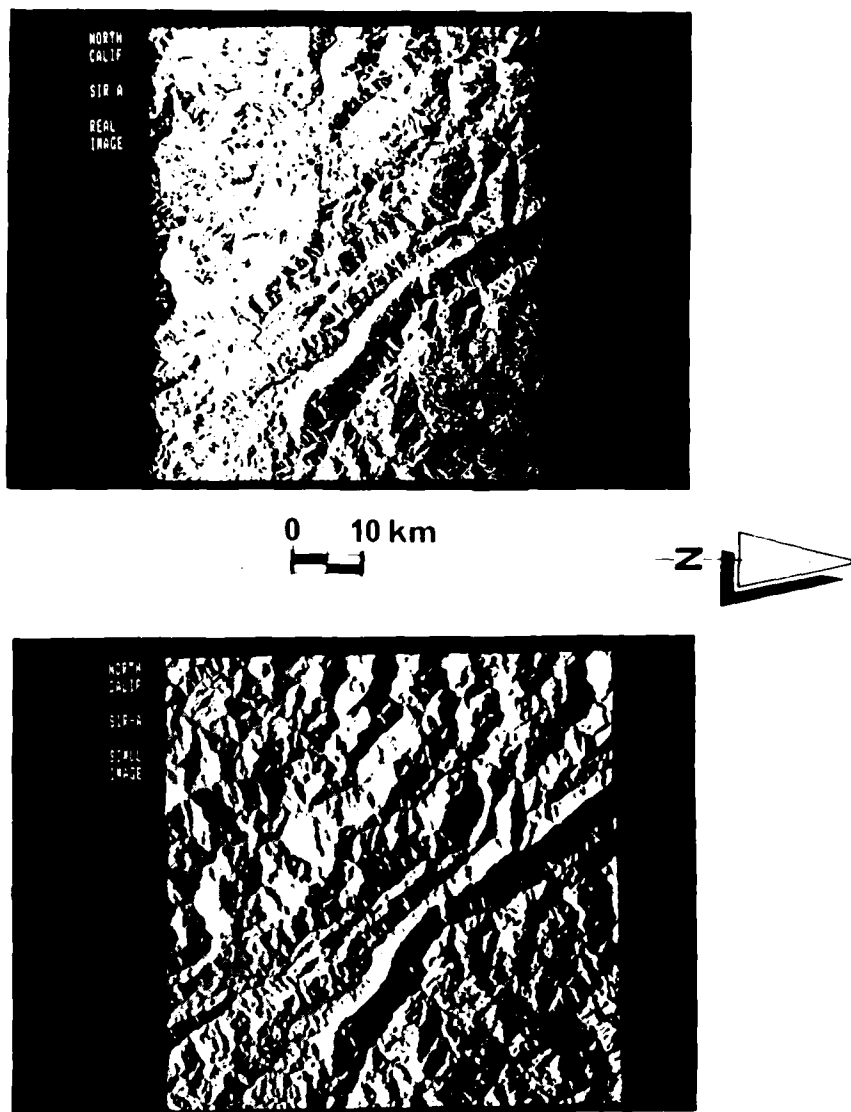


Figure 4.9 : Real and simulated image from N-California  
 (a) SIR A : Orbit 21 / Data Take 24 B.  
 (b) Simulation using SIR-A Parameters.

Just west of the presented area lies the center of another swath crossing, producing a cross angle stereo pair (crossing angle  $14^{\circ}$ ). Both the real and the simulated image are presented in (Kobrick et al, 1983).

#### 4.3 Using SAR-580 (Oetztal).

The SAR-580 Experiment 55-0 "Snow and Ice Parameters from Radar Data" was associated with a glacierized region in the Austrian Alps (Rott H., 1983). The main objectives were directed at applications of SAR data for mapping of snow and glaciers in mountain regions.

On July 7, 1981, one pass (no.149) was acquired in X- and C-Band (both HH-Polarisation), covering a ground swath of 13 km length. Fig. 4.10 shows a sketch map of the ground swath covered by the digitally processed SAR data; it is centered at about  $46.8^{\circ}$  N and  $10.9^{\circ}$  E. The testsite covers an altitude range between 2000 m and 3500 m a.m.s.l.

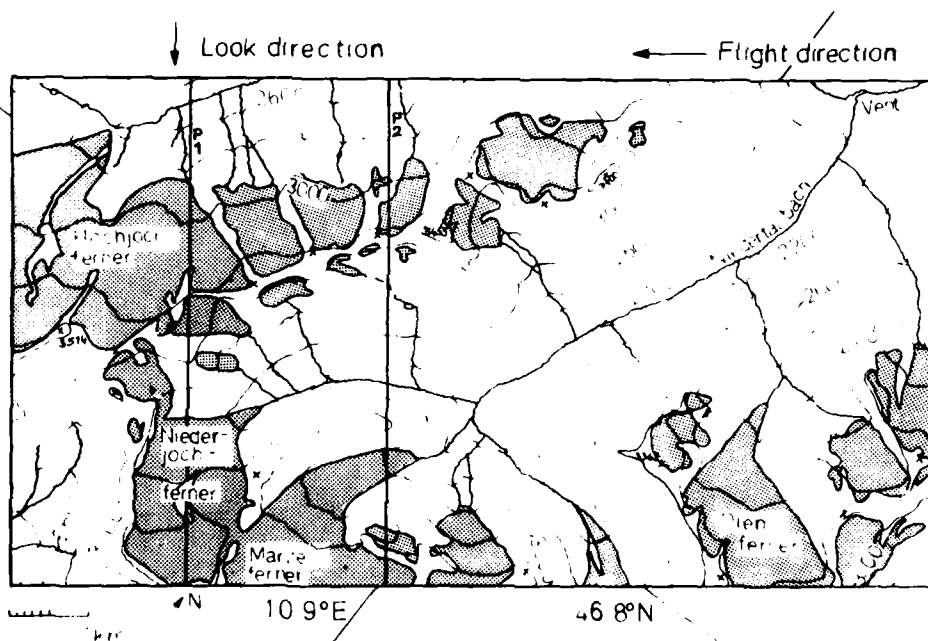


Figure 4.10 : Sketch map of the SAR-580 test site 0-1, Oetztal, Austria. Glaciers are dotted.

Fig.'s 4.11 show different presentations of an area which includes the imaged part.

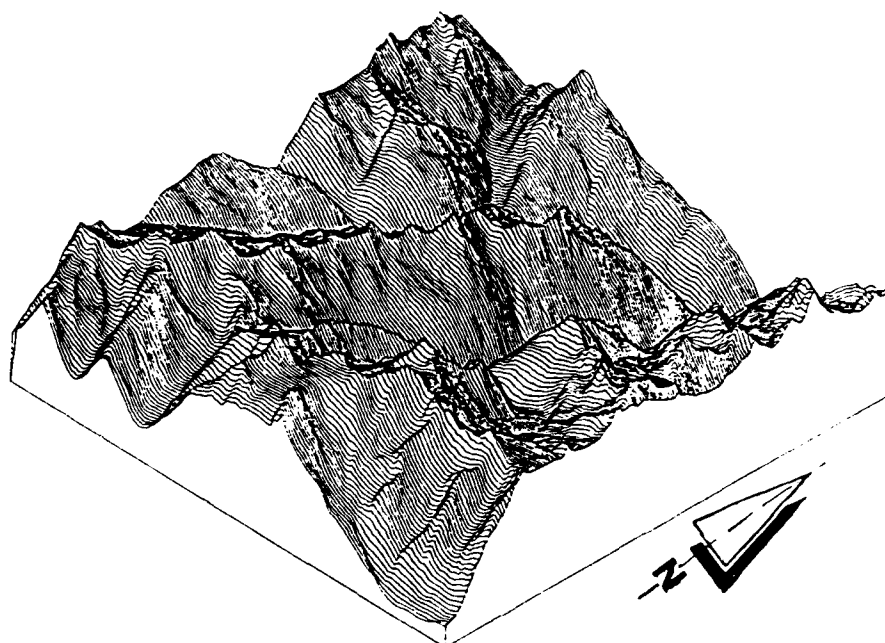


Figure 4.11 : Digital elevation model of Oetzthal. The actual radar image is only part of the data displayed above.  
 above: axonometric presentation of height model.  
 below: Illuminated height model.

In Fig. 4.12 the imaging parameters of the profiles in Fig. 4.10 are explained. Simulation was carried out using these parameters. Also the corrections from a slant range dependence to a ground range presentation for a flight altitude of 6100 m a.m.s.l to a nominal altitude of 2500 m a.m.s.l carried out during processing. Comparisons of the real and simulated image in Fig. 4.13 (a) and (b) show the same geometry. The radiometry is not matched to the real one since this would lead beyond the scope of the current research.

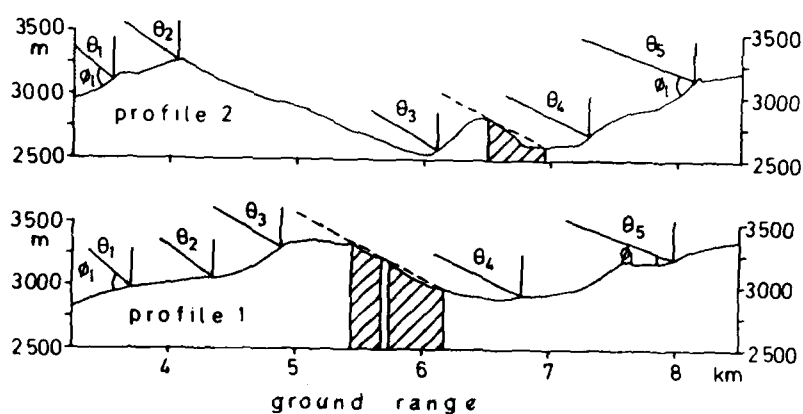


Figure 4.12: Surface relief at the profiles 1 and 2 of the test site 0-1 with radar imaging geometry. Zones of radar glaciers are hatched.  $\theta_1 = 50^\circ$ ,  $\theta_2 = 55^\circ$ ,  $\theta_3 = 60^\circ$ ,  $\theta_4 = 65^\circ$ ,  $\theta_5 = 70^\circ$  antenna incidence angle.

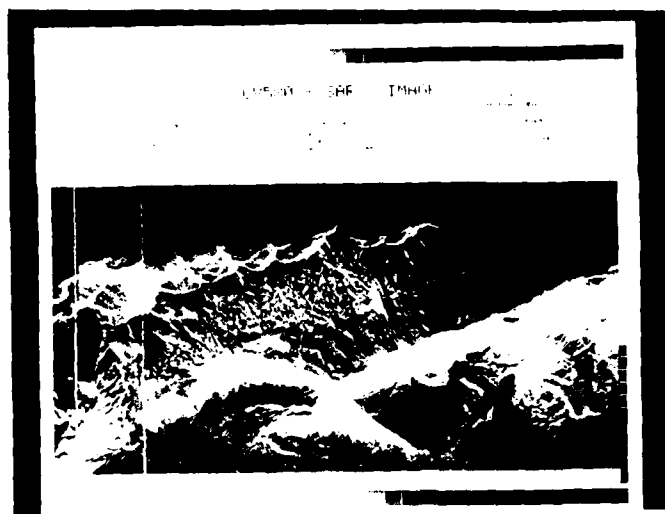


Figure 4.13: Radar image of Oetztlal (around range)  
 (a) SAR-580 image.  
 (b) Simulation.

## 5. Discussion of Stereo-Viewability

Evaluation results of stereo-viewability are discussed showing tables for "same side", "same side with applied squint angle" and "cross-angle" stereo. Different investigators were requested to rate the viewability: Persons without previous stereoscopic viewing and measuring experiences, and two photogrammetrists with such experience. The viewability is

- described by a number between 1 and 10 by the first group, where 1 denotes "no viewability" and 10 "excellent viewability". There is also a distinction between 1-4 and 5-10, the lower numbers indicating "not acceptable" and the higher ones "acceptable" stereo.

- described by a letter g, m or n (by the photogrammetrists), where g means "good visible", m means "marginal" and n means "not visible".

This second grading shows stereoscopic impression to a much higher extend.

The model area for these tests was the Greek Island test site, which can be characterized as a "high relief area". The site is described in more detail in 4.2 (a). According to the stereo viewing considerations (chapter 2.2 (b)), the two stereo partners should be similar in thematic content. Thus a homogeneous backscatter curve was used, homogeneous in the sense of not differentiating between thematics in the image as well as in the sense of using the same backscatter curve for a whole set of stereo images to be evaluated.

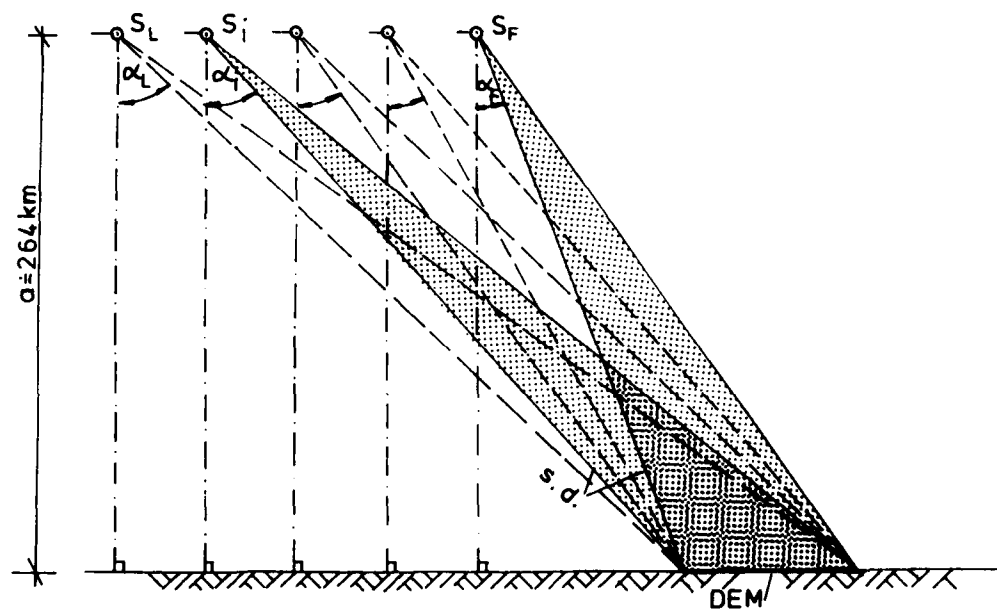
### 5.1. Same Side Stereo -- Different Elevation Angles

Table 5.1 shows the quality of the viewability of same side stereo for twelve simulated images (all in slant range presentation). Their elevation angles, also denoted as "look angles", range from  $10^{\circ}$  to  $80^{\circ}$  (See Fig. 5.1 for stereo configurations and Fig. 5.2 for examples). Stereo viewing for the northern part of the island (heights less than 1000 m) is possible for a much wider range of intersection angles than viewing the southern part of Cephalonia, where the area is very rough and higher and thus creates more shadow for shallow look angles and more foreshortening and layover for steep look angles.

The highest ranked stereo pairs (evaluated 9-10/q) are closer investigated (table 5.2). An intersection angle between  $10^{\circ}$  and  $25^{\circ}$  was found to be best.

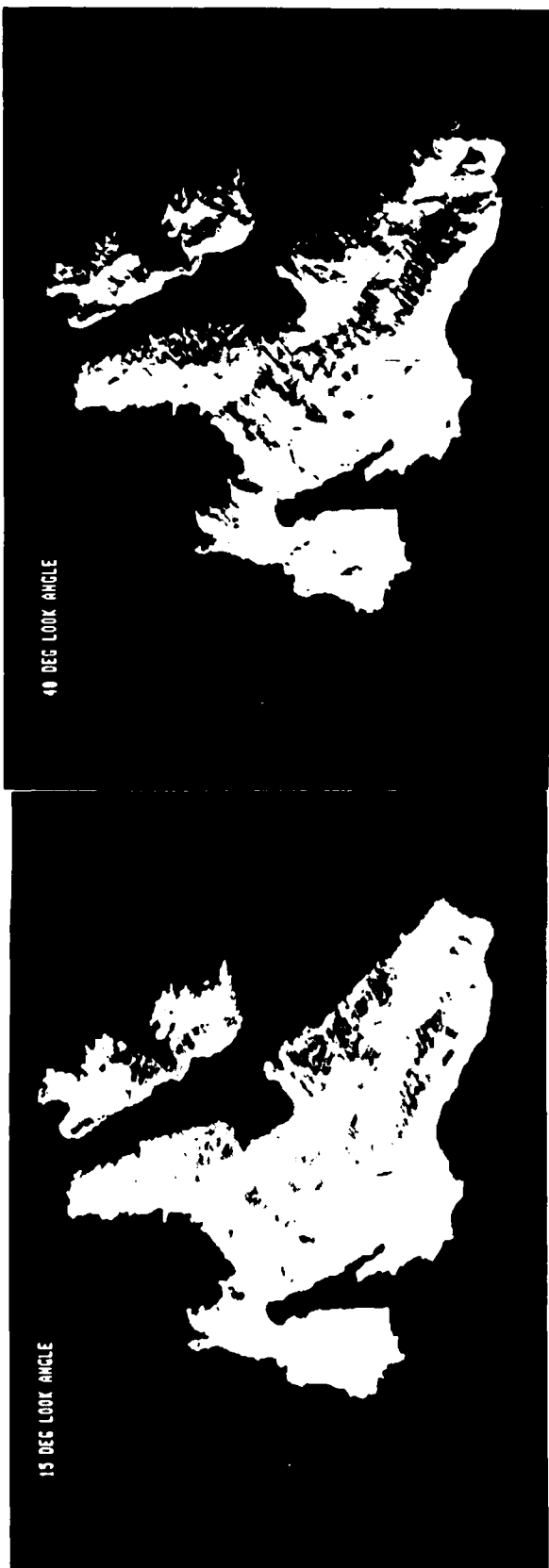
The photogrammetrists found  $60^{\circ}$  intersection angles still to be viewable. The back-slopes, however, were judged to be more difficult to fuse than slopes facing towards the antenna.





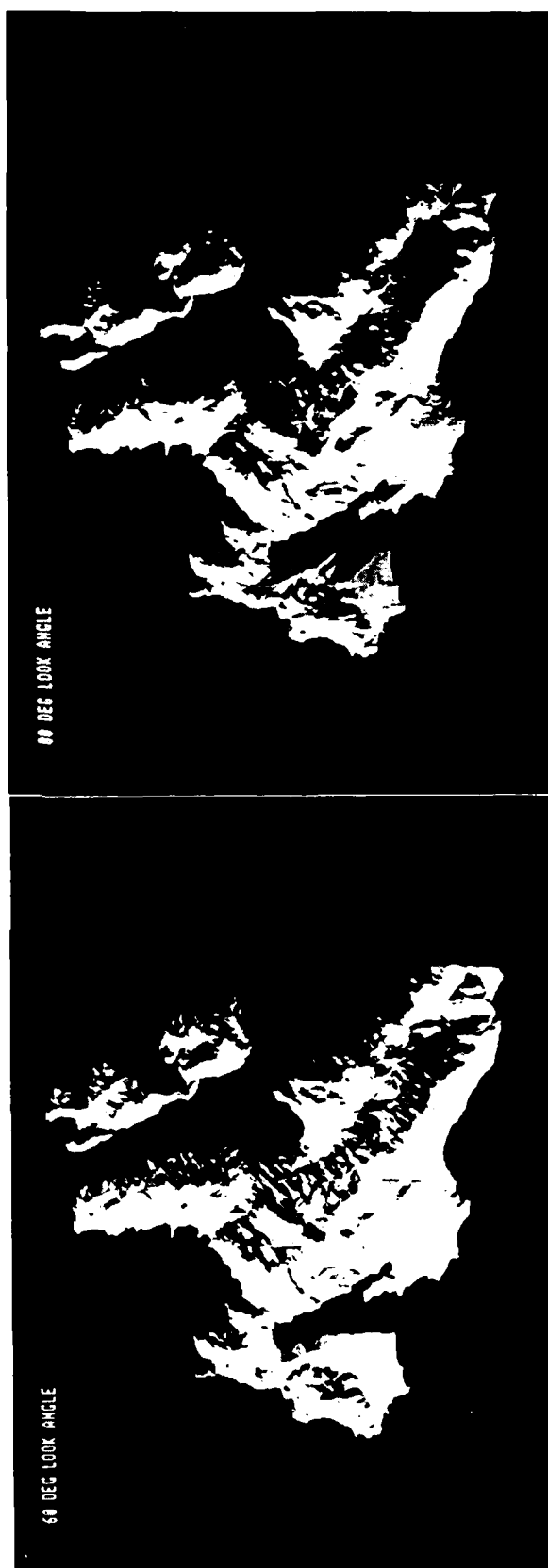
DEM . . . . Digital Elevation Model  
 $S_F$  . . . . Satellite at first flight  
 $S_L$  . . . . Satellite at last flight  
 $a$  . . . . Altitude  
 $s.d.$  . . . . Sweep Delay  
 $\alpha$  . . . . Elevation Angle  
 $\alpha_F$  . . . .  $10^\circ$   
 $\alpha_L$  . . . .  $80^\circ$

Figure 5.1: Configurations of same side stereo.



a

b



c

d



Figure 5.2: (a) - (d)  
Examples of simulated radar images  
with different elevation angles  
(denoted as look angles)

Same Side Stereo

Look Angle	10°	15°	20°	30°	40°	47°	50°	60°	65°	70°	75°	80°
10°												
15°	6/g											
20°	5/g	7/g										
30°	3/g	8/g	8/g									
40°	1.5/m	5/g	7/g	9/g								
47°	1/n	2/g	6/g	9/g	8/g							
50°	1/n	1/g	5/g	8/g	9/g	4/g						
60°	1/n	1/n	4/g	7/g	9.5/g	7/g	7.5/g					
65°	1/n	1/n	2/g	6/g	8/g	8/g	9/g	6/g				
70°	1/n	1/n	1.5/g	5/g	8/g	9/g	10/g	7/g	7/g			
75°	1/n	1/n	1/g	3/g	8/g	7.5/g	9.5/g	8/g	8/g	7/g		
80°	1/n	1/n	1/m	2/m-g	4/g	5/g	5.5/g	5/g	4/g	4/g	5/g	

Table 5.1: Same side stereo evaluation.

RANK ORDER	ELEVATION ANGLES	INTERSECTION ANGLE
1	$70^{\circ} / 50^{\circ}$	$20^{\circ}$
2	$60^{\circ} / 40^{\circ}$	$20^{\circ}$
2	$75^{\circ} / 50^{\circ}$	$25^{\circ}$
3	$40^{\circ} / 30^{\circ}$	$10^{\circ}$
3	$47^{\circ} / 30^{\circ}$	$17^{\circ}$
3	$50^{\circ} / 40^{\circ}$	$10^{\circ}$
3	$70^{\circ} / 47^{\circ}$	$23^{\circ}$
3	$65^{\circ} / 50^{\circ}$	$15^{\circ}$

Table 5.2: Ranking of best same side stereo images.

## 5.2. Distortions of Same Side Stereo with Applied Squint Angles

The interpreters graded the stereo pair with  $50^\circ$  and  $70^\circ$  elevation angles as best. Using the same input parameters for the simulator, the squint angle was varied between  $0.5^\circ$  and  $50^\circ$ . The images obtained were geometrically restored to images without squint. Examples are given in Fig. 5.3 (a)-(d).

The radiometric distortions proved to be "not acceptable" by applying a squint of more than or equal to  $30^\circ$ . Again, the stereoscopic impression is possible much longer in the northern and flatter part. The radiometric differences (illumination, shadow) are much higher in the southern part.

A summary of the quality vs. squint angles is shown in table 5.3.

The front slopes were more easily fused than the back slopes where shadow effects add a confusion element in the viewing process. Also the limitation of the simulation model which did not take the image resolution properly into account, (described in more detail in Appendix A), may bias the conclusion in favor of larger squint angles to be acceptable. Thus sharp edges and plateaus were present and preserved in the simulation.



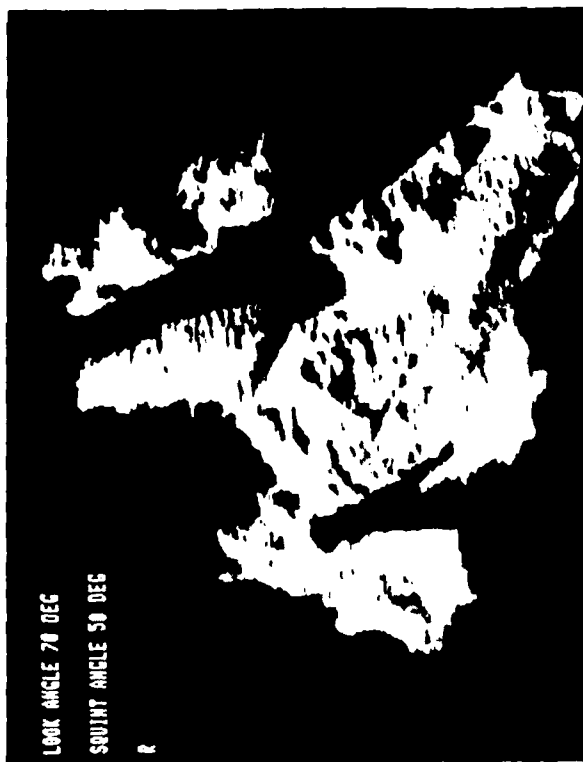
a



b



c



d

Figure 5.3: (a) - (d)  
Examples of simulated radar images  
with different squint angles but

# Squint Distortions

70° \ 50°	0°	0.5°	1°	5°	10°	30°
	0°	0.5°	1°	5°	10°	30°
0°	10/g					
0.5°	9/g	10/g				
1°	8/g	9/g	10/g			
5°	8/g	8/g	9/g	8/g		
10°	7/g	7/g	7/g	7/g	7/g	
30°	4/m	4/m	4/m	4/m	4.5/m	4/m
40°	1/n	1/n	1/n	1.5/n	2/n	1/n
50°	1/n	1/n	1/n	1/n	1/n	1/n

Table 5.3: Evaluation of squint angle images.

### 5.3. Crossing Flight Tracks -- Same Elevation Angle

In the Greek Island SIR-A picture imaging with two tracks crossing at an angle of  $34^\circ$  created a good stereo pair (grade "7"). Further simulations showed a limit to successful viewing between  $40^\circ$  and  $50^\circ$  of the crossing angle. This range of crossing angles was investigated (Fig. 5.4 and 5.5) more closely:

Successful stereo viewing was still obtained from crossing tracks of  $40^\circ$  (grade "5"), but graded "1" for a crossing angle of  $50^\circ$ . The limit lies between  $40^\circ$  and  $42^\circ$ , as can be observed from table 5.4. Trying to detect the limit even more precisely was found to be dependent on the individual investigator.

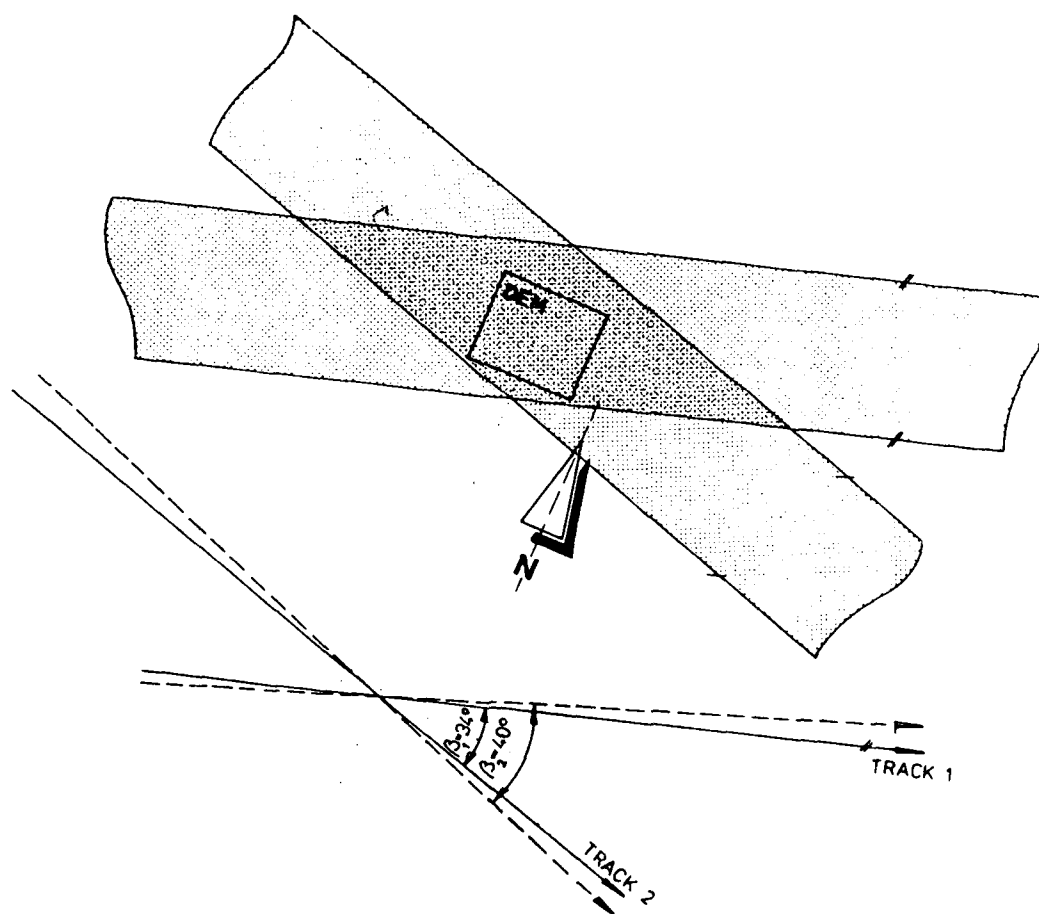


Figure 5.4: Flight and swatch configuration of "cross angle" stereo.



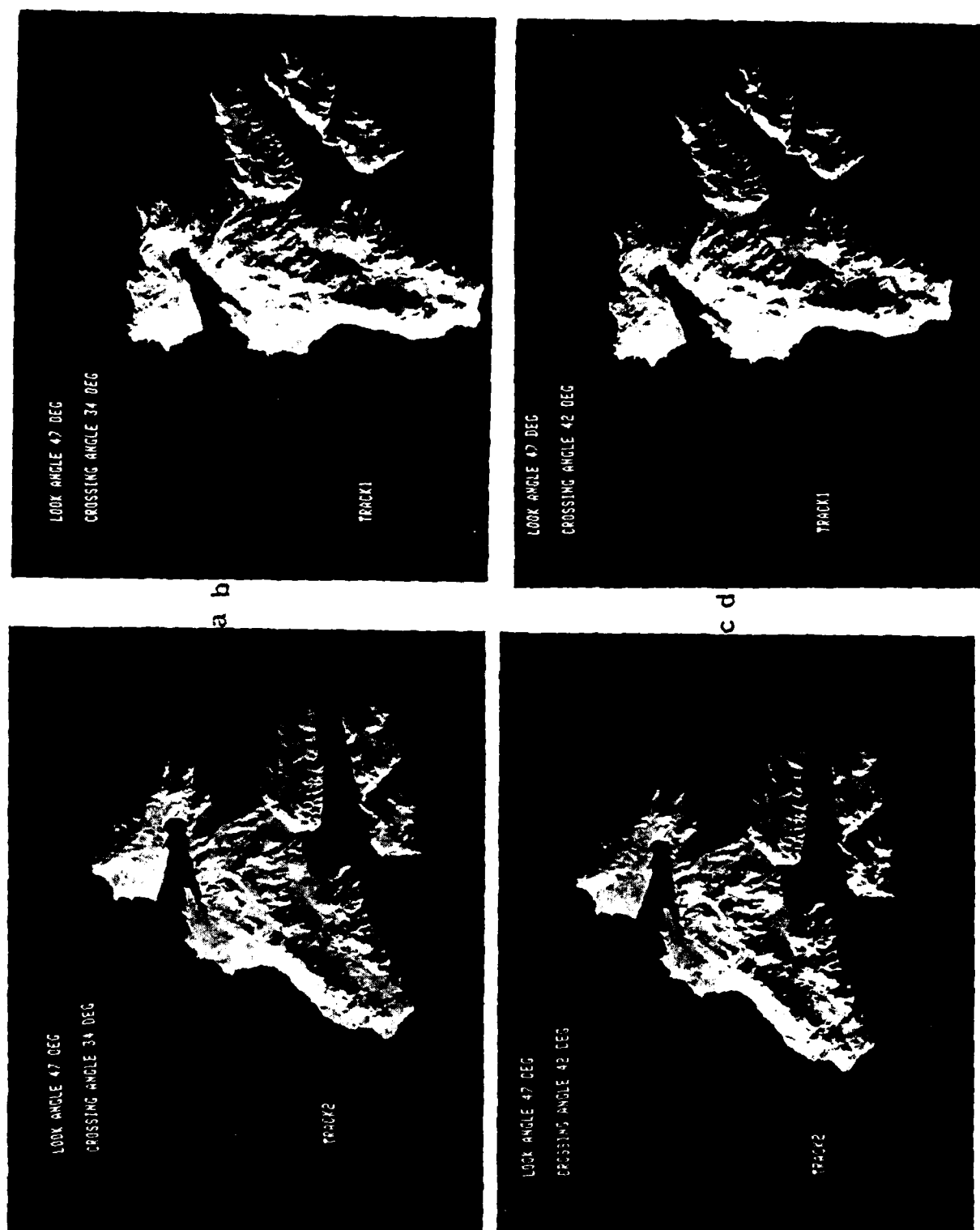


Figure 5.5: (a) - (f)

Examples of simulated radar images  
with crossing flight tracks 1 and 2.  
(a), (b): crossing angle =  $34^\circ$   
(c), (d): crossing angle =  $42^\circ$   
(e), (f): crossing angle =  $50^\circ$

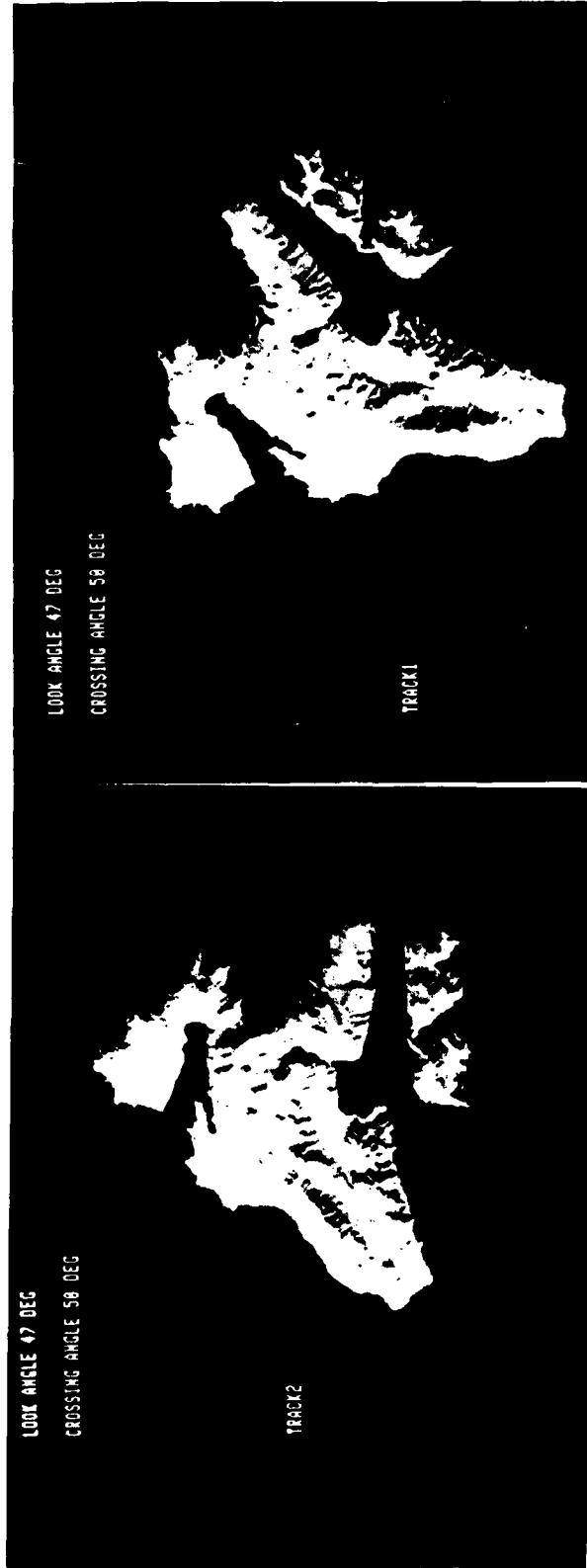


Fig 5.5e

Fig 5.5f

"Cross-Angle" Stereo

Crossing Angle	Evaluation
34°	7
40°	5
42°	4
45°	4
50°	1

Table 5.4: "Cross-Angle" Stereo Evaluation.

## 6. On the Accuracy of Radar Stereo Mapping

The theoretical error propagation into radar stereo model coordinates has been investigated in the part. Also practical studies with actual radar images have resulted in an understanding of achievable accuracies. The following is a short review of recent work to allow one to relate stereo viewability to error propagation and accuracy.

### 6.1. Theoretical Error Analysis of Radar Stereo Models

Error equations for radar stereo models were derived by Leberl (1978, 1979) for a simplified flight arrangement as shown in Figure 6.1. In this local coordinate system the vectors of sensor positions ( $\underline{s}'$  and  $\underline{s}''$ ) and the velocity vectors of the sensor ( $\underline{\dot{s}}'$ ,  $\underline{\dot{s}}''$ ) are given as follows :

$$\begin{aligned}\underline{s}' &= (s_x', s_y', s_z') = (0, 0, H) \\ \underline{\dot{s}}' &= (\dot{s}_x', 0, 0) \\ \underline{s}'' &= (s_x'', s_y'', s_z'') = (0, B, A) \\ \underline{\dot{s}}'' &= (\dot{s}_x'', 0, 0)\end{aligned}$$

EO.'s 6.1

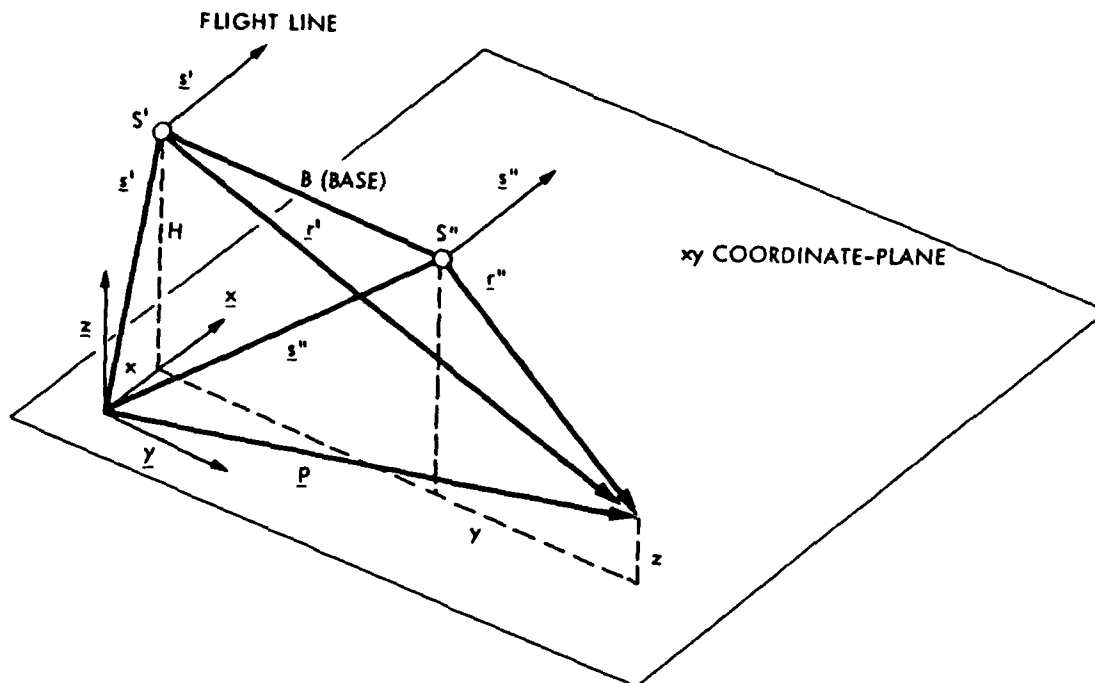


Figure 6.1. Coordinate system

One is dealing with errors in sensor positions ( $\underline{ds}'$ ,  $\underline{ds}''$ ), sensor velocity vectors ( $\underline{ds}'$ ,  $\underline{ds}''$ ) and slant ranges ( $\underline{dr}'$ ,  $\underline{dr}''$ ).

(a) Errors in sensor position coordinates :

It is obvious to see that an error  $ds_x'$  has no effect on  $y$  and  $z$ , so that:

$$\begin{aligned} dx(s_x') &= ds_x'/2 & dx(s_x'') &= ds_x''/2 \\ dy(s_x') &= 0 & dy(s_x'') &= 0 \\ dz(s_x') &= 0 & dz(s_x'') &= 0 \end{aligned}$$

EO.'s 6.2

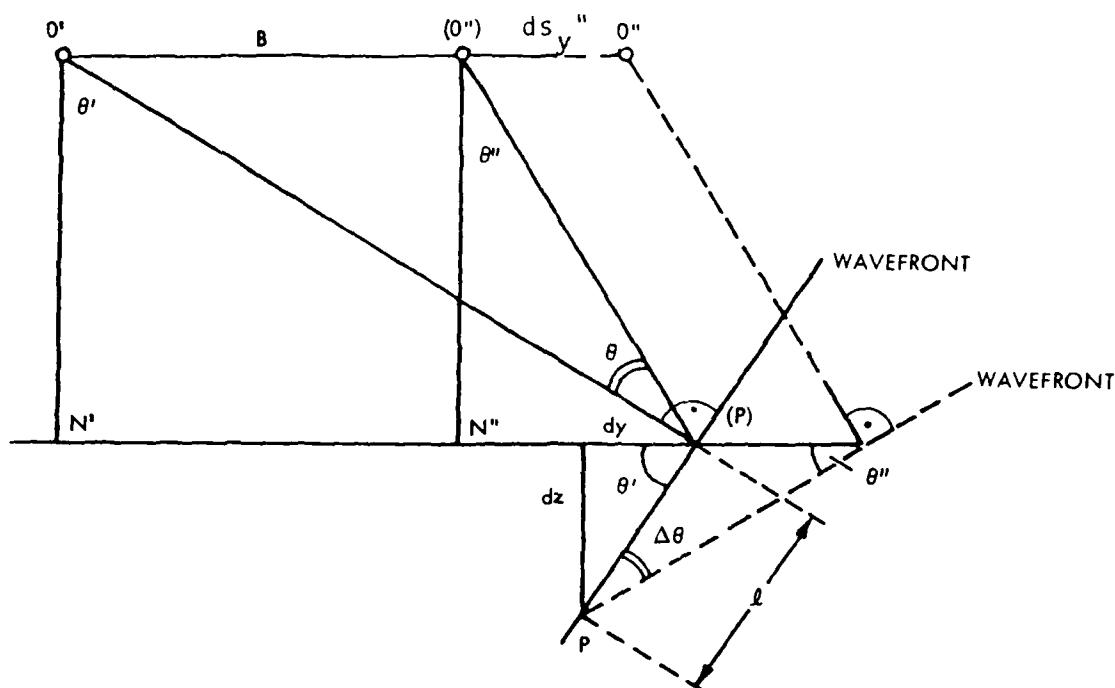


Figure 6.2. Errors due to  $ds_y''$ -component of sensor position

The effects of  $ds_y'$ ,  $ds_y''$  are less obvious. Figure 6.2 clarifies the relationship. There is no effect on x. In y, we find:

$$\frac{dy}{1} = \frac{H}{r'}$$

with

$$\frac{1}{ds_y''} = \frac{\sin \theta''}{\sin (\theta' - \theta'')}$$

So that :

$$dy = H * ds_y'' \sin \theta'' / (r' \sin (\theta' - \theta'')) \quad \text{EQ. 6.3}$$

But :

$$\frac{r'}{B} = \frac{\sin (90^\circ - \theta'')}{\sin (\theta' - \theta'')}$$

$$r' \sin (\theta' - \theta'') = B \sin (90^\circ - \theta'') \quad \text{EQ. 6.4}$$

Introducing EQ. 6.4 in EQ. 6.3 gives :

$$dy = ds_y'' H \tan \theta'' / B$$

so that, finally :

$$dy (s_y'') = ds_y'' (B - y) / B \quad \text{EQ. 6.5}$$

We can substitute for  $y/B$  also :

$$\frac{y}{B} = \frac{y}{r'} * \frac{r'}{B} = \frac{\sin \theta' \sin (90^\circ + \theta'')}{\sin (\theta' - \theta'')} = \frac{1}{1 - \cot \theta' \tan \theta''}$$



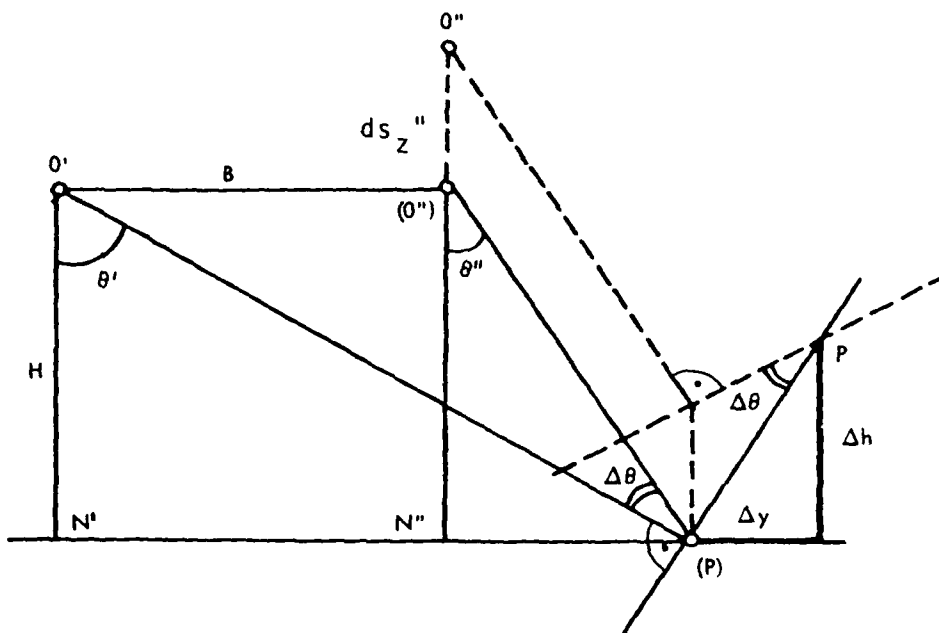


Figure 6.3. Errors due to  $ds_z''$ -component of sensor position

An error of sensor altitude does not deform the model y-dimension, but merely shifts the model in y. In height, there is a linear effect of model tilt.

(b) Errors in sensor attitude vectors :

Erroneous sensor attitudes, caused by errors of the velocity vectors  $\underline{s}'$ ,  $\underline{s}''$ , lead to nonintersecting projection circles. This is illustrated in Figure 6.4, for the example of an error  $ds_y$  which creates an antenna swing  $k$ . We need to define a model point, that most logically is chosen halfway between the error-free point if no  $ds_y$  error had been present.

From Figure 6.4 we find that an error  $ds_y'$  affects the x-coordinates of the model point  $P$ , shifting it to position  $p$ , but leaves the y, z-coordinates unchanged, at least to a first-order approximation :

$$\begin{aligned} dx(s_y') &= ds_y' * y/2 = ds_y' * H * \tan \theta'/2 \\ dv(s_y') &= 0 \\ dz(s_y') &= 0 \end{aligned}$$

$$\begin{aligned} dx(s_y'') &= ds_y'' * (y - B)/2 = \\ &= ds_y'' * H * \tan \theta''/2 \\ dy(s_y'') &= 0 \\ dz(s_y'') &= 0 \end{aligned}$$

EO.'s 6.8

TOP VIEW

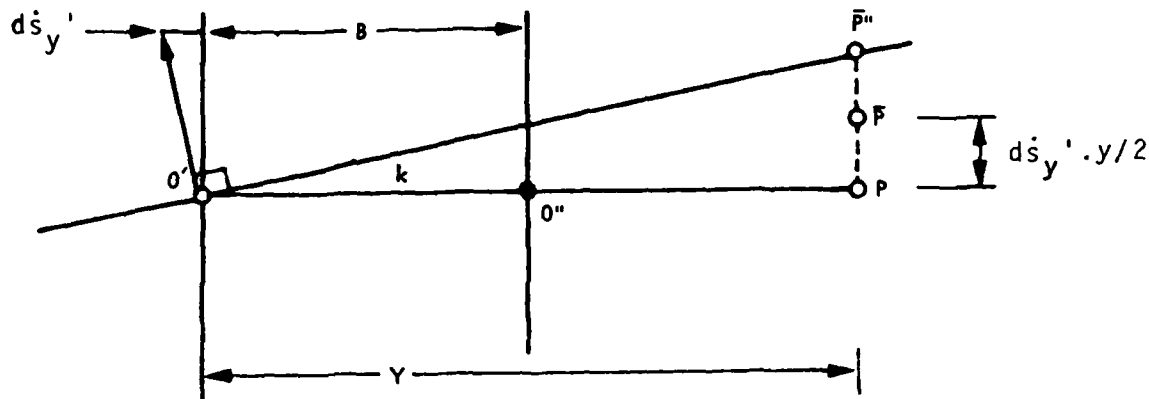


Figure 6.4. Error due to  $ds_y$  - component of velocity vector

Similarly, the  $ds_z'$   $ds_z''$ -components cause a tilt  $\theta$  of the radar antenna, so that:

$$\begin{aligned} dx(s_z') &= ds_z' * H/2 \\ dy(s_z') &= 0 \\ dz(s_z') &= 0 \end{aligned}$$

$$\begin{aligned} dx(s_z'') &= ds_z'' * H/2 \\ dy(s_z'') &= 0 \\ dz(s_z'') &= 0 \end{aligned}$$

EO.'s 6.9

An erroneous  $ds_x'$ ,  $ds_x''$ -component will not affect the antenna attitude and thus not produce errors of the stereo model. It will, of course, affect antenna position when integrated over time. This error was considered in Equation 6.2.



(c) Errors in slant ranges:

A last error of the stereo model results from erroneous range data  $r'$ ,  $r''$ . Figure 6.5 shows that:

$$\begin{aligned} dx(r') &= 0 \\ dy(r') &= dr' * r'/B = dr' (y^2 + H^2)^{1/2}/B = \\ &= dr' * \cos \theta' / \sin (\theta' - \theta'') \\ dz(r') &= dr' * r' * (y - B)/B * H = \\ &= dr' \sin \theta' / \sin (\theta' - \theta'') \\ &= dr' \sin \theta' / \sin (\theta' - \theta'') \end{aligned}$$

$$\begin{aligned} dx(r'') &= 0 \\ dy(r'') &= -dr'' * r''/B = -dr'' \cos \theta'' / \sin (\theta' - \theta'') \\ dz(r'') &= -dr'' * y * r''/B * H = \\ &= -dr'' * \sin \theta'' / \sin (\theta' - \theta'') \end{aligned}$$

EQ.'s 6.10

These errors are nonlinear in the  $y$  and  $z$ -dimensions.

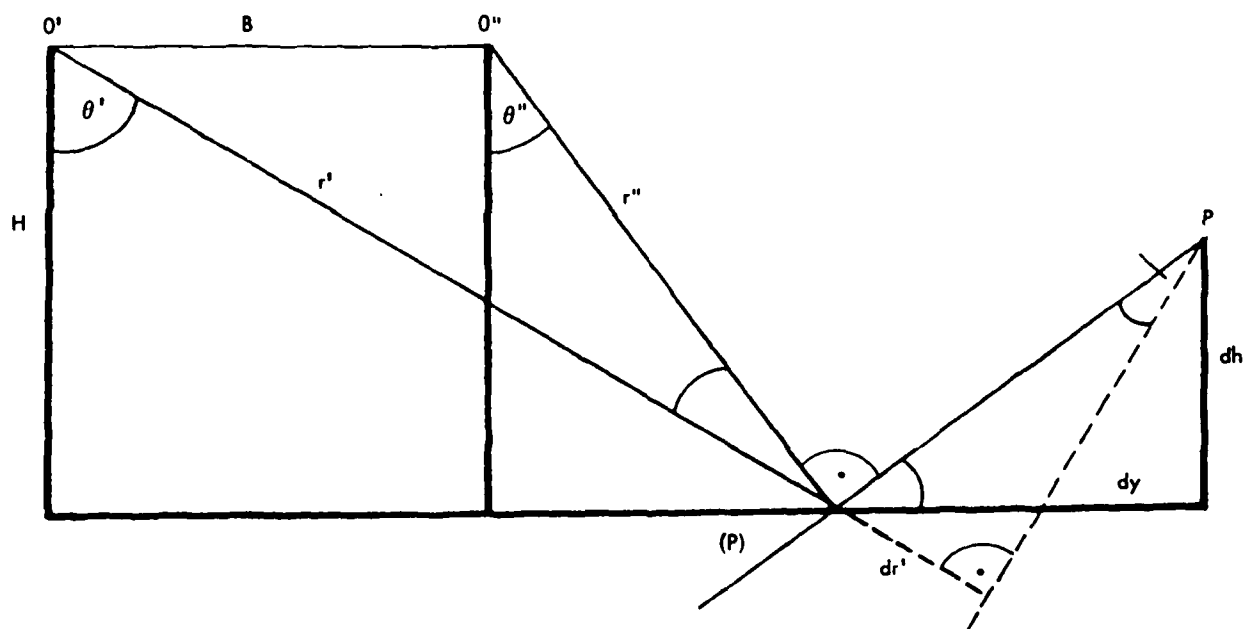


Figure 6.5. Error due to range error

## 6.2 Accuracies with Parallax Measurements

As shown in Chapter 2, parallax difference measurements may serve to compute height differences between terrain points by using the simplified equations (6.11) for ground range presentation or (6.12) for slant range presentation:

$$dh = dp_g / ( \cot \theta'' - \cot \theta' ) \quad \text{EQ. 6.11}$$

$$dh = dp_s / ( \cos \theta'' - \cos \theta' ) \quad \text{EQ. 6.12}$$

The following stereo model cases were used for parallax measurements:

- (a) Aircraft radar image pair of Granite Mountain (Arizona, USA) in ground range presentation. This image pair is shown in Figure 2.4.
- (b) Satellite radar image pair of Granite Mountain in slant range presentation with optical correlation. This image pair is shown in Figure 2.5.
- (c) Satellite radar image pair of Los Angeles, California in slant range presentation and with optical correlation. This image pair is shown in Figure 2.6.
- (c) Satellite radar image pair of Los Angeles, California in slant range presentation and with digital correlation. This image pair is shown in Figure 6.6.

Parallax differences between control points as differences of absolute parallaxes were measured for the four radar stereo models using a stereoscope and a parallax bar and for the two models of Granite Mountain also using a photogrammetric stereoplotter as a comparator. With these parallax differences the height differences between terrain points were determined. The height errors  $dh$  in control points were computed as the difference between known heights  $h$  and radar-derived heights  $h'$ .

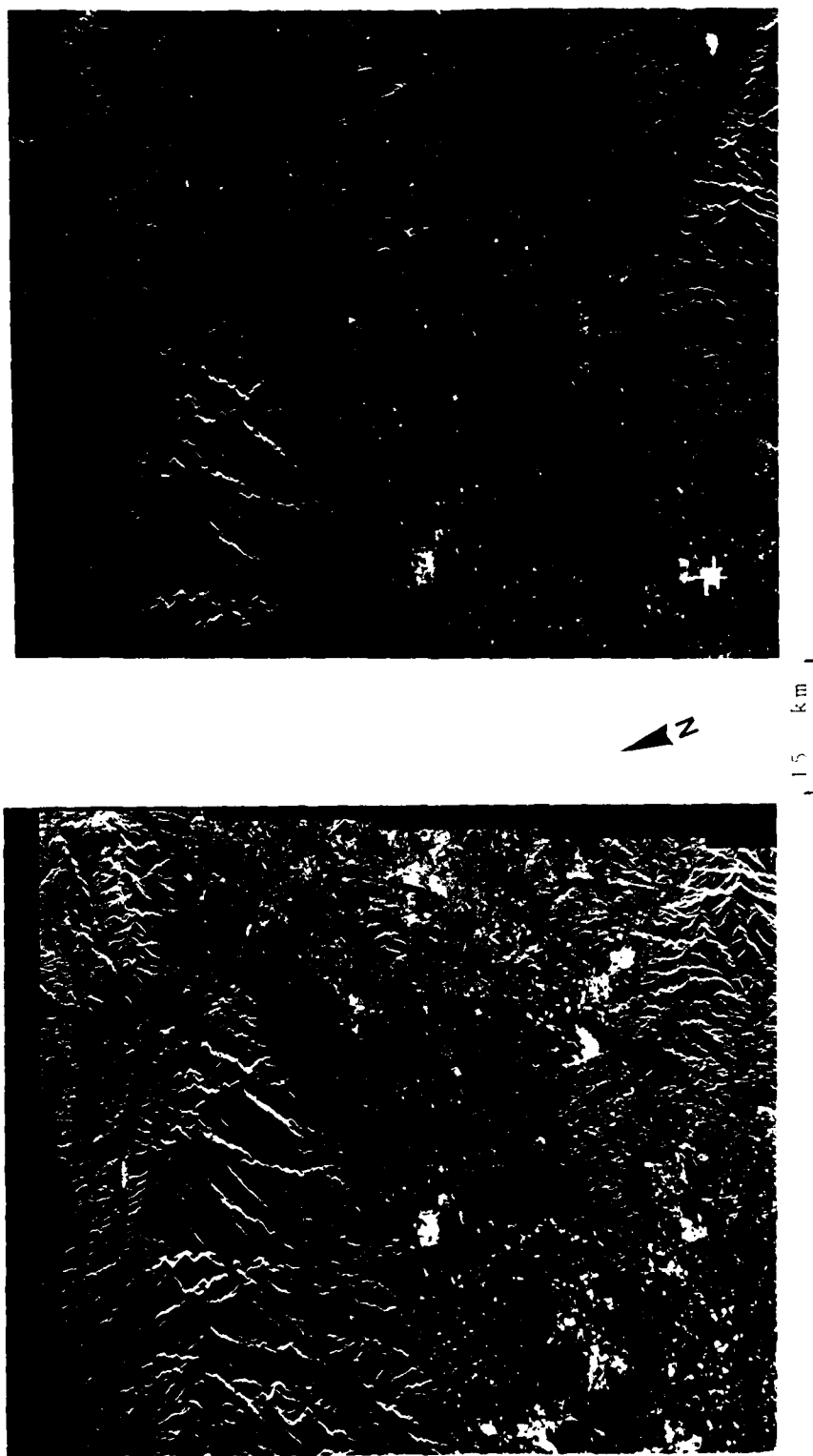


Figure 6.6 Stereo model of Los Angeles, satellite radar,  
with digital correlation

Since there are systematic errors in the radargrammetrically computed heights, a correction polynomial was used to eliminate these errors:

$$h^* = u' + \sum_{i=1}^3 \sum_{j=1}^3 a_{ij} x^{(i-1)} y^{(j-1)}$$

EO. 6.13

One might expect that with the use of a flexible polynomial the systematic height errors can be eliminated, so that only errors caused by measurement inaccuracies remain. Table 6.1 presents the results of this exercise in the form of root mean square residuals in the measured control points. The residuals are found in the control points between the known height and the polynomial error surface. The following conclusions result:

The stereoplotter was not superior to simple parallax bar measurements.

Systematic errors exist in all raw heights and need to be corrected with the use of control points and correction polynomials.

Aircraft radar of Granite Mountain provided higher accuracies than SEASAT satellite radar. This refers to the fact, that the aircraft stereo model has a better stereo configuration, which is expressed by the relationship of stereo base and flying height.

SEASAT satellite radar of Los Angeles is poorer than of Granite Mountain because of a poorer stereo configuration (smaller base).

Digital and optical correlations led to the same performance figures with the images that were employed.

Imagery	Measurement	Nr. of measured points	R.m.s.height error (m)
Seasat, Granite Mtn. Optical	Parallax bar	28	96
	Stereo plotter	28	121
Aircraft, Granite Mtn. Optical	Parallax bar	21	49
	Stereo plotter	21	48
Seasat, L.A. Digital	Parallax bar	28	143
Seasat, L.A. Optical		28	121

Table 6.1 Root mean square errors of radargrammetric heights after polynomial correction

## 6.3 Rigorous Radar Stereo Mapping

### 6.3.1 Mathematical Formulation

For each ground point there are two condition equations for each image:

- (1) The range condition:

$$| \underline{p} - \underline{s} | = r \quad \text{EQ. 6.14}$$

- (2) The squint angle condition:

$$\sin \xi = \underline{s} \cdot (\underline{p} - \underline{s}) / | \underline{s} | \cdot | \underline{p} - \underline{s} | \quad \text{EQ. 6.15}$$

For the formation of a radar stereo model we need to use a pair of these conditions:

$$\begin{aligned} r' &= | \underline{p} - \underline{s}' | = 0 \\ r'' &= | \underline{p} - \underline{s}'' | = 0 \\ \sin \xi' &= \underline{s}' \cdot (\underline{p} - \underline{s}') / | \underline{s}' | \cdot | \underline{p} - \underline{s}' | = 0 \\ \sin \xi'' &= \underline{s}'' \cdot (\underline{p} - \underline{s}'') / | \underline{s}'' | \cdot | \underline{p} - \underline{s}'' | = 0 \end{aligned} \quad \text{EQ. 6.16}$$

The sensor positions  $\underline{s}$  and the sensor velocity vectors  $\underline{\dot{s}}$  are represented as polynomials of the imaging times  $t$ :

$$\begin{aligned} \underline{s} &= (s_x, s_y, s_z) = \underline{s}(t) \\ \underline{\dot{s}} &= (\dot{s}_x, \dot{s}_y, \dot{s}_z) = \underline{\dot{s}}(t) \end{aligned} \quad \text{EQ. 6.17}$$

Imaging times  $t$  can be expressed by radar image coordinate  $x$  and slant range  $r$  by radar image coordinate  $v$  as follows:

$$\begin{aligned} t &= m_x \cdot x + c_x \\ r &= m_y \cdot v + c_y \end{aligned} \quad \text{EQ. 6.18}$$

The x-axis of the radar image system is pointing in flight direction of the imaging sensor.  $m_x$  and  $m_y$  are image scale factors,  $c_x$  is the time corresponding to image coordinate  $x = 0$  and  $c_y$  is the sweep delay.

If we assume error-free sensor orientation and image parameters ( $m_x, m_y, c_x, c_y$ ), the equations 6.16 contain the unknowns  $X, Y, Z$  of the object point and the measurements  $x', y', x'', y''$  for the image coordinates of the left and the right radar image. Linearization leads to:

$$\underline{C} * \underline{v} + \underline{D} * \underline{dp} + \underline{w} = 0$$

EO. 6.19

$\underline{C}$  and  $\underline{D}$  are coefficient matrices of the linearization, the  $\underline{v}$  vector contains the corrections for the image coordinate measurements, the vector  $\underline{dp}$  contains increments for approximately known ground coordinates of the object point and the elements of vector  $\underline{w}$  are the contradictions of Equ. 6.16 when introducing image coordinate measurements and approximate  $X, Y, Z$  values. The unknowns  $\underline{dp}$  can be found by a least squares adjustment with

$$\underline{dp} = -(\underline{D}^T (\underline{C} \underline{G} \underline{C}^T)^{-1} \underline{D}^T (\underline{C} \underline{G} \underline{C}^T)^{-1} \underline{w}$$

EO. 6.20

If orientation and image parameters are not error-free, they may be improved by a radar block adjustment or one can use ground control points to determine calibration polynomials.

In the case of calibration the  $X, Y, Z$  - coordinates of the ground control points are converted to left and right radar image coordinates ( $x_t', y_t', x_t'', y_t''$ ) using the erroneous sensor parameters. The difference between these transformed and the measured image coordinates is approximated with correction polynomials:

$$\begin{aligned} dx' &= dx'(x', y') = a_0 + a_1 * x' + \dots + a_k * y' + \dots \\ dy' &= dy'(x', y') = b_0 + b_1 * x' + \dots + b_k * y' + \dots \\ dx'' &= dx''(x'', y'') = c_0 + c_1 * x' + \dots + c_k * y' + \dots \\ dy'' &= dy''(x'', y'') = d_0 + d_1 * x' + \dots + d_k * y' + \dots \end{aligned}$$

so that

$$\begin{aligned} x_t' &= x' + dx'(x', y') \\ y_t' &= y' + dy'(x', y') \end{aligned}$$

$$\begin{aligned} x_t'' &= x'' + dx''(x'', v'') \\ y_t'' &= y'' + dy''(x'', v''). \end{aligned}$$

EQ. 6.21



### 6.3.2 Results Obtained with Rigorous Stereo Radargrammetry

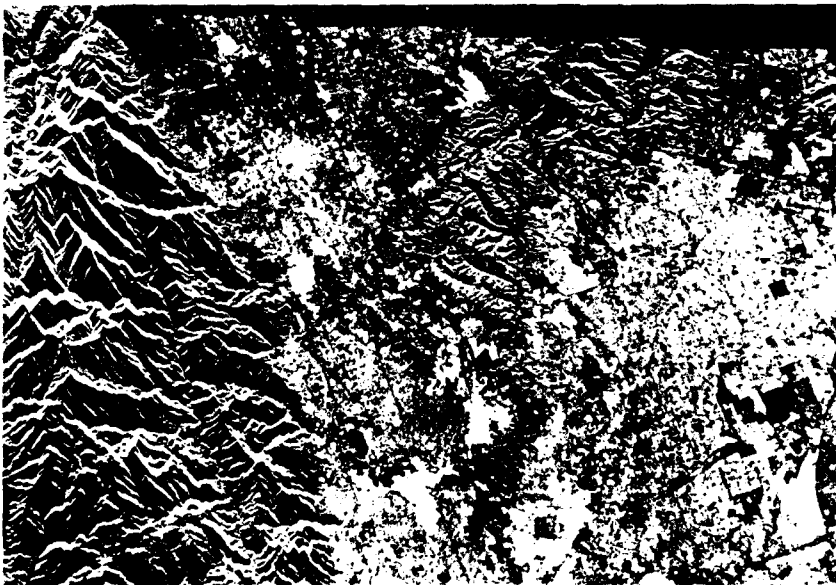
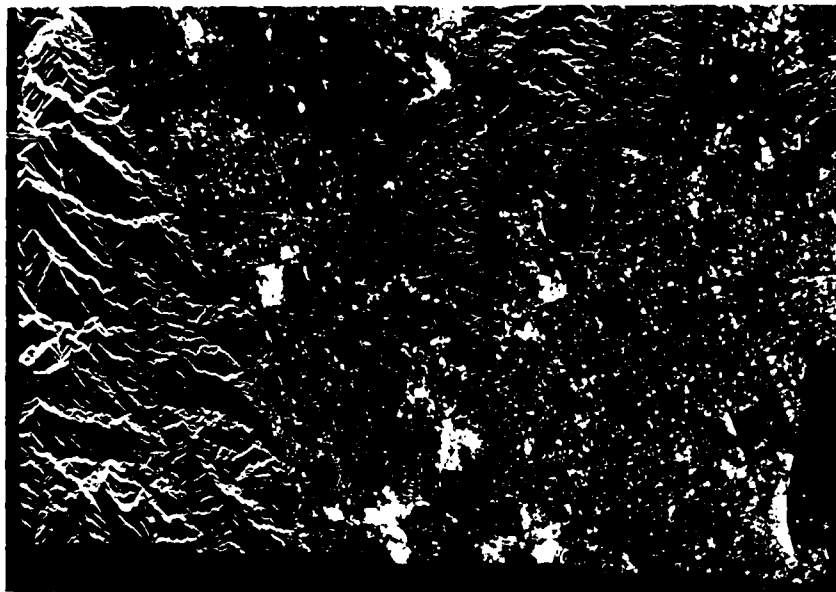
The procedure described above to convert radar image coordinates  $x'$ ,  $y'$ ,  $x''$ ,  $y''$  to object coordinates was applied to a SEASAT radar stereo model of the area of Los Angeles and to a SIR-A radar stereo model of the greek islands Cephalonia and Ithaka. The SEASAT radar stereo model is shown in Figure 6.7 and the SIR-A model previously was presented in Chapter 2, Figure 2.13.

Image coordinates were measured with the analytical plotter KERN DSR-1 used as stereo comparator and transformed to object coordinates  $X_t$ ,  $Y_t$ ,  $Z_t$ . These computed ground point coordinates then were compared with the given values  $X$ ,  $Y$ ,  $Z$ . Table 6.2 summarizes the results that were obtained with the mentioned algorithm. Different kinds of correction polynomials were used to calibrate the erroneous sensor data.

Since the radar image parameters of these models are unknown, at least a calibration polynomial of linear order in  $x$  and  $y$  is necessary to get reasonable results. While the height accuracy of the SEASAT stereo model compares well with that of SIR-A, its accuracy in planimetry is somewhat poorer. This refers to the steeper look angles of the SEASAT imaging system (approximately 22 degrees), where for example an error in slant range causes larger errors for planimetry than for heights (note from chapter 7.1 that the planimetric error is affected by the cosine and the height error by the sine of the elevation angle). Since the look angles for the SIR-A radar system are about 45 degrees, also the errors in planimetry are of the same order of magnitude than those for heights.

Further we see that with the use of flexible calibration polynomials of second order in  $x$  and  $y$  the results may be improved. However, the improvement for SEASAT stereo is about 30 percent while for SIR-A stereo it is only about 20 percent. This is not as much as one might have expected.

Also the use of a poorer but well distributed ground control density leads to quite reasonable results that are not much poorer than those obtained with high ground control density.



15 km

Figure b.7 SEASAT stereo model of Los Angeles, California,  
with same side geometry

AD-A139 565

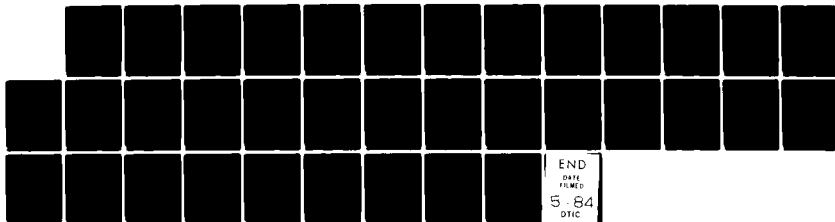
EVALUATION OF RADARGRAMMETRIC STEREO(U) INSTITUT FUER  
DIGITALE BILDVERARBEITUNG UND GRAPHIK GRAZ (AUSTRIA)  
G DOMIK ET AL. 11 OCT 83 F49620-82-C-0053

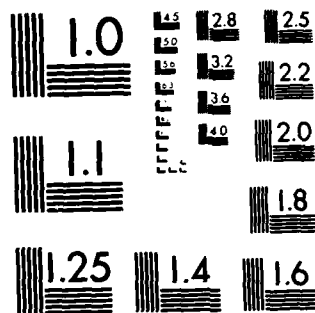
2/2

UNCLASSIFIED

F/G 17/9

NL





MICROCOPY RESOLUTION TEST CHART  
NATIONAL BUREAU OF STANDARDS-1963-A

Radar Imaging System	Ground Control	Calibration		RMS-Residuals (meters)		
		Order in x	Order in y	x	y	z
SEASAT	27 control (check) points	1	1	182	94	94
	- " -	2	1	137	69	70
	- " -	1	2	124	64	65
	- " -	2	2	123	62	62
	7 control points 27 check points	1	1	200	104	107
SIR - A	31 control (check) points	1	1	62	111	94
	- " -	2	1	57	91	82
	- " -	1	2	56	90	102
	- " -	2	2	54	80	76
	6 control points 31 check points	1	1	68	125	123

Table 6.2 Root mean square errors of rigorous radargrammetric mapping method using calibration polynomials

## 7. CONCLUSIONS AND OUTLOOK

The study concerns stereoscopic viewing of side-looking radar images. Current understanding of this effect is based on theoretical considerations of radar parallax, of error propagation and work with actual radar images. This, however, is too limited to be satisfactory: the precise capabilities and limitations of radar stereoscopy remained unclear.

In the framework of the current study one therefore developed a technique for computer simulation of radar images. Using this one can vary a number of significant parameters of the radar imaging process so that a better understanding is obtained of radar stereoscopic effects.

This report presents the starting point for the study by a review of basic principles of radar stereo-imaging, parallax and vertical exaggeration. It then proceeds to describe the chosen technique of radar image simulation. Emphasis is on radar image geometry since stereoscopy is largely a geometric effect. An image space algorithm was chosen as an appropriate method of simulation computations.

The validity of computer generation of images was with simple geometric shapes and with various real radar images of areas where digital terrain elevation models exist. A great number of images was then generated with various look angles, squint angles and flight directions to allow for a complete review of stereo viewing limitations. The conclusions are as follows:

- (a) Same-side stereo from parallel flight lines produces the most distinct vertical exaggeration at steepest look angles, e.g.  $10^\circ$  and  $20^\circ$  off-nadir, with intersection angles of only  $10^\circ$ .
- (b) This same side geometry allows successful stereo-viewing with intersection angles of up to  $60^\circ$ , namely look angles off-nadir of  $20^\circ$  and of  $80^\circ$ , in the extreme case.
- (c) Larger differences of look angles cannot be fused stereoscopically due to excessive shadowing in one image combined with excessive lay-over in the other image.
- (d) Opposite-side stereo from parallel flight lines was not usable for stereo viewing. However, unprocessed raw images with original gray values were used for analysis.

- (e) Crossing flight line stereoscopy is feasible up to intersection angles of about  $42^{\circ}$ .
- (f) The use of squinted radar images does not destroy the stereoscopic effect if squint angles amount to a total of  $30^{\circ}$  or less.

As a by-product of the study also a mathematical model was developed for parallax-computations with crossing flight-line stereo. An understanding was obtained for the occurrence of x and y - parallaxes and for the required orientation of the eye basis. An analysis produced maximum y parallaxes for one existing  $34^{\circ}$  crossing angle SIR-A stereo pair in the amount of 160 m on the ground (50 km swath).

Also a number of rigorous radargrammetric computations were performed on actual radar image pairs from both aircraft and satellite, with accuracies ranging from 49 m (aircraft) to 143 m with Seasat satellite data. SIR-A cross-angle stereo resulted in 78 m to 123 m height errors, depending on the ground control used.

The resources for the study did not allow to cover all aspects of the area of radar stereoscopy, nor of the area of topographic shape reconstruction from radar images.

A next and important step is the addition of both

- (a) ground resolution,
- (b) thematic variation

in the computer simulation. The variability of ground resolution will not affect the "viewability" of radar stereo models, but it will affect the surface definition and therefore the accuracy of measurements. This is a significant element in the evaluation of radar stereo work.

Thematic variability leads to the incorporation of texture, use of several backscatter curves and a chance to more realistically simulate the radar images. It is also meaningful to better understand the relative interdependence of height and planimetric measurement accuracies.

Clearly the work would benefit from studying a wide range of terrain types. This was not possible in the current effort due to limitations in both time and resources.

The improved capability of radar image simulation should be combined with current radar image stereo measurement techniques on photogrammetric analytical plotters. This will then close a complete loop to obtain a

full understanding of the applicability of radar images to topographic stereo mapping.



## Appendix A

### Refined Description of SIMRISA

Fig. A.1 shows a table of contents of the program package. Each rectangle defines a program unit; program functions like input routines or help functions do not appear in the table of contents, but are added after the description of the main routines.

Documentation time during and throughout the development cycle was unfortunately - like always - rather limited. But as good documentation is essential to the continued success of a program development effort, our choice was a HIPO-like (Hierarchy plus Input-Process-Output) documentation design. This has the advantage of not describing the program logic - or at least not until a very low level - but the functions of the system. Thus changing programming logic during the implementation did not result in a redesign of a whole diagram or flow chart.

The next pages show a short documentation of the main routines. Each routine expects some input and creates some output, the corresponding process is described with the help of programming statements, normal English words and structograms. It should be easy enough to read.

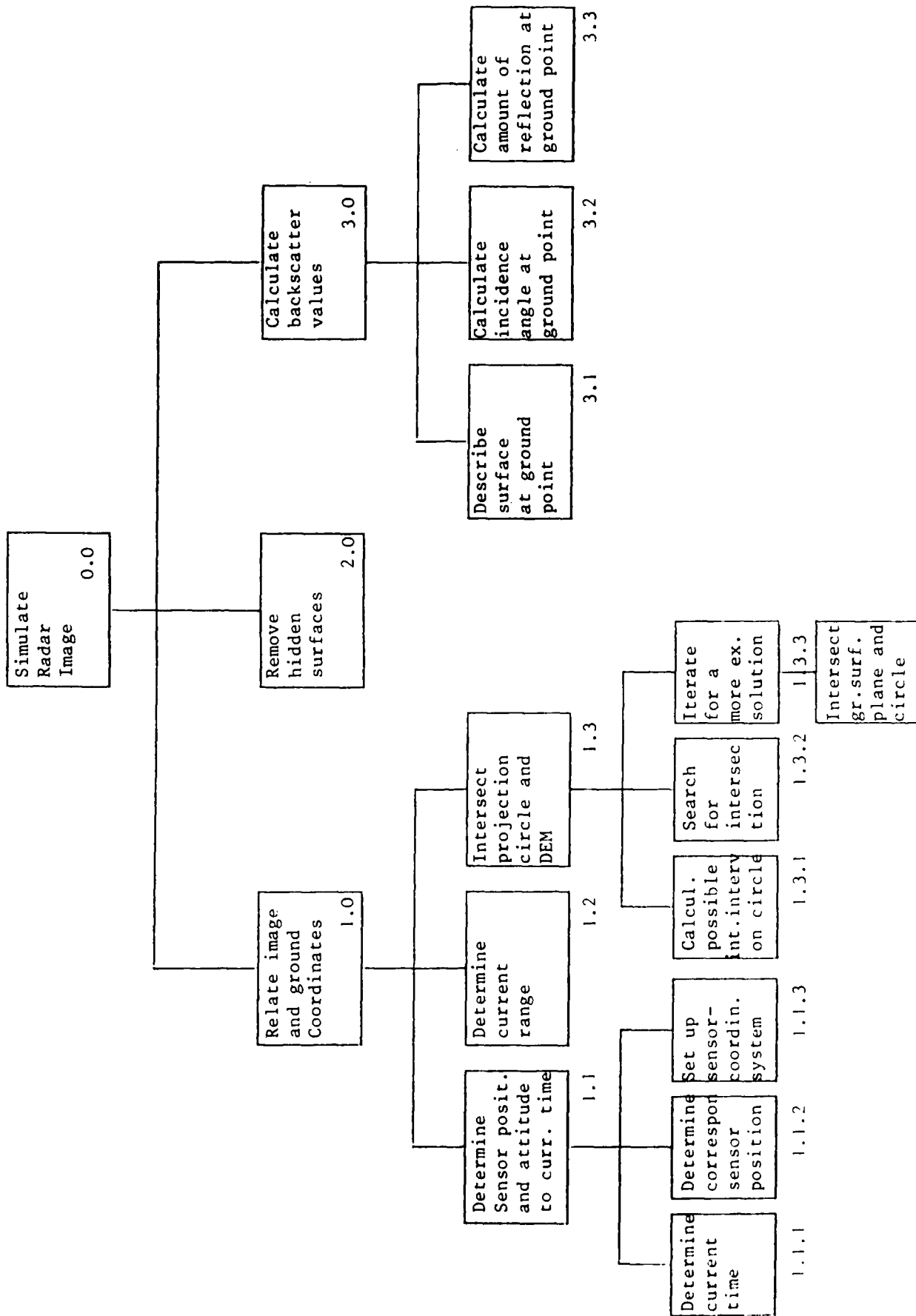
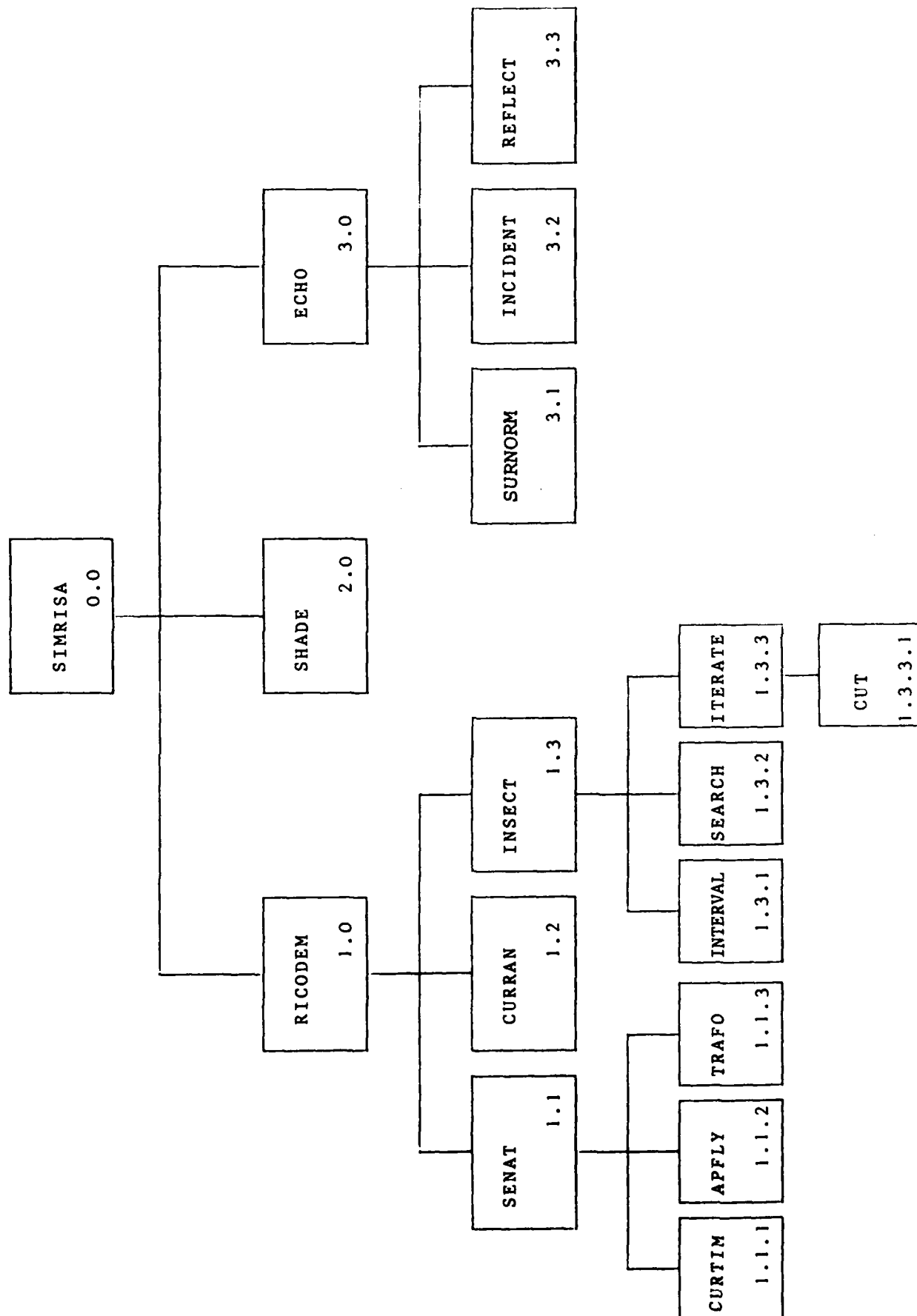


Figure A.1



MENU 0

LEVEL 0

DD-MM-YYYY

- (1) File Names
- (2) DEM Parameters
- (3) Imaging Parameters
- (4) Backscatter Curves
- (5) Test Sets
- (6) Invoke Simulator
- (7) End Session

SELECT NUMBER -

LEVEL 1

MENU 1

DD-MMM-YYYY

FILE NAMES AND DESCRIPTION

(1) Unique Filename

(2) Display Names

(3) Exit to Level 0

SELECT NUMBER 1

DD-NMM-YYYY

MENU 2

LEVEL 1

DEM PARAMETERS

- (1) DEM Size (Row, Col)
- (2) Horizontal Resolutions (Km)
- (3) Vertical Resolution (Km)
- (4) Maximal Height (Km)
- (5) Sweep Delay (Km)
- (6) Display Names
- (7) Exit to Level 0

SELECT NUMBER -

DD-MMM-YYYY

MENU 3

LEVEL 1

IMAGING PARAMETERS

- (1) Image Size (Row,Col)
- (2) Resolutions (sec/km)
- (3) Squint Angle (deg)
- (4) Look Direction (L/R)
- (5) Range Processing (S/G)
- (6) Start time (sec)
- (7) Display Names
- (8) Exit to Level 0

SELECT NUMBER 1

MENU 4

LEVEL 1

DD-NNN-YYY

### BACKSCATTER CURVES

You have the choice of

Hagfors' (H), Muhleman's (M), Cosine (K)

Now active:

Your choice (QUIT to end): -



SYSTEM-ID Radarsimulation

NAME SIMRISA

DIAGRAM-ID 0.0

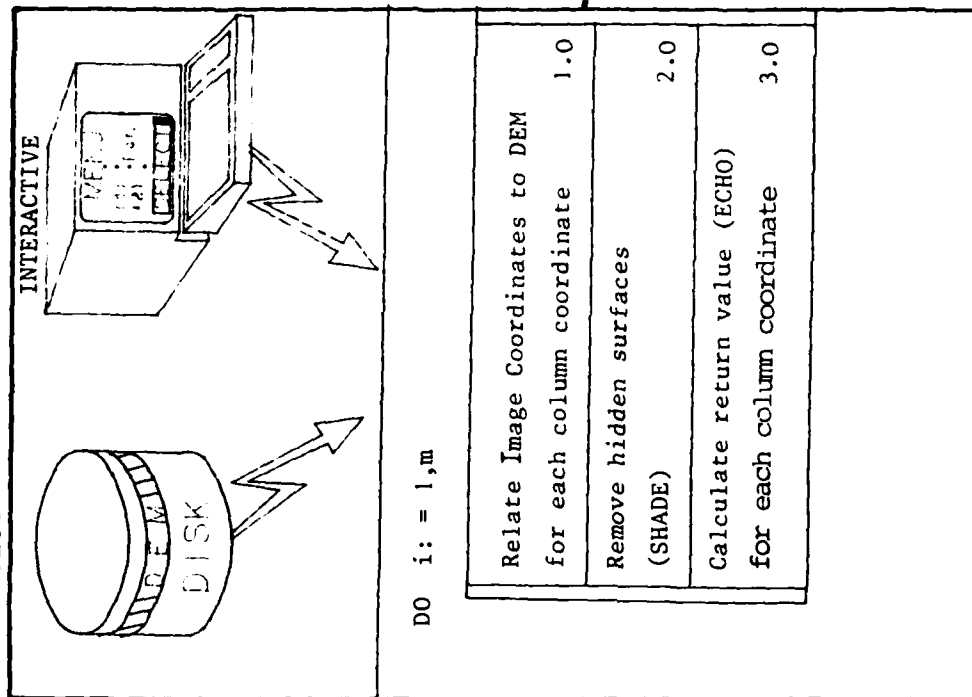
DESCRIPTION SIMulate Radar images using an Image

Space Algorithm

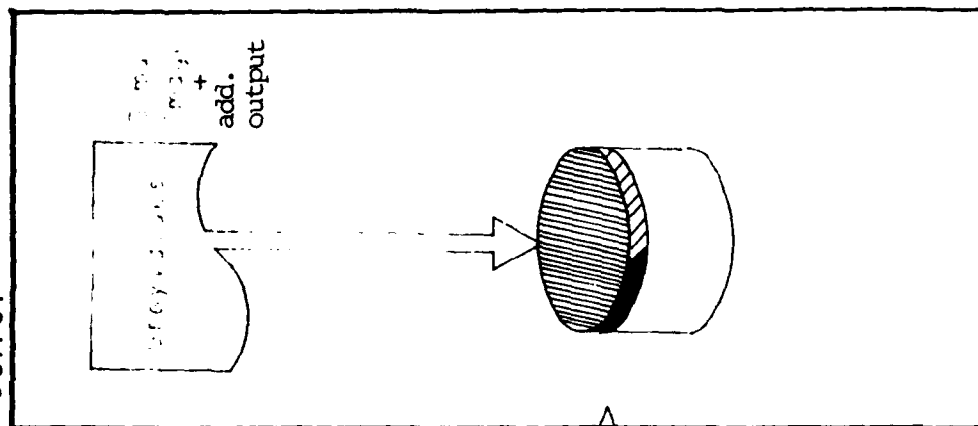
### INPUT

- DEM  
(Digital Elevation  
Model)  
and description  
(Resolutions...)
- Sensor/time  
information
- Imaging parameters  
(image resolutions,  
m..nr of-image lines  
n..nr of-im. col.)
- Backscatter curves

### PROCESS



### OUTPUT



SYSTEM-ID	Radarsimulation	NAME	RICODEM
DIAGRAM-ID	1.0	DESCRIPTION	Relate Image Coordinates and DEM

# INPUT

-i..image row coord
j..image col.coord
n..nr. of im. col.
- image parameters (scale factors)
- DEM

# PROCESS

Define Sensor position S and velocity vector $\dot{s}$ at image row number i	1.1
Do j: = 1,n	
Define slant range r from image column coordinate j	1.2
Intersect circle (sphere (S,r) n cone (S, $\dot{s}$ ;r)) with DEM	1.3

# OUTPUT

-Relation between each (i,j)..image coord. i..fixed j..1,n
$P_k = (P_x, P_y, P_z) \dots$ ...ground coord
K = 1,...,l, l,...layover points corresp. to (i,j)
-additional description to each ground-coord. $\theta_k$ ...elevation angle $d_k$ ...distance between Nadir and $P_k$

SYSTEM-ID Radarsimulation		NAME	SHADE
DIAGRAM-ID	2.0	DESCRIPTION Remove hidden surfaces (Radar SHAD(E)ow)	

### INPUT

- (i,j)...Im.Coord  
 i...fixed  
 j...1,n  
 $P_k, \theta_k$   
 $k = 1, \dots, l_j$   
 $l_n = \sum_{j=1}^n l_j$

### PROCESS

SQRT information of one time  
 line according to ascending  
 distances  
 $(d_1, d_2, \dots, d_{l_n}) \leq d_1 \leq d_2 \leq \dots \leq d_{l_n}$   
 $(\theta_1, \theta_2, \dots, \theta_{l_n}) \Rightarrow \theta_1 ? \theta_2 ? \dots ? \theta_{l_n}$   
 $\theta_{MIN} = \theta_1$   
 DO K = 2, l<sub>n</sub>

$\theta_{MIN} \geq \theta_k$ .TRUE. corresponding $P_k$ is in shadow		.FALSE. $\theta_{MIN} = \theta_k$
--	--	--------------------------------------

### OUTPUT

- (i,j)...image coord.  
 i...fixed  
 j...1,n  
 $P_k, \theta_k$   
 $k = 1, \dots, l_j$   
 $l_n = \sum_{j=1}^n l_j$

SYSTEM-ID	Radarsimulation	NAME	ECHO
DIAGRAM-ID	3.0	DESCRIPTION Calculate return value (ECHO) from imaged points	

### INPUT

```

- (i,j)..image co.
  |
  | i..fixed
  | j...l,n
  |
Pk, θk...
...ground coord.
k = 1...lj
n...nr.of image
col.
- DEM
  
```

### PROCESS

```

Do j = 1,n
  Do K: = 1,lj
    Define slope in Pk 3.1
    Calculate incidence angle in Pk 3.2
    Calculate amount of reflection in this point 3.3
  
```

### OUTPUT

```

  Grey values
  Sim. image
  
```

SYSTEM-ID	Radarsimulation	NAME	SENAT
DIAGRAM-ID	1.1	DESCRIPTION	Determine <u>SENSOR</u> position a. <u>Attitude</u>

# INPUT

-image row coordinate $i$
---------------------------

# PROCESS

Calculate corresponding time to image row
Determine sensor position and velocity vector at time $t$ .
Define sensor coordinate System $(u,v,w)$ with origin in sensor position

# OUTPUT

-Sensor Position $S$ -velocity vector $\underline{\dot{s}}$ -Transformation (shift vector $q$ , Rotation matrix $R$ ) between two Cartesian coordinate systems
--

SYSTEM-ID Radarsimulation

NAME CURRAN

DIAGRAM-ID

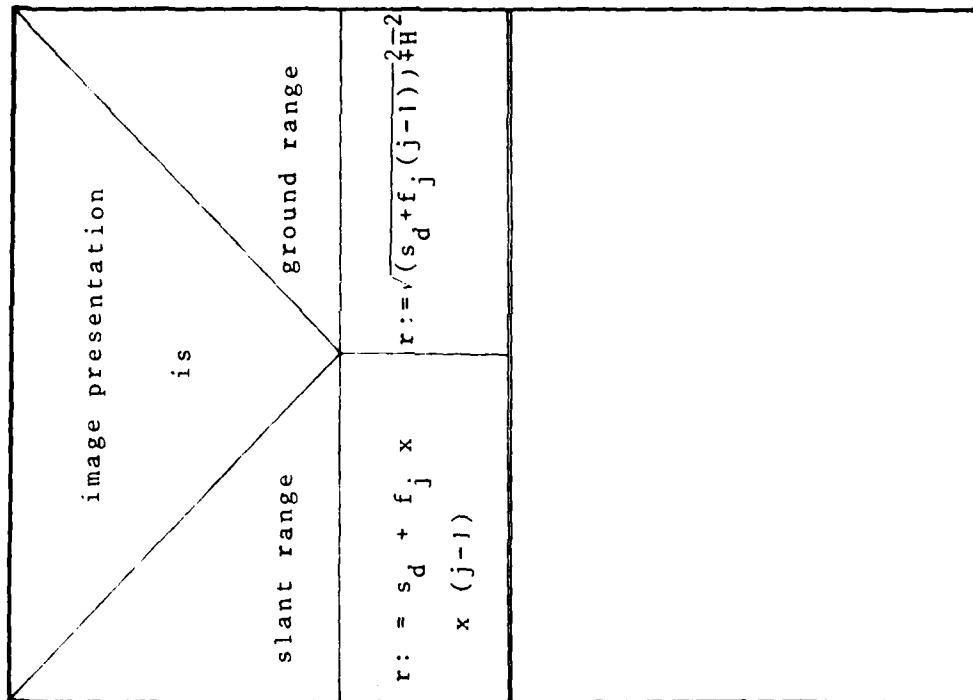
1.2

DESCRIPTION Determine range from image col.coord

INPUT

-image column  
coord. j  
-sweep delay  $s_d$   
-scale factor  $f_j$   
-flight altitude H

PROCESS



OUTPUT

r... slant range

SYSTEM-ID Radarsimulation		NAME INSECT
DIAGRAM-ID 1.3	DESCRIPTION <u>InterSECT circle and DEM</u>	

# INPUT

- DEM  
-  $\theta_0$ ...search  
distance on  
circle

# PROCESS

Define search interval  $[\theta_B, \theta_E]$   
on circle using height informations  
of DEM

$\theta = \theta_B$

WHILE ( $\theta < \theta_E$ ) DO

Compare point on circle defined  
by  $\theta$  and point projected on DEM  
1.3.2

Circle intersects DEM be-  
tween last and recent  $\theta$

.TRUE.

.FALSE.

Start fine  
iteration between  
 $\theta - \theta_0$ ,  $\theta$  and  
intersect analogue  
1.3.3

$\theta := \theta + \theta_0$

# OUTPUT

all intersection points

-  $P_k = (p_{xk}, p_{yk}, p_{zk})$   
and their additional  
description by

-  $\theta_k, d_k$   $k \geq 1$   
to corresponding  
image coord. (i, j)

SYSTEM-ID	Radarsimulation	NAME	CURTIM
DIAGRAM-ID	1.1.1.1	DESCRIPTION	Calculate Current imaging TIME

# INPUT

```

-t_o...Start time
-f_i...scale factor
-i....image row
      coord.

```

# PROCESS

```

t: t_o + f_i x (i - 1)

```

# OUTPUT

```

t...time imaging
i-th row of image

```



SYSTEM-ID Radarsimulation

NAME APFLY

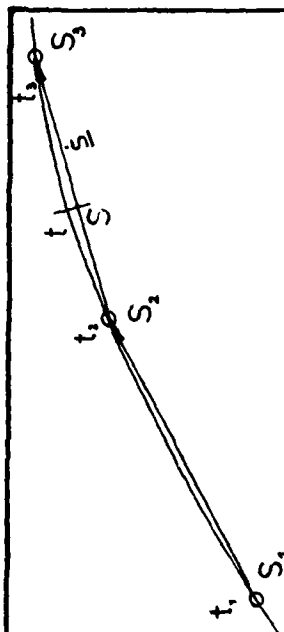
DIAGRAM-ID 1.1.2

DESCRIPTION Approximate FL(Y)ightpath of sensor

#### INPUT

- t...time  
imaging i-th  
image row
- $t_k, S_k, \dots$   
time marks and  
corresponding  
sensor positions

#### PROCESS



Linear approximation of sensor posit.  
and velocity vector between  $(t_{k-1}, t_k]$ ,  
where  $t_{k-1} < t \leq t_k$

#### OUTPUT

- S... Sensor position
- $\dot{S}$ ... velocity vector  
at time t

SYSTEM-ID	Radarsimulation	NAME	TRAFO
DIAGRAM-ID	1.1.3	DESCRIPTION Describe TRANSFORMATION between local and Sensor Coord.System	

# INPUT

<ul style="list-style-type: none"> <li>- <math>S, \underline{s}</math>...Sensor pos. and vector in <math>(x, y, z)</math> Coord. Syst.</li> <li>- <math>\underline{s}_g</math>....Sensor pos. in geocentric Coord. Syst. <math>(X, Y, Z)</math></li> <li>- <math>\underline{\dot{s}}</math>.....velocity vector in <math>(x, y, z)</math></li> </ul>
--

# PROCESS

<p>New coordinate axes:</p> $\underline{u} = \underline{\dot{s}} /  \underline{\dot{s}} $ $\underline{v} = (\underline{s}_g \times \underline{\dot{s}}) /  s_g \times \underline{\dot{s}} $ $\underline{w} = (\underline{u} \times \underline{v}) /  \underline{u} \times \underline{v} $	$\underline{R} = (\underline{u}^T, \underline{v}^T, \underline{w}^T) = \text{Rotation matrix}$ $\underline{q} = \underline{s} \dots \text{Shift vector}$
---	--

# OUTPUT

<ul style="list-style-type: none"> <li>- Shift vector <math>\underline{q}</math> and</li> <li>- Rotation matrix <math>\underline{R}</math> to convert from local to sensor coordinate system</li> </ul>
---

SYSTEM-ID Radarsimulation		NAME	INTERVAL
DIAGRAM-ID	1.3.1	DESCRIPTION	Define INTERVAL on circle to be searched

### INPUT

-HMAX-	
maxim. height of	
DEM	
-HMIN-	
minim. height of	
DEM	
-proj. circle	

### PROCESS

intersect projection circle with plane parallel to (x,y) plane at height HMIN (z = HMIN...in (x,y,z) Coord. Syst) == > $\theta_B$	
intersect projection circle with plane parallel to (x,y) plane at height HMAX (z = HMAX...in (x,y,z) Coord. Syst) == > $\theta_E$	

### OUTPUT

Search interval on circle $[\theta_B, \theta_E]$
---

SYSTEM-ID	Radarsimulation	NAME	SEARCH
DIAGRAM-ID	1.3.2	DESCRIPTION	SEARCH for intersection

INPUT

- $\tau$ - DEM - r..slant range - R,q... Transform. between local and sensor coord.syst -last-diff: last height difference - $\theta$	Rem: $P = (P_u, P_v, P_w)$ ground point in sensor coord. syst. $P = (P_x, P_y, P_z)$ ground point in local coord. $h(P_x, P_y)$ = height in $(P_x, P_y)$ acc.to DEM
---	---

PROCESS

$P_u = r \times \sin \tau$ $P_v = r \times \sqrt{\sin^2 \theta - \sin^2 \tau}$ $P_w = -r \times \cos \theta$	$(P_x, P_y, P_z)^T = R^T \times (P_u, P_v, P_w)^T + q$
Convert from sensor to local coord. syst.: $(P_x, P_y, P_z)^T = R^T \times (P_u, P_v, P_w)^T + q$	$\text{Diff} = h(P_x, P_y) - P_z$
$\text{diff} \times \text{last-diff} > 0$ .TRUE.	.FALSE.
Circle does not intersect DEM	Circle intersects DEM between last and recent $\theta$

OUTPUT

- intersection did (not) happen between last and recent DEM
---

SYSTEM-ID Radarsimulation

NAME ITERATE

DIAGRAM-ID 1.3.3

DESCRIPTION ITERATE for a more exact solution

# INPUT

- $[\theta_B, \theta_E]$  ...  
Search interval  
on circle
- $\theta_0$  ... search dis-  
tance on circle
- $d_f$  ... division  
factor
- DEM

# PROCESS

$$\theta_o := \theta_o / d_f$$

$$\theta = \theta_B$$

WHILE ( $\theta < \theta_E$ ) DO

Compare point on circle defined  
by  $\theta$  and point projected on DEM

Circle intersect DEM be-  
tween last and recent  $\theta$

.TRUE.

.FALSE.

intersect  
circle and DEM  
1.3.3.1

$$\theta := \theta + \theta_o$$

# OUTPUT

- $\theta$ , where the circle  
point defined by  
 $\theta$  is in the close  
environment of the  
intersection

SYSTEM-ID	Radarsimulation	NAME	CUT
DIAGRAM-ID	1.3.3.1	DESCRIPTION	CUT surface plane and circle

# INPUT

<ul style="list-style-type: none"> <li>- <math>\theta</math>...defines point on circle in environment of intersection</li> <li>- <math>P, q</math>...inclination i in x or y direction of plane in same environment</li> </ul>
--

# PROCESS

<p>intersect plane with normal vector</p> $\underline{n} = \begin{bmatrix} -\tan p \\ -\tan q \\ 1 \end{bmatrix} \dots \text{defined in } x, y, z$ <p>and circle</p> $v^2 + w^2 = r^2 \times \cos^2 \tau \dots \text{defined in } u, v, w$	
--	--

# OUTPUT

<ul style="list-style-type: none"> <li>- (intersection point <math>\underline{p} = (P_x, P_y, P_z)</math>)</li> <li>- corresponding elevation angle <math>\theta</math> and distance to nadir d</li> </ul>
--

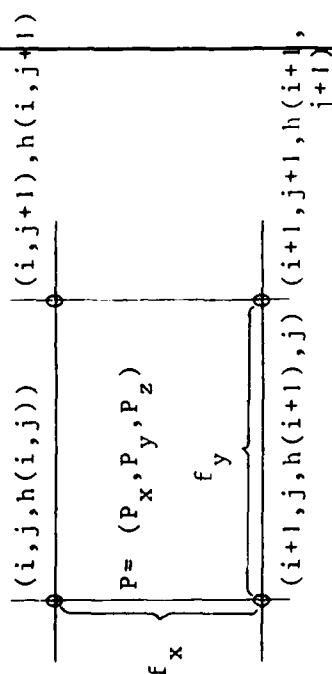
SYSTEM-ID	Radarsimulation	NAME	SURNORM
DIAGRAM-ID	3.1	DESCRIPTION	Describe Surface around P

# INPUT

- $P = (P_x, P_y, P_z) \dots$   
..ground point
- DEM
- $f_x, f_y$   
ground resolution  
in x resp. y  
direction

# PROCESS

Rem.: Ground resolution cell:



$P_x \in [i, i+1)$

$P_y \in [j, j+1)$

$$\tan p = \frac{\frac{h(i+1, j) + j(i+1, j+1)}{2} - \frac{h(i, j) + h(i, j+1)}{2}}{f_x}$$

$$\tan q = \frac{\frac{h(i, j+1) + h(i+1, j+1)}{2} - \frac{h(i, j) + h(i+1, j)}{2}}{f_y}$$

# OUTPUT

- p, q...inclinations in  
x resp. y direction

SYSTEM-ID	Radarsimulation	NAME	INCIDENT
DIAGRAM-ID	3.2	DESCRIPTION	Define INCIDENT angle

# INPUT

-S= (S<sub>x</sub>, S<sub>y</sub>, S<sub>z</sub>)...  
 Sensor position  
 -p= (P<sub>x</sub>, P<sub>y</sub>, P<sub>z</sub>)...  
 Ground point  
 -p,q...inclination  
 in x resp. y di-  
 rection  
 -f<sub>x</sub>, f<sub>y</sub>...  
 ground resolution  
 in x resp. y di-  
 rection  
 -r...slant range  
 -θ...elevation angle

# PROCESS

$$\cos \theta^i = (\cos \theta \cos \psi + \sin \theta \sin \psi) \times \cos \gamma$$

where

θ...elevation angle

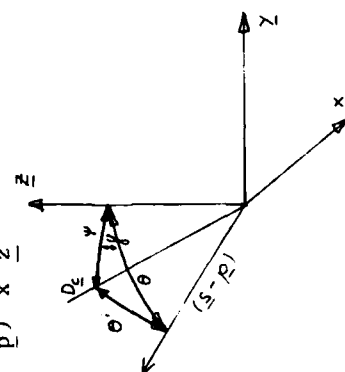
ψ...Angle between surface normal

to flat surface (z)

and surface normal at P(c)

γ...angle between c x z and

$$(\underline{s} - \underline{p}) \times \underline{z}$$

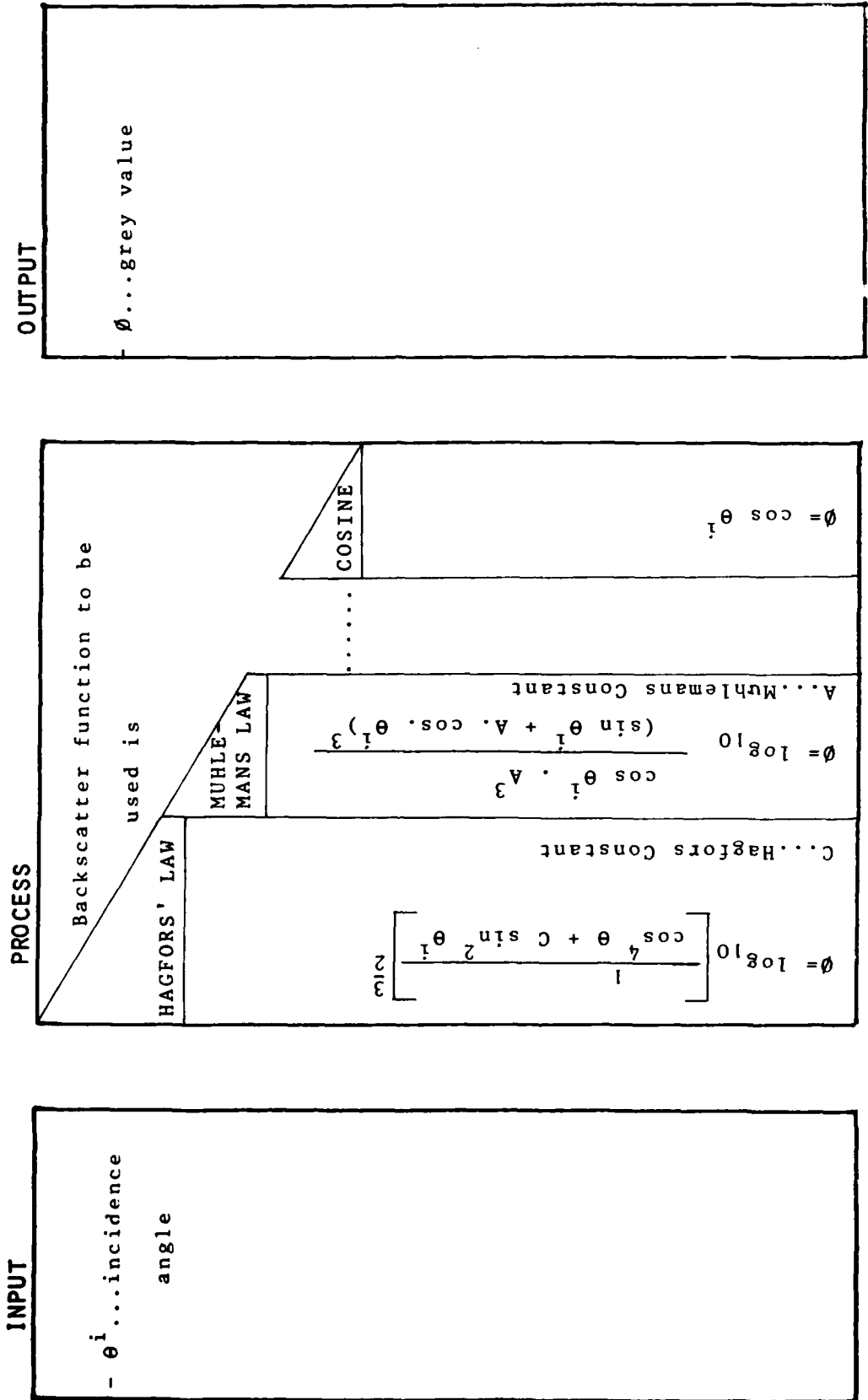


# OUTPUT

-θ<sup>i</sup>...incidence angle  
 at P=(P<sub>x</sub>, P<sub>y</sub>, P<sub>z</sub>)



SYSTEM-ID	Radarsimulation	NAME	REFLECT
DIAGRAM-ID	3.3	DESCRIPTION Calculate amount of REFLECTION	



## Appendix B

### List of Figures and Tables

#### FIGURES

Figure 1.1:	Radar imaging from orbit.....	5
Figure 2.1:	Flight configurations for overlapping images.....	7
Figure 2.2:	Aircraft radar pair, opposite side stereo.....	9
Figure 2.3:	Same as Figure 2.2, but same-side geometry.....	10
Figure 2.4:	Same-side geometry SAR stereo (3 cm wl.).....	11
Figure 2.5:	Same-side geometry SEASAT SAR stereo (25 cm wl.)....	12
Figure 2.6:	SEASAT-SAR stereo Los Angeles area.....	13
Figure 2.7:	Same as Fig. 2.6, but opposite-side geometry.....	14
Figure 2.8:	Apollo 17 Lunar Sounder Experiment (ALSE).....	15
Figure 2.9:	Definitions for radar stereo computations.....	16
Figure 2.10:	Definitions for the vertical exaggeration factor....	20
Figure 2.11:	Orbit configurations for SIR-A.....	23
Figure 2.12:	Imaging geometry for SIR-A convergent stereo.....	26
Figure 2.13:	Stereoscopic radar image pair (Greek Islands).....	27
Figure 2.14:	Explanation of radar stereo parallax.....	28/2
Figure 2.15:	Amount of x and y-parallaxes.....	30
Figure 2.16:	Values for parallaxes in SIR-A stereo model.....	31
Figure 3.1:	Set-up for an object space algorithm.....	35
Figure 3.2:	Imaging in a plane.....	36
Figure 3.3:	Imaging with squint angle.....	38
Figure 3.4:	Ground point P in 2 coordinate systems.....	40
Figure 3.5:	Doppler cone and range sphere. Perspective view....	43
Figure 3.6:	Doppler cone and range sphere. Vertical view.....	43
Figure 3.7:	Rectifying "squint image" geometrically.....	45
Figure 3.8:	Simulated radar images (squinted).....	47
Figure 3.9:	Reference Image to Fig. 3.8.....	47
Figure 4.1:	Synthetic Height Model.....	52
Figure 4.2:	Imaging geometry for slant range presentation.....	53
Figure 4.3:	Radar illuminated height model.....	54
Figure 4.4:	Radar slant range presentation.....	54
Figure 4.5:	Opposite side stereo pair.....	55
Figure 4.6:	Sensor configuration for 4.5.....	54
Figure 4.7:	Map of Cephalonia (a) and Ithaka (b).....	57
Figure 4.8:	Simulations of Greek islands.....	58
Figure 4.9:	Real and simulated image from N-California.....	60
Figure 4.10:	Sketch map of a SAR-580 test site.....	61
Figure 4.11:	Digital elevation model of Oetzal.....	62
Figure 4.12:	Surface relief at the profiles in Fig. 4.10.....	63
Figure 4.13:	Radar image of Oetzal (ground range).....	64
Figure 5.1:	Configurations of same side stereo.....	67
Figure 5.2:	Examples of simulated radar images (same side).....	68
Figure 5.3:	Examples of simulated radar images (squinted).....	72
Figure 5.4:	Configuration of "cross angle" stereo.....	73
Figure 5.5:	Examples of simulated radar images (cross-track)....	75/7

Figure 6.1:	Coordinate system.....	77
Figure 6.2:	Errors due to $ds_y$ '-component of sensor position.....	78
Figure 6.3:	Errors due to $ds_z$ '-component of sensor position.....	81
Figure 6.4:	Error due to $ds_y$ - component of velocity vector.....	82
Figure 6.5:	Error due to range error.....	83
Figure 6.6:	Stereo model with digital correlation.....	85
Figure 6.7:	SEASAT stereo model with same side geometry.....	92

## TABLES

Table 2.1:	Exaggeration factors for radar stereo imagery.....	25
Table 5.1:	Same side stereo evaluation.....	69
Table 5.2:	Ranking of best same side stereo images.....	70
Table 5.3:	Evaluation of squint angle images.....	73
Table 5.4:	"Cross-Angle" Stereo Evaluation.....	76
Table 6.1:	Root mean square errors of radargrammetric heights after polynomial correction.....	87
Table 6.2:	Root mean square errors of rigorous radargrammetric mapping method using calibration polynomials.....	93

## LITERATURE

- Bair, G.L. and Carlson, G.E., 1975:  
"Height Measurement with Stereo Radar"  
Photogramm. Eng. and Remote Sensing,  
Vol XLI.
- Bair, G.L. and Carlson, G.E., 1974:  
"Performance Comparison of Techniques for Obtaining  
Stereo Radar Images", IEEE Trans. on Geoscience  
Electronics, GE-11.
- Carlson, G.E., 1973:  
"An Improved Single Flight Technique for Radar Stereo",  
IEEE Trans. on Geoscience  
Electronics, GE-11, No. 4, 1973.
- Cimino C., Elachi C., 1982:  
"SIR-A Radar Parameters. On/Off Times. Latitude  
and Longitude". Internal JPL-Report  
Pasadena, Cal. 91109, USA.
- DBA-Systems, 1974:  
"Research Studies and Investigations for Radar Control  
Extensions", DBA Systems, Inc., P.O. Drawer 550, Melbourne,  
Florida, Defense Documentation  
Center Report No. 530784L.
- Derenyi, E.E., 1975:  
"Topographical Accuracy of Side Looking Radar Imagery",  
Bildmessung und Luftbildmessung, No. 1, 1975
- Elachi C., Granger J., 1982:  
"Spaceborne Imaging Radars Probe in Depth".  
IEEE Spectrum.
- Elachi C., 1983:  
"Radarbilder der Erde". Spektrum der Wissenschaft,  
Feb. 1983; Translated from: Scientific American,  
Dec. 1982.
- Goodyear, 1974:  
"Preliminary Imagery Data Analysis",  
Goodyear Electronic Mapping System (GEMS),  
Goodyear Aerospace Corp., Report GIG-9342, Code  
99696.
- Gracie, G. et al., 1970:  
"Stereo Radar Analysis", US Engineer

Topographic Laboratory, Ft. Belvoir,  
Virginia Report No. FTR-1339-1.

- Graham, L., 1975:  
"Flight Planning for Radar Stereo Mapping",  
Proc. Am. Soc. Photoqramm., 41 st. meeting,  
Washington, D.C.
- Greve, C.W., W.A. Cooney, 1974:  
"The Digital Rectification of Side Looking Radar  
Imagery", Proceedings of the American Society of  
Photogrammetry, Fall Meeting '74, pp. 19-32
- Hagfors T., 1969:  
"Backscattering from an Undulating Surface with  
Applications to Radar Returns from the Moon",  
J. Geophys. Res. 1969, pp.3779-3784
- Hoare C.A.R., 1962:  
"Quicksort". Computer J. 5 1962, pp.10-15
- Holtzman, J.C., V.S. Frost, J.L. Abbott, V.H. Kaupp, 1978.  
"Radar Image Simulation". IEEE Trans. on Geoscience  
Electronics, Vol. GE-16
- Innes, R.B., 1964:  
"Principles of SLAR-Measurements of the Third  
Coordinate of Target Position", Report of Project  
Michigan No. 2900-474-T, 1964.
- Kaupp V. L. Bridges, M. Pisarnek, H. MacDonald,  
W. Waite, 1982:  
"Comparison of simulated Stereo Radar Imagery."  
IGARSS '82, Munich, Paper TA4, June 1-4, 1982.
- Kobrick M., F. Leberl, J. Raggam (1983, in print):  
"Convergent Stereo with Shuttle Imaging Radar".
- Konecny, G., 1972:  
"Geometrische Probleme der Fernerkundung, Bildmessung  
und Luftbildwesen, Vol.42, No.2.
- LaPrade, G.L., 1963:  
"An Analytical and Experimental Study of Stereo  
for Radar", Photoqramm., Eng. Vol. XXIX.
- LaPrade, G.L., 1970:  
"Subjective Considerations for Stereo Radar",  
Goodyear Aerospace Corp., Report GIB-9169,  
and Photoqramm. Eng.
- LaPrade, G.L., 1975:  
"Addendum to GIB-9169, Subjective Considerations

for Stereo Radar", Goodyear Aerospace Corp.,  
Arizona Division.

LaPrade, G.L. et al., 1980:

"Stereoscopy", Manual of Photogrammetry,  
4th Edition, American Society of Photogrammetry,  
Falls Church, USA.

Leberl F., 1972:

"On Model Formation with Remote Sensing Imagery".  
Oesterreichische Zeitschrift f}r Vermessungswesen.  
1972, Nov.2.

Leberl, F., 1975:

"Lunar Radargrammetry with ALSE-VHF-Imagery",  
Proc. Am. Soc. Photogramm., Fall Tech. Meeting,  
Phoenix Arizona.

Leberl, F., 1978:

"Satellitenradargrammetrie", Deutsche Geodaetische  
Kommission, Series C, No. 239, Munich, 156 p. 1978.

Leberl, F., 1979:

"Accuracy Aspects of Stereo-Side-Looking Radar",  
JPL-Publication 1979-17, Jet Propulsion Laboratory,  
Pasadena, USA.

Leberl, F. and Raggam, H., 1982:

"Satellite Radargrammetry", Phase I.  
Final Report. DIBAG-Report Nr. 4,  
Research Center Graz, Austria

Leberl F., J. Raggam, M. Kobrick (1983, in print):

"Stereo Viewing of Radar Images".  
IEEE Trans. Geoscience Remote Sensing.

Maurer H., 1974:

"Datenstrukturen und Programmierverfahren".  
Teubner-Studienbuecher, Stuttgart 1974

Muenster C., 1942:

"Ueber einige Probleme der stereoskopischen Messung".  
Zeitschrift f}r Instrumentenkunde pp 346 - 357, 1942.

Rinner K., R. Burkhardt, 1972:

"Photogrammetrie", Band III a/1, Handbuch der Vermessungskunde  
J.B. Metzler'sche Verlagsbuchhandlung,  
Stuttgart.

Rosenfield, G.H., 1968:

"Stereo Radar Techniques", Photogramm. Eng.  
Vol. XXXIV., 1968.

Rott H., 1983:

"SAR Data Analysis for an Alpine Test Site".  
Paper presented at the SAR-580 Workshop in  
Ispra, Italy, April 1983.

Sutherland I.E., Sproull R.F., Shumacker R.A., 1974:

"A Characterization of Ten Hidden-Surface Algorithms".  
Computing Surveys, Vol. 6, No.1, March 1974.

Unruh J.E., Mikhail E.M., 1981:

"Surveying, Mapping, Geodesy, and Photogrammetry;  
Digital Image Simulation for Photogrammetric  
Applications", Purdue University.

Williams J.W.J., 1964:

"Heapsort". C. ACM 7, Nr. 6 1964, pp. 349-358

ND

TE

ED

84

C